



McGill

Design and Validation of a Laser Thermal Propulsion Thruster Powered by a Fiber Laser

Gabriel Roland Dubé

Department of Mechanical Engineering
McGill University, Montreal

July 2025

A thesis submitted to McGill University
in partial fulfillment of the requirements of the degree of
Master of Science

Contents

List of Figures	vi
List of Tables	vii
Nomenclature	viii
Abstract	ix
Résumé	x
Acknowledgements	xii
1 Introduction	1
1.1 Motivation	1
1.2 Literature review	3
1.3 Summary and direction of work in this thesis	10
2 Facility design	13
2.1 Version 1 test section design	13
2.2 Version 2 test section design	13
2.2.1 Requirements for the version 2 test section	14
2.2.2 Initial sizing of the double choked laser-thermal propulsion thruster .	17
2.2.3 Test section and thrust stand	19
2.2.4 Laser and optics	19
2.2.5 Timing control	20
2.2.6 Data acquisition system and oscilloscope	21
2.2.7 Cameras	22
2.2.8 Spark initiation system	23
2.2.9 Needle valve	24

3 Experiments	27
3.1 Static laser-sustained plasma validation	27
3.1.1 Spark initiation of plasma in version 1	27
3.1.2 Seeding argon with NO ₂	29
3.1.3 Spark initiation of plasma in version 2 and quasi-continuous wave laser-sustained plasma	30
3.1.4 Optical experiments: going from quasi-continuous wave to continuous wave laser-sustained plasma	31
3.1.5 Version 2 continuous wave laser-sustained plasma	35
3.2 Version 2 cold flow thruster characterization	38
3.2.1 Cold flow thrust tests	38
3.2.2 Thruster nozzle effective sonic area A^*	40
3.2.3 Needle valve effective sonic area A^*	41
3.2.4 Summary of results	43
3.3 Initial quasi-continuous wave laser-sustained plasma thrust tests (hot fire) .	44
4 Zero-dimensional laser-sustained plasma model	46
4.1 Equilibrium calculations	46
4.2 Bremsstrahlung energy loss	49
4.3 Model setup	50
4.4 Model results	52
5 Discussion	56
5.1 Experiment	56
5.2 Model discussion	63
6 Conclusion	65
6.1 Summary	65
6.2 Future work	66
References	68
A YLR-300/3000-QCW-MM-AC Calibration Report	71
B P30 Collimator Calibration Report	78
C Omega PX119A-1KG5V Calibration	80
D V2 Test Section Parts Drawings	82

CONTENTS

CONTENTS

E V2 Second (Rear) Window Mount	91
F Untested V2 Parts Drawings	93

List of Figures

1.1	LTP architecture (Duplay [4])	2
1.2	Overview of LTP system (Duplay [4])	2
1.3	Cross-section drawing of 10 kW thruster from Shoji [6] (original is of poor quality)	3
1.4	Experimental apparatus from Keefer <i>et al.</i> [8]	4
1.5	Experimental apparatus from Zerkle <i>et al.</i> [10]	5
1.6	Apparatus used in Black <i>et al.</i> [12]	6
1.7	Two thruster models from Toyoda <i>et al.</i> [13]	7
1.8	Experimental setup from Lu <i>et al.</i> [14]	8
1.9	LSP setups from Takano <i>et al.</i> [16]	9
2.1	V1 LTP thruster from Duplay [4]	14
2.2	Renders of the V2 LTP thruster	15
2.3	Cutaway of the V2 double choked LTP thruster showing both choking orifices: the metering valve and the nozzle. Ports other than the argon inlet are omitted for clarity.	18
2.4	V2 LTP thruster	20
2.5	V2 LTP thruster	21
2.6	Laser system	21
2.7	Electronics rack with laser at the base	22
2.8	Delay generators and oscilloscope	23
2.9	Data acquisition (DAQ) system	23
2.10	Spark initiation system. On the left is a power supply, while spark coil number 6 is on the right.	24
2.11	Assembled electrodes with Ultra-Torr cap and electrical connectors	24
2.12	WL14H-320P Needle valve	25

2.13 Size comparison between V1 (top, on extrusion rails) and V2 (bottom, mounted in front of laser collimator). V2 is in static configuration, without the extension cylinder.	25
3.1 V1 spark alignment	28
3.2 Signal timing diagram. The <i>trig</i> prefix denotes triggering signals. The component is active when the line is high. Timings in ms are also indicated on the figure.	28
3.3 QCW LSP spark initiation in V1: 3079 W, 20 bar. LSP142_SPRK15.	29
3.4 Average dynamic pressure rise of QCW LSP shots in a mixture of NO ₂ and argon compared to that of pure argon QCW LSP. Initial pressure was 20.15 bar. Values given in the legend are the partial pressure of NO ₂ seeding in the gas.	30
3.5 2 FOVs of alignment laser light on power meter. The aberration at the center of the red light is due to laser damage to the window.	31
3.6 100% power (3079 W) QCW LSP shot	31
3.7 LSP threshold graph for V1 with 125 mm focal length lens	33
3.8 Model of the lenses showing paraxial rays and focus	34
3.9 Spot diagrams of the three lens systems studied	35
3.10 LSP threshold graph for V1 with dual-lens system	36
3.11 LSP threshold graph for V2 with dual-lens system	36
3.12 First CW LSP captured by the webcam: 342 W, 20.00 bar. LSP385_V2_CW1.	37
3.13 First CW LSP captured by the Photron high-speed camera: 342 W, 20.00 bar. LSP385_V2_CW1.	37
3.14 Dynamic pressure rise from CW LSP measured with PCB transducer	38
3.15 Typical cold flow pressure and thrust curves for 20 bar chamber pressure	39
3.16 Absolute pressure versus thrust and curve fit of pressure-thrust relation	39
3.17 Multiple cold flow thrust tests in succession	40
3.18 Saad blowdown model and experimental data	42
3.19 Bubble flow meter setup	43
3.20 Two QCW thrust tests	44
3.21 Nozzle ablation during flowing test. LSP315_V2_Flow4.	45
3.22 V2 Flowing QCW LSP. LSP321_V2_Flow10.	45
4.1 Gibbs free energy (<i>G</i>) plotted against the degree of dissociation (<i>x</i>) of hydrogen under three different pressures	48
4.2 Comparing calculated <i>c_p</i> values of argon to those from CEA	48
4.3 Model of an LSP inside a volume of pressurized argon	50

4.4	Experimental data compared to the 0D model, with both Bremsstrahlung and blackbody losses	53
4.5	Pressure change over time during two further LSPs, with Bremsstrahlung loss	54
4.6	Pressure increase from 0D model as a function of laser power, with initial pressure of 20 bar	54
5.1	V1 single plug electrodes	57
5.2	V1 with newly machined opposing bottom ports	57
5.3	Electrode manufacturing process	59
5.4	Ablation damage to the flat rear plate of the thruster after two 3 kW laser shots	59
5.5	Rear window damage on V2	60
5.6	Window extension tube	61
5.7	Nozzle laser damage	62
5.8	New nozzle parts	62
5.9	Mechanism of LSP growth	63

List of Tables

1.1	Summary of a selection of past LSP experiments. λ : wavelength, P : maximum laser power, p : pressure, I_{sp} : maximum specific impulse, F_T : maximum thrust	11
1.2	Comparative table of experimental LTP thruster efficiencies	12
3.1	Statistics from the power meter after 10 times 50 ms laser shots at 10 % and 12 % power	32
3.2	Simulated focal length and spot diameter of various lens assemblies in Win-Lens3D. The average laser flux is calculated for 342 W of incident power . .	34
3.3	Calculated opening area and calculated diameter for needle valve at different rotation increments (upstream pressure = 5000 kPa and outlet pressure = 100 kPa)	42
3.4	Summary of the studied V2 thruster characteristics	43
4.1	Comparison of Bremsstrahlung power density loss	49
4.2	Initial values for 0D model	55

Nomenclature

Abbreviations

- 0D Zero-dimensional
- BPP Beam Parameter Product
- CW Continuous Wave
- DAQ Data Acquisition
- FOV Field Of View
- IR Infrared
- LSP Laser-Sustained Plasma
- LTP Laser-Thermal Propulsion
- MAOP Maximum Allowable Operating Pressure
- NPT National Pipe Thread
- QCW Quasi-Continuous Wave
- STP Standard Temperature and Pressure
- UV Ultraviolet
- V1 Version 1
- V2 Version 2

ABSTRACT

For ambitious space missions like rapid human transit to Mars, conventional propulsion methods fall short. Laser-Thermal Propulsion (LTP) utilizes lasers to heat propellant gas, generating thrust with potentially greater specific impulse than traditional rocket engines. Two lab-scale LTP thrusters were tested in this thesis, denoted Version 1 (V1) and Version 2 (V2). Version 1 permitted initial testing and visualization of the Laser-Sustained Plasma (LSP) wave propagation. As a prototype for an actual thruster, Version 2 was optimized for thrust measurements. The design process of the improved V2 thruster is also presented. These thrusters were powered by a 300 W Continuous Wave (CW), 3 kW Quasi-Continuous Wave (QCW) 1.07 μm fiber laser. Argon was used as the propellant at a pressure of 20 bar, selected for its ease of ionization. Using an automotive-type coil, spark initiation of QCW LSP was successfully implemented in V1 and V2. Seeding of the argon with nitrogen dioxide (NO_2) at partial pressures between 0.12 bar to 0.55 bar showed the gas absorbed more than double the laser energy compared to pure argon propellant. To increase laser flux to the plasma, an optical system of two lenses was designed. Different lenses were compared using ray tracing software (WinLens3D). A CW LSP was achieved in V2, lasting 85.1 ms. This represents a 1.7 times longer lifetime than the maximum QCW pulse length of 50.0 ms at this power. Average cold flow thrust of V2 was approximately 1 N. In order to interpret the experimental results, a zero-dimensional (0D) heat transfer model was written in Python, using Bremsstrahlung as the mechanism of radiation. Finally, paths to further improve the V2 thruster and thrust stand are presented to eventually enable accurate thrust measurements with CW operation.

RÉSUMÉ

Pour des missions spatiales ambitieuses comme le transit rapide d'humains vers Mars, les méthodes de propulsion conventionnelles ne sont pas à la hauteur. La propulsion laser-thermique (LTP) utilise des lasers pour chauffer le gaz propulseur, générant ainsi de la poussée avec une impulsion spécifique potentiellement plus grande que les moteurs fusées traditionnels. Deux propulseurs LTP à l'échelle du laboratoire ont été testés dans cette thèse, désignés Version 1 (V1) et Version 2 (V2). Version 1 a permis les essais initiaux et la visualisation de la propagation de l'onde du plasma soutenu par laser (LSP). Un prototype d'un propulseur réel, Version 2 a été optimisé pour les essais de poussée. Le processus de conception du propulseur amélioré V2 est également présenté. Ces propulseurs ont été alimentés par un laser à fibre de 1.07 µm ayant une puissance ondes continues (CW) de 300 W et une puissance à ondes quasi continues (QCW) de 3 kW. L'argon a été utilisé comme gaz propulseur à une pression de 20 bar, sélectionné pour sa facilité d'ionisation. Utilisant une bobine de type automobile, l'amorçage par étincelle du LSP QCW a été implémenté avec succès dans V1 et V2. L'ensemencement de l'argon avec du dioxyde d'azote (NO_2) à des pressions partielles comprises entre 0.12 bar et 0.55 bar a montré que le gaz absorbait plus du double de l'énergie laser par rapport au propergol d'argon pur. Pour augmenter le flux laser vers le plasma, un système optique composé de deux lentilles a été conçu. Différentes lentilles ont été comparées à l'aide d'un logiciel de traçage de rayons (WinLens3D). Un LSP CW a été obtenu avec V2, d'une durée de 85.1 ms. Cela représente une durée de vie 1.7 fois plus longue que la longueur d'impulsion QCW maximale de 50.0 ms à cette puissance. La poussée moyenne à froid de V2 était approximativement 1 N. Afin d'interpréter les résultats expérimentaux, un modèle de transfert de chaleur zéro dimension (0D) a été écrit en Python, en utilisant le Bremsstrahlung comme mécanisme de radiation. Enfin, des pistes

pour améliorer encore le propulseur V2 et le banc d'essai de poussée sont présentées pour permettre à terme des mesures de poussée précises avec un fonctionnement CW.

ACKNOWLEDGEMENTS

First, I want to thank my supervisor Professor Andrew J. Higgins for his deep knowledge, mentorship, and support throughout this journey. He gave me and our lab the singular opportunity to pursue graduate studies on advanced space propulsion. In Canada, this is a rare topic of research indeed, but it is only with advances in this field that humanity will be able to reach the stars.

I'm very grateful to my family and Anna for their support and encouragement during my studies.

I would like to extend my heartfelt appreciation to the members of the McGill Interstellar Flight Experimental Research Group. Emmanuel Duplay and Siera Riel, in the pursuit of science together, you have given me dear memories that will last a lifetime. Siera helped with many measurements in the lab, including quasi-continuous wave (QCW) and flowing thrust experiments. She also helped with the design of the Version 2 (V2) thruster and produced the drawings of its new parts. I wish Siera and Anthony Côté much success in continuing the work Emmanuel and I have but started.

Editorial help was provided by Professor Higgins, Emmanuel, Siera, John Kokkalis, and Sebastian Rodriguez. Sebastian helped manufacture the V2 electrodes. Thank you for your knowledge on how to do things in the lab. Thariq Meulendijks did the needle valve A^* calibration and the bubble flow meter experiments and calculations.

Alain Halbouny, Jade Tabbara, Karl Atallah, Serge Rubeiz, and Shady Tawil designed and assembled the V2 laser-thermal thruster, as well as produced its drawings and renders. Thank you to Meisam Aghajani, Mathieu Beauchesne, Ramnarine Harihar (Harry), and Andy Hofmann, the machinists who built V2. Without it, we would not have the experi-

mental insights we have today.

Outside the lab, I want to acknowledge the colleagues that helped make my short stay at McGill even more enjoyable and memorable: Ali Al Abed, Niloy Barua, Caileigh Bates, Andrew Behling, Léa Bernard, Dylan Caverly, Alexandre Courtis, Philippe Decoste, Xavier Duchesne, Ella Godun, Anushka Goyal, Rik Keizer, Mathias Larroutuou, Leah Lavoie, Jana Mouchaimech, Dan-Cornelius Savu, Taj Sobral, Emma Sinasac, Arnab Sinha, and Maximilian Van der Wee.

This work was funded by the Natural Sciences and Engineering Research Council of Canada (NSERC) Canada Graduate Scholarships — Master’s (CGS-M) program and the McGill Summer Undergraduate Research in Engineering (SURE) program.

Chapter 1

Introduction

1.1 Motivation

In 2016, Lubin [1] proposed sending 1 g space probes to Alpha Centauri at 20 % the speed of light, using massive ground-based laser arrays. This could be enabled by a Moore's law in fiber laser technology, with a rapid doubling of power and a similar exponential decrease in costs.

As a near-term stepping stone using a smaller array, the laser can be coupled to a gas, reducing specific impulse but increasing thrust. This process, Laser-Thermal Propulsion (LTP), would allow rapid interplanetary transfers, notably to Mars. The concept of LTP was first suggested by Kantrowitz [2] as a way to decrease launch costs and continues to be of interest. A conceptual design of an LTP spacecraft was proposed by Duplay *et al.* [3], with a similar architecture to Lubin [1]: a 10 m laser array beams 100 MW of power to an orbiting spacecraft for injection burns (Figure 1.1). With a 1 ton payload, 6 kN of thrust and 3000 s of I_{sp} , a 1 h laser beaming maneuver gives 14 km/s of delta-V to the spacecraft, which reaches Mars in 45 days.

Initially, hydrogen propellant is introduced in the thrust chamber of the vehicle. The laser is focused inside the chamber (see Figure 1.2) and is absorbed by the gas via inverse Bremsstrahlung, creating a Laser-Sustained Plasma (LSP) core. Colder hydrogen flows around the LSP core and is heated by it to 10 000 K. The hot gas is then exhausted through a conventional converging-diverging nozzle at the exhaust velocity, imparting thrust to the vehicle.

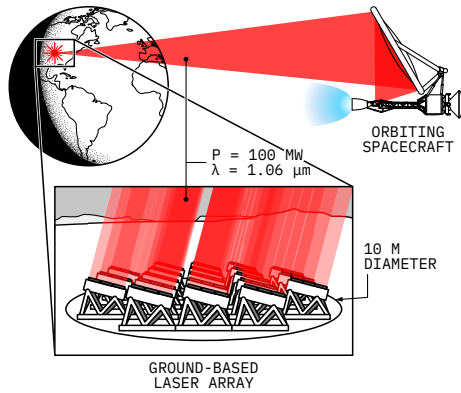


Figure 1.1: LTP architecture (Duplay [4])

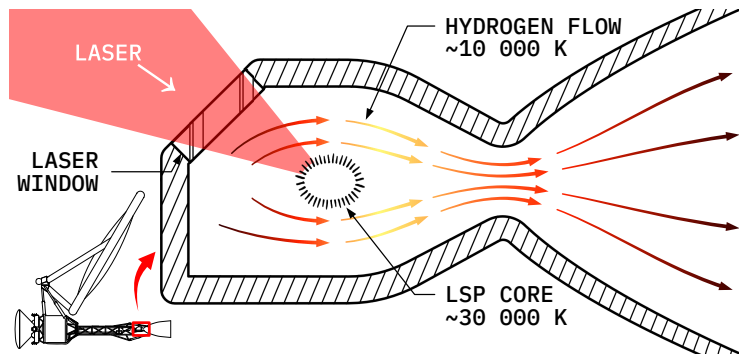


Figure 1.2: Overview of LTP system (Duplay [4])

In a conventional chemical rocket engine, the energy source is the oxidizer and the fuel, which are reacted together to release energy. They are transported with the rocket and set the temperature of the combustion reaction (typically 2000 K to 3000 K), which is directly related to the exhaust velocity.

Separating the power source used for propulsion (here, the laser) from the spacecraft itself allows crucial weight savings, either increasing the payload mass fraction or decreasing transit time. Using a laser also allows for much greater thrust chamber temperatures than chemical propulsion, as the temperature of these plasmas is typically 15 000 K to 30 000 K. This gives in turn greater exhaust velocities. This propulsion method could therefore be an order of magnitude more efficient than our current rocket engines if certain engineering problems can be solved.

Increasing the amount of energy deposited by the laser into the propellant remains a topic of active research and is a significant hurdle for the operational use of LTP. The two main conversion efficiencies are:

1. Absorption of the laser energy by the plasma
2. Heat transfer from the plasma to the propellant

A selection of past LSP experiments will now be presented, with an emphasis on these efficiencies. As the efficiencies chosen are different from source to source, they will be defined where applicable.

1.2 Literature review

The experimental basis of LTP was developed by Generalov *et al.* [5] in 1970. For the first time, an LSP was generated with a 150 W CO₂ laser operating at a 10.6 μm wavelength. In this case, the LSP was initiated by a second, 10 kW pulsed CO₂ laser.

Work was done in the mid-1970s by Shoji [6] and Shoji and Larson [7] to design a small-scale 10 kW and full-scale 5000 kW LTP engine. Carbon-seeded hydrogen was proposed to capture the plasma's radiation, which was mostly in the UV wavelength. 20 % of the laser power would be lost by convection and radiation to the walls in the 10 kW thruster, with an additional 5 % of laser power lost by radiation through the thruster window. However, these engines were not tested. The 10 kW prototype (Figure 1.3) was built and delivered to NASA at the conclusion of their effort. Photographs of the assembled apparatus and its parts can be found in Shoji and Larson [7].

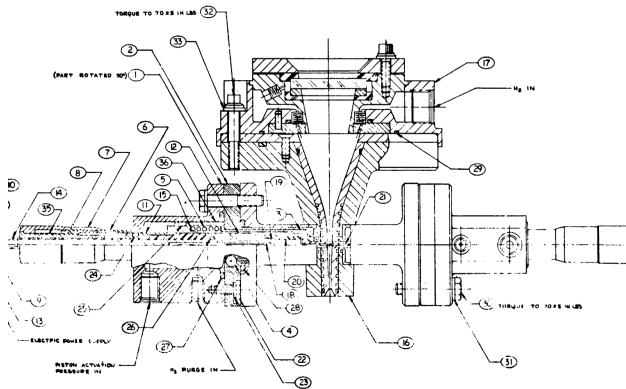


Figure 1.3: Cross-section drawing of 10 kW thruster from Shoji [6] (original is of poor quality)

In the 1980s, Keefer *et al.* [8] studied LSP in a forced convective flow environment. Using a 1.5 kW CO₂ laser with power levels of 360 W to 840 W and pressures of 1.3 atm to 2.3 atm, with varying argon flow velocities, the temperature field of the plasma was measured. From

the temperature field, and assuming local thermodynamic equilibrium, the power absorbed by the plasma and the power radiated from it can be calculated. [Figure 1.4](#) shows the ap-

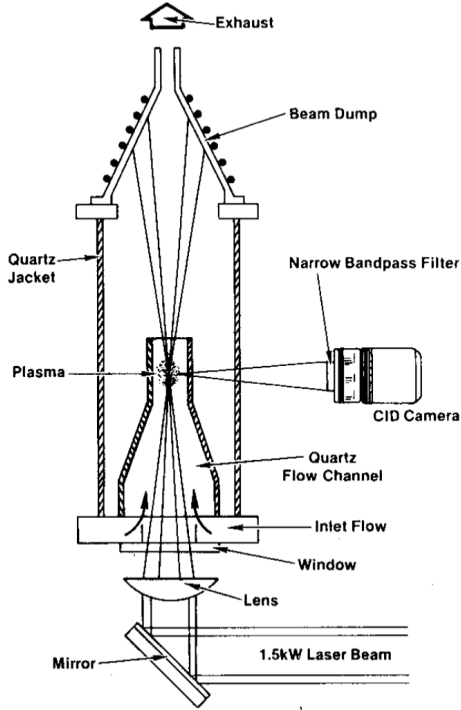


Figure 1.4: Experimental apparatus from Keefer *et al.* [8]

paratus used for these measurements. An inner quartz flow channel contained the plasma, while an outer quartz jacket contained the pressure. The plasma was initiated by laser heating of a tungsten rod, which was removed after initiation. Downstream, a water-cooled copper beam dump absorbed the energy of the laser and the heated argon flow, but it was not used for any measurements. The plasma's temperature was obtained through analyzing digital images. This temperature field was then used to calculate the power absorption and the radiation loss. The power absorbed by the plasma was between 23 % to 61 % of incident laser power, while the radiation loss was between 51 % to 80 % of the absorbed power.

Contemporary to Keefer *et al.* [8], Mazumder and Krier headed a group at the University of Illinois that advanced the field of LTP. Krier *et al.* [9] reported laser absorption in an argon plasma approaching 80 %. [Figure 1.5](#) shows the apparatus that was used by Krier *et al.* [9], Zerkle *et al.* [10], and Chen and Mazumder [11]. This vertical cylindrical flow chamber was made of 304 steel and had an internal diameter of 5 inches. A water-cooled calorimeter was used as a beam dump for the 10 kW CO₂ laser. The laser energy not collected by the calorimeter (beam dump) was assumed to be absorbed by the plasma, as

the radiation reflected off the plasma is less than 2 % at these electron number densities. Moveable thermocouples gave a two-dimensional map of the flow surrounding the plasma core. The direct laser heating of the thermocouples and their carriage was taken into account. With the two-dimensional temperature map, the change in enthalpy at the exit plane

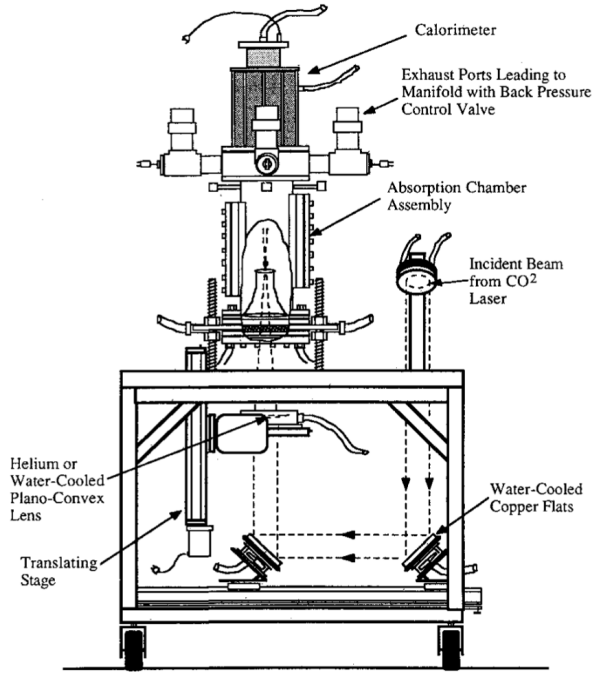


Figure 1.5: Experimental apparatus from Zerkle *et al.* [10]

was calculated, giving the amount of laser energy retained by the gas. Thermal efficiency was between 6 % to 25 %, with radiative losses of 64 % and 30 %, respectively. Thermal efficiency was defined as:

$$\eta_{\text{th}} = \frac{\text{Power retained by the gas}}{\text{Incident laser power}} \quad (1.1)$$

The minimum maintenance intensity of the plasma was also estimated at 0.1 MW/cm^2 to 0.3 MW/cm^2 .

Further work by Zerkle *et al.* [10] with the apparatus shown in Figure 1.5 reported absorption from 55 % to 97 % and thermal efficiency from 11 % to 46 %. This was done in 12.5 atm of flowing argon, with laser powers up to 7 kW. Chen and Mazumder [11] again increased the thermal efficiency of this apparatus, with 41 % to 62 % of the laser energy being retained by the gas as thermal energy. This was among the highest thermal efficiencies measured by an LSP experiment. Here, 86 % of the laser's energy is absorbed by the

1. INTRODUCTION

1.2. LITERATURE REVIEW

LSP. This was attained with a 5 kW CO₂ laser, with flow speeds between 2 m/s to 10 m/s. They discuss that greater thermal efficiency is due to greater laser power, a high enough flow speed, and a greater laser focusing *f* number.

Based on work by the Illinois group, an LTP engine demonstrator was tested in 1995 by Black *et al.* [12] with a 10 kW CO₂ laser. This was planned to be a step towards a full-scale thruster. More than 100 thruster firings were completed, lasting 1 to 2 minutes each. The 10 kW thruster is presented in Figure 1.6a. It is mounted in a vacuum chamber to a thrust measurement assembly. Efficiency was calculated from:

$$\eta = \frac{F^2}{2\dot{m}P_L} \quad (1.2)$$

with P_L the input laser power at the thruster window. Both argon and hydrogen were used. Argon propellant produced 200 s of I_{sp} and a peak efficiency of 0.24. With hydrogen propellant, an I_{sp} of 350 s and a peak efficiency of 0.37 were reported. A preliminary design

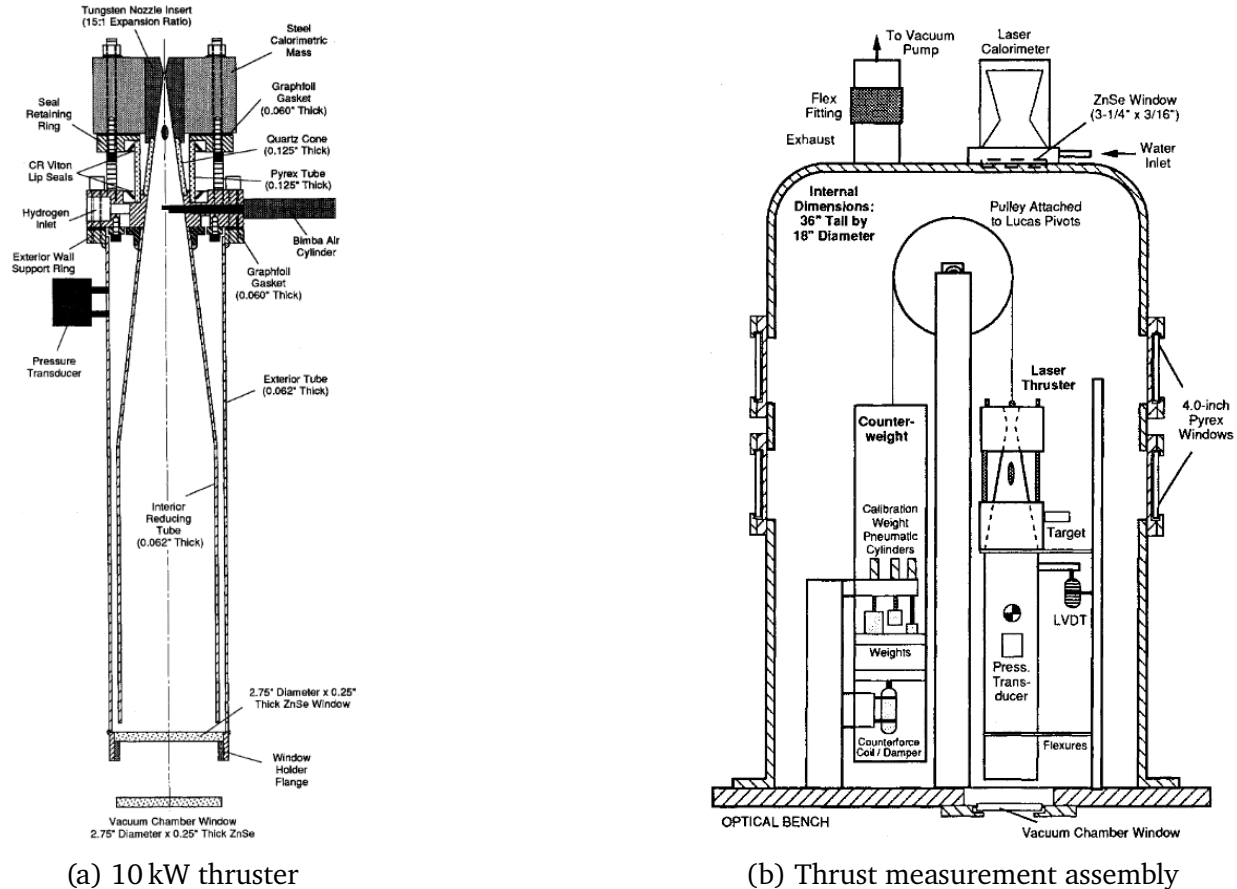


Figure 1.6: Apparatus used in Black *et al.* [12]

for the full-scale 100 kW thruster was also presented, with a predicted specific impulse of 1000 s, thrust of 4.5 N and a conversion efficiency of 80 %.

In the early 2000s, Toyoda *et al.* [13] built and tested two different thruster models, presented in Figure 1.7. These thrusters, using argon or nitrogen heated by LSP, were powered by a 2 kW CO₂ laser. The LSPs were initiated by a retractable tungsten rod at the laser's focus. Thrust measurements were done both in atmospheric pressure and in vacuum. This comparative study showed that confining the plasma into a smaller chamber increased thrust and therefore, efficiency. Toyoda *et al.* [13] defined the energy conversion efficiency as the amount of laser power that is converted into usable kinetic energy for thrust. It is calculated as¹:

$$\eta_e = \frac{F_{\text{hot}}^2 - F_{\text{cold}}^2}{2\dot{m}P} \quad (1.3)$$

Where F_{hot} is the thrust with laser on, F_{cold} is the cold flow thrust (laser off) and P is incident laser power. An energy conversion efficiency of 37% and an I_{sp} of 113 s were measured with the second model Figure 1.7b in vacuum with argon propellant. The pressure ratio, defined as the chamber pressure divided by the nozzle exit pressure, was 420. A water cooling system measured the heat loss to the walls to be 55% of incident laser power, with a final 8% being “other loss”. Heat loss to the walls was expected to be recycled with regenerative cooling in a real-world application.

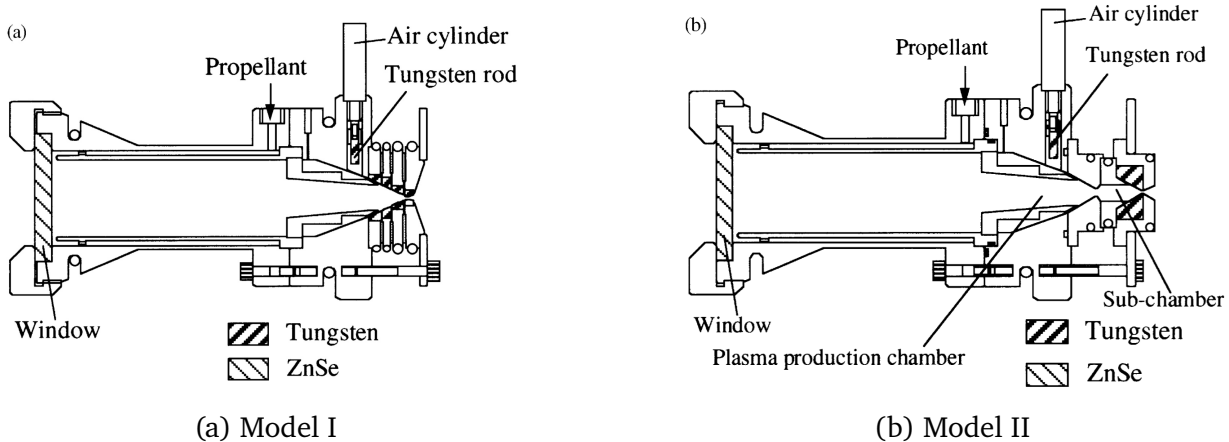


Figure 1.7: Two thruster models from Toyoda *et al.* [13]

Lu *et al.* [14] investigated LSP for lighting applications instead of propulsion. Therefore, an emphasis was made on spectroscopy measurements. A 300 W fiber laser at a wavelength of 1080 nm was focused to a 50 μm diameter spot in a high pressure chamber. Argon was

¹As mentioned by Duplay [4], there appears to be a typographical error in the reference as the units are inconsistent. The corrected equation is presented here.

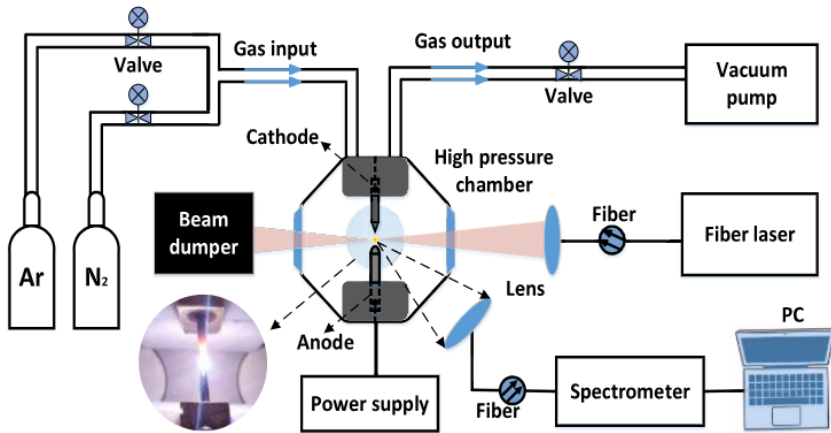


Figure 1.8: Experimental setup from Lu *et al.* [14]

used, with pressures between 10 bar to 20 bar. A lower initiation power (117 W) than other studies was achieved at 20 bar. This was attributed to the smaller focus delivering a greater photon flux. N_2 was later added between 0.1 % to 1.0 %. As expected, increasing the laser power or the gas pressure was found to increase the radiation intensity of the LSP. However, adding N_2 reduced both the electron temperature and electron density of the LSP, reducing its radiation intensity.

Seeding the propellant with another species has been discussed as a way to increase the energy absorption into the working fluid of an LTP engine. LSPs in pure methane and methane-seeded gasses have been investigated by Kamei *et al.* [15]. Methane dissociates into hydrogen and carbon with the high temperature of the LSP. As mentioned by Shoji [6], carbon particles would absorb the LSP's UV radiation. A 1.1 kW diode laser at a wavelength of 940 nm was beamed into a high-pressure chamber fitted with arc initiation electrodes. The gap between these electrodes was 1 mm. A CCD type spectrometer recorded emission spectra of the initiation arc discharge and of the LSP. LSPs in three different gasses were attempted: pure methane, methane-argon, and methane-xenon.

In methane at 0.1 MPa, soot formation between the electrodes prevented LSP initiation. The spectrometer confirmed the dissociation of methane, as line spectra of carbon and hydrogen were observed at the initiation arc. Initiation was also unsuccessful in argon-methane with a pressure between 0.1 MPa to 0.3 MPa and a methane volume fraction between 20 % to 60 %. LSP was successfully generated in methane-xenon, with a lower threshold power (850 W) than in pure xenon. The partial pressure of methane was between 0.02 MPa to 0.6 MPa, with a partial pressure of xenon of 0.10 MPa.

Takano *et al.* [16] used a diode laser emitting simultaneously at 927 nm and 951 nm to generate LSPs in argon. This resulted in an I_{sp} of 105 s and a thrust efficiency of 8 %. This I_{sp} was calculated from the plenum pressure when the laser was on. They define thrust efficiency as:

$$\eta = \frac{g_0 I_{sp} (F_{hot} - F_{cold})}{2P_{laser}} \quad (1.4)$$

Two setups were used: the LSP generation chamber previously used by Kamei *et al.* [15] (Figure 1.9a) and an LSP thruster (Figure 1.9b). The LSP chamber was used to determine

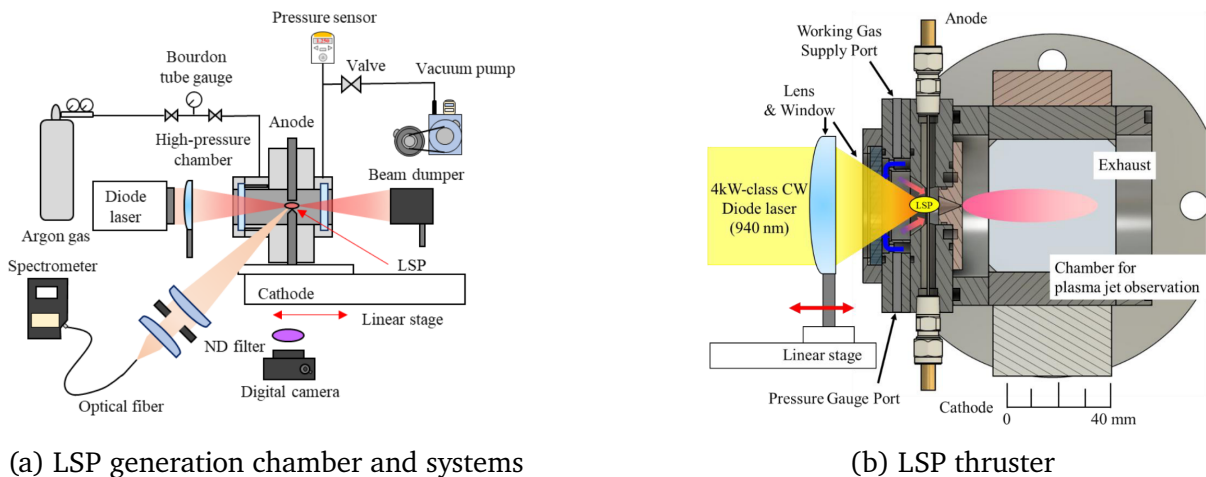


Figure 1.9: LSP setups from Takano *et al.* [16]

the effect of various F-numbers on the argon LSP. The thruster has an interchangeable copper throat, with diameters of 0.7 mm and 1.0 mm. In both setups, electric arc initiation was used. Once initiated in the thruster, the LSP is moved toward the nozzle with the lens mounted on a motorized stage. It was found that moving the LSP this way increased the heat exchange with the propellant. Thrust was calculated by using the pressure measurements inside the thruster's heating chamber.

Duplay [4] used a 3 kW pulsed fiber laser to create LSPs in static and flowing argon. In static argon, about 80 % of the laser energy was being absorbed by the plasma, with approximately 15 % of the laser energy heating the bulk gas. This was done between 5 bar to 20 bar.

1.3 Summary and direction of work in this thesis

From the literature review, [Table 1.1](#) and [Table 1.2](#) were compiled. Most studies have used CO₂ lasers with a wavelength of 10.6 μm. As a laser beam advances in space, it diffracts. This leads to a larger spot size the farther it is focused, even with ideal optics. The range L at which the laser's spot size is equal to its emitter size is derived by Lubin [\[1\]](#):

$$L = \frac{dD}{2\lambda\alpha} \quad (1.5)$$

With d the diameter of the laser aperture, D the diameter of the laser receiver, and $\alpha = 1.22$ for a circular array, deriving from the first zero of the J_1 Bessel function. A smaller wavelength (λ) gives a larger value of L , as the beam diverges less. Use of a CO₂ laser for power beaming to a remote target for propulsion applications is limited to ground-to-orbit launch. However, high power fiber lasers emitting near 1 μm have recently become readily available. Being able to beam energy ten times farther than CO₂ lasers, fiber lasers make laser propulsion more feasible.

To increase thermal efficiency, Chen and Mazumder [\[11\]](#) suggest:

1. A greater laser power to increase electron temperature, which gives greater inverse bremsstrahlung absorption coefficient and longer absorption path length;
2. A high enough flow speed to push the LSP back to the laser focus, but not too fast as to blow the plasma out;
3. A greater laser focusing f number, creating a longer and narrower plasma. This increases the probability that a photon from the laser will be absorbed by the plasma and reduces the radiation loss.

For a small-scale, demonstration thruster, I_{sp} values near 100 s can be expected, with thrust values under 1 N, as was found by Toyoda *et al.* [\[13\]](#) and Takano *et al.* [\[16\]](#).

The objective of this research project will be to test a Version 1 (V1) lab-scale LTP thruster, as well as design and test an improved Version 2 (V2) thruster. These will be both powered by a 1.07 μm fiber laser. This project will mainly build upon the experimental research started by Duplay [\[4\]](#) with the V1 thruster.

Table 1.1: Summary of a selection of past LSP experiments. λ : wavelength, P : maximum laser power, p : pressure, I_{sp} : maximum specific impulse, F_T : maximum thrust

LSP Facility	Year	Laser	λ [μm]	P [kW]	Gas	p [bar]	I_{sp} [s]	F_T [N]
Generalov <i>et al.</i> [5]	1970	CO_2	10.60	0.15	Xe	1.0–10.1	-	-
Keefer <i>et al.</i> [8]	1986	CO_2	10.60	0.84	Ar	1.3–2.3	-	-
Krier <i>et al.</i> [9]	1986	CO_2	10.60	10.0	Ar	1.1–3.5	-	-
Zerkle <i>et al.</i> [10]	1988	CO_2	10.60	7.0	Ar	1.0–2.5	-	-
Chen and Mazumder [11]	1989	CO_2	10.60	5.0	Ar	1.0	-	-
Black <i>et al.</i> [12]	1995	CO_2	10.60	10.0	Ar	0.9–2.6	200	7.0
Toyoda <i>et al.</i> [13]	2002	CO_2	10.60	10.0	H_2	1.9–3.4	350	3.6
		CO_2	10.60	2.0	Ar, N_2	2.0–5.6	113	0.44
Lu <i>et al.</i> [14]	2022	Fiber	1.08	0.30	Ar, N_2	10.0–20.0	-	-
Takano <i>et al.</i> [16]	2024	Diode	0.927 and 0.951	4.4	Ar	6.0–20.0	105	-
Duplay [4]	2024	Fiber	1.07	3.0	Ar	3.0–20.0	-	-

Table 1.2: Comparative table of experimental LTP thruster efficiencies

LSP Facility	Fraction of laser power absorbed	Efficiency formula	Value of efficiency
Keefer <i>et al.</i> [8]	0.23–0.61	-	-
Krier <i>et al.</i> [9]	0.50–0.80	$\eta_{\text{th}} = \frac{\text{Power retained by the gas}}{\text{Incident laser power}}$	0.06–0.25
Zerkle <i>et al.</i> [10]	0.55–0.97	$\eta_{\text{th}} = \frac{\text{Power retained by the gas}}{\text{Incident laser power}}$	0.11–0.46
Chen and Mazumder [11]	0.86	$\eta_{\text{th}} = \frac{\text{Power retained by the gas}}{\text{Incident laser power}}$	0.41–0.62
Black <i>et al.</i> [12]	-	$\eta = \frac{F_{\text{hot}}^2}{2\dot{m}P_{\text{L}}}$	0.18–0.24 (Ar), 0.25–0.37 (H ₂)
Toyoda <i>et al.</i> [13]	-	$\eta_{\text{e}} = \frac{F_{\text{hot}}^2 - F_{\text{cold}}^2}{2\dot{m}P}$	0.37
Takano <i>et al.</i> [16]	-	$\eta = \frac{g_0 I_{\text{sp}} (F_{\text{hot}} - F_{\text{cold}})}{2P_{\text{laser}}}$	0.08
Duplay [4]	0.79	$\eta_{\text{th}} = \frac{\text{Power retained by the gas}}{\text{Incident laser power}}$	0.15

Chapter 2

Facility design

2.1 Version 1 test section design

The design process of the first generation thruster, called Version 1 (V1, see [Figure 2.1](#)), can be found in Duplay [4]. It proved to be a dependable prototype for studying LSP initiation, repurposed from a previous unrelated experiment. However, it presented problems related to operation as a thruster. Indeed, it was too heavy for thrust measurement and its length put fragile rubber seals in the path of the laser beam. Its large internal volume also meant that the increase in thrust and chamber pressure with LSP would be minimal. This required a second generation prototype to be designed and manufactured.

A total of 298 recorded pulsed laser shots were conducted with V1, exploring the power-pressure threshold, wire initiation and spark initiation. A side window permitted direct visualization of the LSP with a high-speed camera (Photron Fastcam SA5).

2.2 Version 2 test section design

To improve upon the V1 facility, an entire LTP thruster redesign was done. This resulted in the much smaller Version 2 (V2) purpose-built LTP thruster, seen in [Figure 2.2](#). The part and assembly drawings for V2 are found in [Appendix D](#).

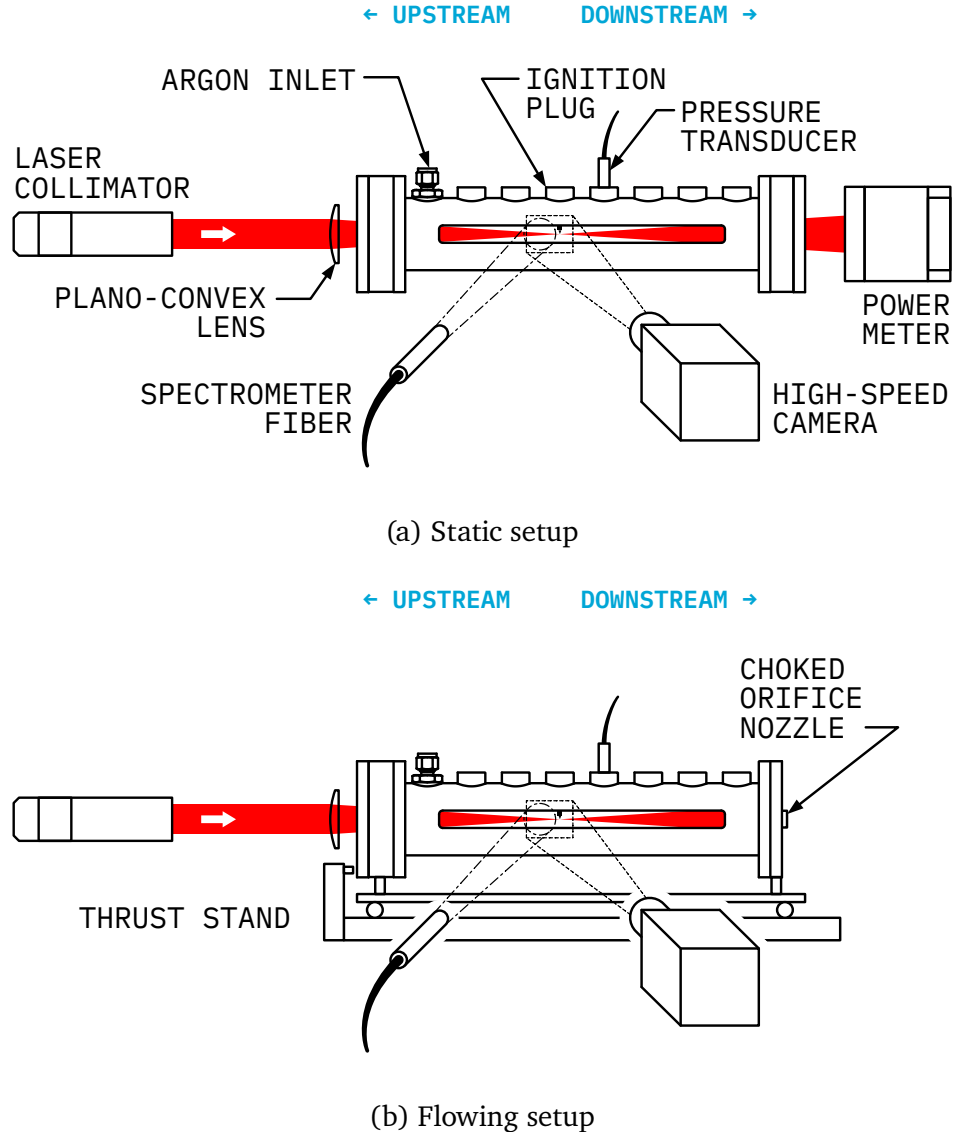


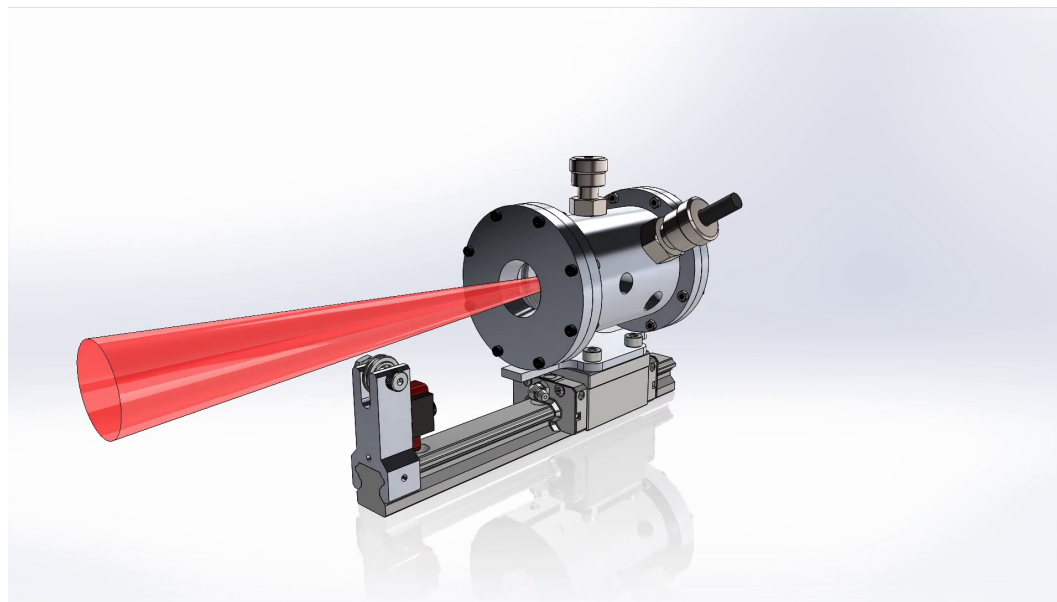
Figure 2.1: V1 LTP thruster from Duplay [4]

2.2.1 Requirements for the version 2 test section

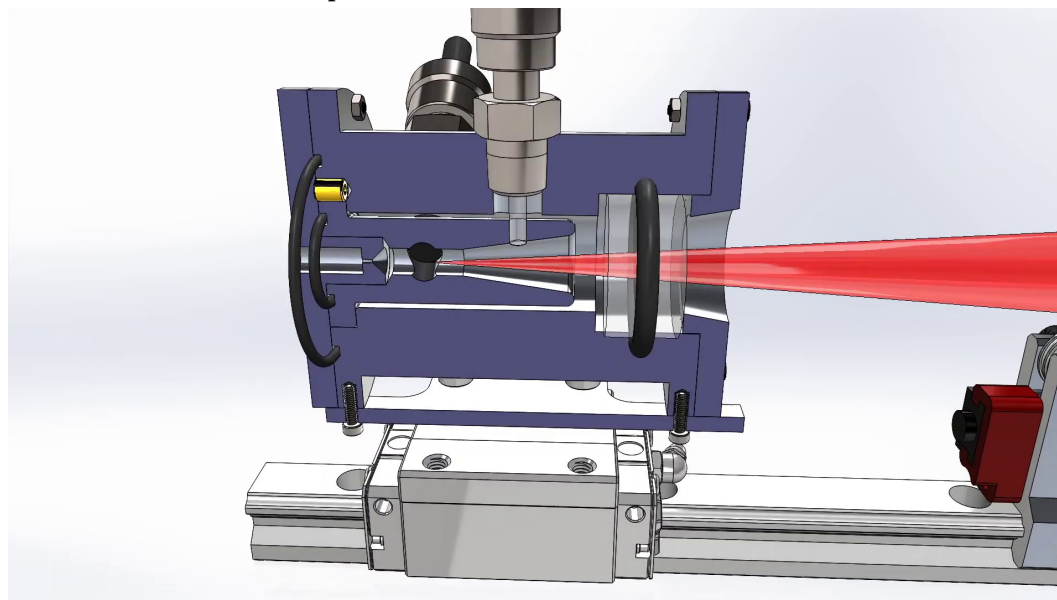
The following requirements were developed for the design of the V2 thruster. The objective was to detect a measurable difference in thrust between an argon cold gas thruster and an argon “hot gas” thruster, heated by LSP.

1. Laser thruster

- (a) A 300 W Continuous Wave (CW) 1070 nm laser will be used to sustain the plasma (nominal power 300 W, actual max power 350 W)



(a) View of the laser path (in red) and thruster mounted on its thrust stand



(b) Cutaway view of the inside of the thruster

Figure 2.2: Renders of the V2 LTP thruster

- (b) The thruster should have a minimum safe “hot” operation time of 30 s
 - i. In the event of failed LSP initiation, the thruster will safely absorb the total laser power for at least 10 s
- (c) An optical path is required to be present to let the laser into the thruster, utilizing a 100 mm focal length lens at minimum and a collimated beam with a maximum diameter of 30 mm

- i. The optical components will not be damaged by the laser flux
 - (d) Argon will be used as the working fluid
 - i. The argon feed gas will be at room temperature
 - (e) A gas feed path brings argon gas into the thruster
 - i. The gas feed is choked at the thruster inlet
 - ii. The gas feed will be evenly distributed in the thruster
 - (f) The mass flow rate of the argon gas will be measured and controlled by interchangeable upstream choked orifices
 - (g) The Maximum Allowable Operating Pressure (MAOP) of the thruster will be 50 bar
 - i. The nominal pressure of the thruster will be 25 bar
 - (h) A converging-diverging exhaust nozzle will be designed to accelerate the gas to a supersonic speed
 - i. The nozzle will be easily changeable
 - (i) A 1/8" NPT port for a pressure transducer will be present along the thruster
 - (j) An optical port will be present for spectrometry measurements of the plasma
 - (k) The thruster will be installed on a thrust stand (See requirements section 3. Thrust stand)
2. Initiation system/electrical
- (a) The LSP is initiated by an electrical spark
 - (b) The spark gap will be measurable, controllable, and repeatable
 - (c) The spark is to be generated by an AEM 30-2853 High Output Smart Coil, supplying 41 kV with up to 118 mJ
 - (d) All parts of the thruster and thrust stand should be directly or indirectly connected to a common electrical ground
3. Thrust stand
- (a) The thrust stand measures thrust on the order of 0.1 N to 5 N
 - (b) The thrust stand minimizes friction losses

- (c) The thrust stand will be securely fixed using standard optical breadboard mounting hardware

With these requirements, preliminary geometric dimensions of the V2 thruster could commence. It was expected to be much smaller than V1, as the goal was to isolate the LSP region and increase heat flux to the gas.

2.2.2 Initial sizing of the double choked laser-thermal propulsion thruster

The minimum diameter of the cylinder that will contain the LSP core must be larger than the diameter of the plasma itself, which is 2 mm according to observations from Duplay [4]. An arbitrary factor of safety of 2.5 was used, which set the innermost diameter to 5 mm.

The argon gas enters radially near the end of the thruster. A channel around the inner cylinder directs the gas to the front of the thruster, where it turns 180° towards the plasma region and out the nozzle (see [Figure 2.3](#)). This “cylinder-inside-a-cylinder” design was inspired by Toyoda *et al.* [13], allowing the gas to cool the inner cylinder and straightening the flow. The thickness of the exterior wall of the thruster was determined by the minimum engagement depth (14 mm) of the 1/4 inch Ultra-Torr NPT fittings.

The required metering valve and nozzle orifice sizes were then estimated. When adding energy to the thruster chamber with a laser, it is useful to choke the inflow upstream of the chamber. Indeed, this keeps the P_0 and \dot{m}_{in} constant, so the increase in chamber pressure can be interpreted as a measure of energy deposition. The second choke happens at the nozzle to accelerate the hot gas to a supersonic speed. Therefore, this configuration is double choked (see [Figure 2.3](#)), a classic problem in compressible fluid mechanics.

The starting assumptions were the following: a fixed 300 W power input (the laser) supplies energy to an LTP experiment that has an internal pressure of 25 bar, with a 50 bar feed pressure. It is required that the hot gas operation (laser on) increases the gas’ exit velocity to twice that of the cold gas operation (laser off). The gas mass flow rate and the diameter of the two orifices needed to choke the flow will be determined.

Starting with a cold gas thruster using argon, the speed of sound of argon (c_0) is 323 m/s. This is at ambient temperature $T_1 = 300$ K, as there is no laser energy to heat the gas in this case. With a nozzle, the gas is accelerated to approximately twice this speed. The exit velocity of the gas v_{exit} , which is the main performance parameter, is therefore 646 m/s.

Laser on (hot) operation will now be examined, with the assumption that there is perfect conversion of laser power to gas heating. To see an effect on thrust that was significant, the

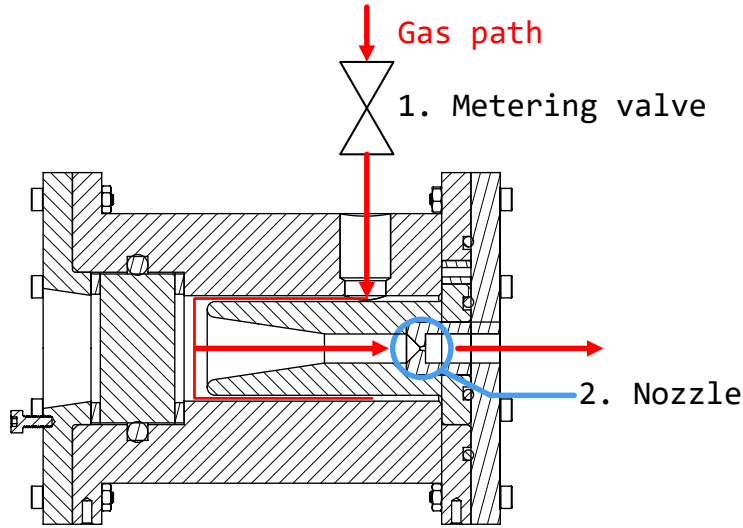


Figure 2.3: Cutaway of the V2 double choked LTP thruster showing both choking orifices: the metering valve and the nozzle. Ports other than the argon inlet are omitted for clarity.

mass flow was set such that the thrust would be doubled with a fixed mass flow rate. The exit velocity is therefore doubled, giving a $v_{\text{exit}} \approx 1300 \text{ m/s}$. With a fixed nozzle and mass flow, the speed of sound in the gas must increase by a factor of two. As the speed of sound is $c = \sqrt{\gamma RT}$, the temperature after ionization (T_2) is estimated to be four times larger than T_1 .

$$\text{Power} = \dot{m}(h_2 - h_1) = \dot{m}c_p(T_2 - T_1) \quad (2.1)$$

Using a constant c_p of argon of $0.520 \text{ kJ kg}^{-1} \text{ K}^{-1}$, the calculated \dot{m} is 0.641 g/s . The nozzle throat size will then be found for this \dot{m} , with $p_0 = 25 \text{ bar}$. $\text{MW}_{\text{Ar}} = 40 \text{ g/mol}$ is known. Fliegner's formula describes the mass flow rate of an isentropic flow:

$$\frac{\dot{m}}{A} = p_0 \sqrt{\frac{\gamma}{T_0 R}} \frac{M}{\left(1 + \frac{\gamma-1}{2} M^2\right)^{\left(\frac{\gamma+1}{2(\gamma-1)}\right)}} \quad (2.2)$$

With $\gamma = \frac{c_p}{c_v} = 1.67$ for argon and choked flow at the nozzle ($M = 1$), the area and the diameter of the circular nozzle are 0.176 mm^2 and 0.473 mm , respectively. The V2 test section was built with this nozzle diameter. These calculations can be repeated for the feed orifice, with the same \dot{m} , a pressure of 50 bar and ambient temperature. This gives us an

orifice diameter of about 0.2 mm.

2.2.3 Test section and thrust stand

As can be seen in [Figure 2.4](#), the V2 test section was designed with multiple ports for modularity, enabling static and flowing tests with argon propellant. Ports that were not in use were fitted with pipe plugs. In all tests, the two opposing electrode ports and one argon inlet port were used. The second argon inlet, intended to offer a more uniform flow if needed, was not used. The optical access port was initially fitted with a quartz rod in an Ultra-Torr fitting, but was replaced by a pipe plug after excessive rod breakage due to pressure cycling. After flowing through the test section, used argon propellant was vented to the ambient air. [Figure 2.5](#) shows the two final configurations that were used.

The thrust stand is a ball bearing carriage (McMaster-Carr 6709K12) on a 15 mm wide, 160 mm long guide rail (McMaster-Carr 6709K33). The rail is mounted on the optical breadboard using acrylic spacers. A string through a pulley holds a variable weight, adding a preload to the test section. This ensures adequate contact between the test section and the load cell and allows calibration of the load cell. Two load cells are used with different force sensing ranges: Honeywell FSG020WNPB (0 N to 20 N) and Honeywell FSG005WNPB (0 N to 5 N).

2.2.4 Laser and optics

The laser used as the plasma's power source is an IPG Photonics YLR-300/3000-QCW-MM-AC Ytterbium fiber laser. The wavelength of the emitted light is 1070 nm. Its nominal maximum power is 3 kW quasi-continuous wave (QCW) or 300 W continuous wave (CW). At 3 kW, a QCW pulse has a maximum duration of 10 ms. The maximum duration of a 300 W QCW pulse is 50 ms. The IPG Photonics P30-001736 collimator outputs a 30 mm diameter laser beam. The laser also includes a red visible laser for alignment, which is coaxial to the main beam. These components form the laser system, presented in [Figure 2.6](#).

Calibration reports for the laser and the collimator can be found in [Appendix A](#). The laser is mounted at the base of a freestanding electronics rack ([Figure 2.7](#)).

V2 uses two lenses placed close to each other to focus the laser from the collimator. These are the Thorlabs LA1380-C and LA1417-C N-BK7 plano-convex lenses with a 1050 nm to 1700 nm anti-reflective coating. Their focal lengths of 500 mm and 150 mm, respectively, give a combined focal length of 115 mm. These two lenses are mounted in a single Thorlabs

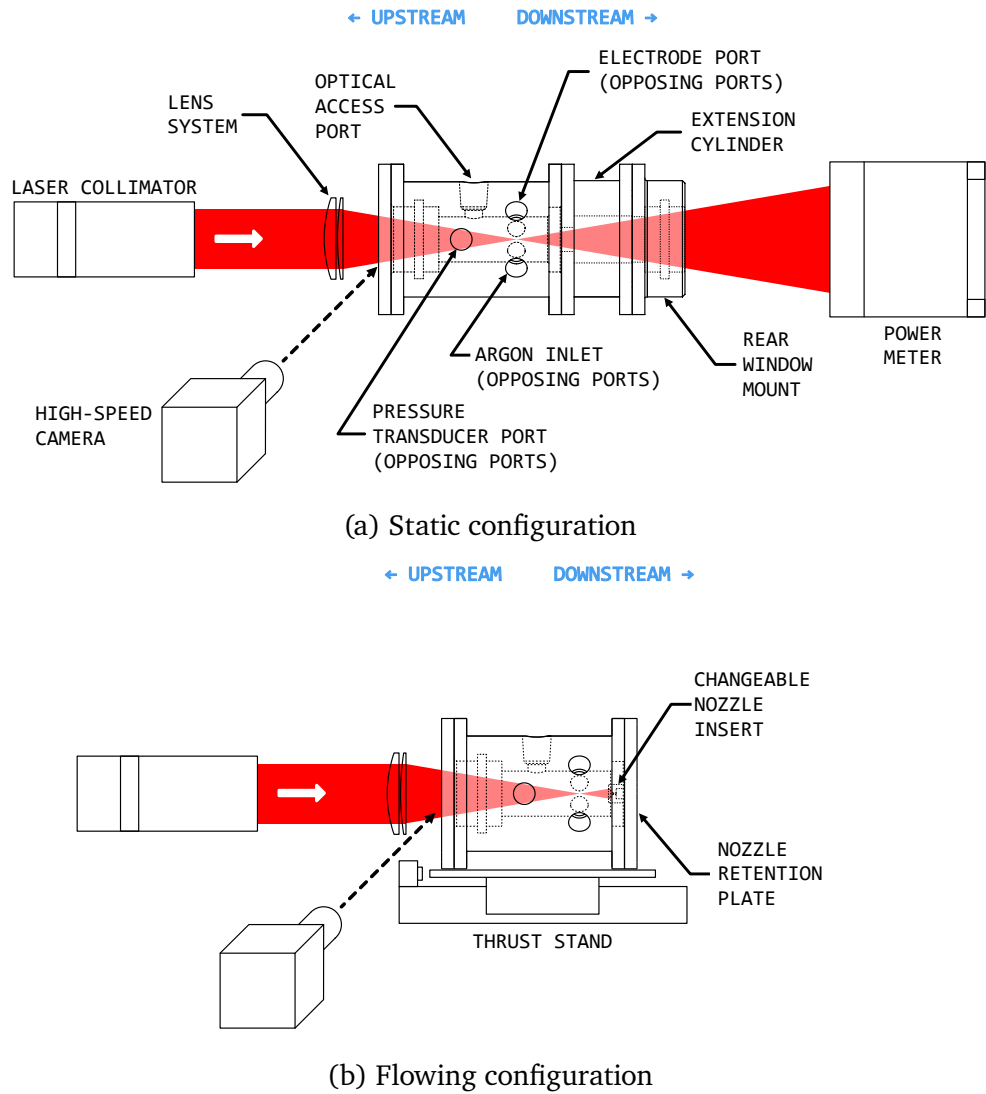
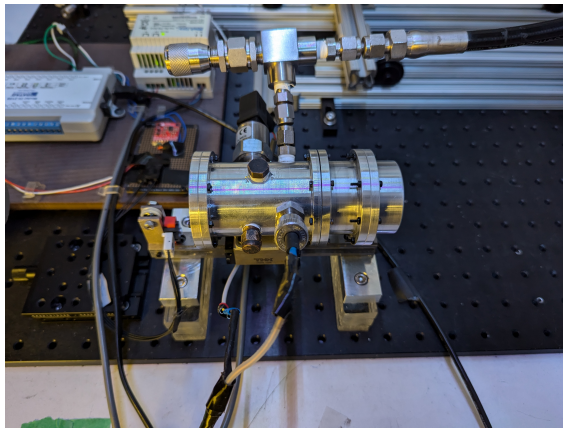


Figure 2.4: V2 LTP thruster

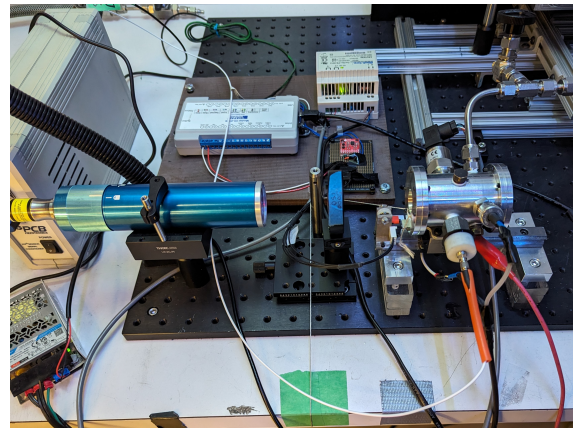
LMR2 lens mount with two retaining rings. A Thorlabs DT12 translation stage enables left-right alignment of the laser focus, while a Thorlabs DTS25 translation stage gives control on the depth (axial position) of the focus.

2.2.5 Timing control

Correct timing of the laser and spark initiation is necessary to initiate LSP. To this end, delay generators are used (BNC models 7010 and 7055) as seen in [Figure 2.8](#). They are mounted at the top of the electronics rack.



(a) Final static configuration. Note the extension part and window mount. Optics and laser collimator are not pictured here but would be installed during testing.



(b) Final flowing configuration. The nozzle is held by the rear plate.

Figure 2.5: V2 LTP thruster



(a) IPG Photonics YLR-300/3000-QCW-MM-AC laser



(b) IPG Photonics P30-001736 collimator

Figure 2.6: Laser system

2.2.6 Data acquisition system and oscilloscope

Load cell and pressure transducer voltage is sent to a DATAQ Instruments DI-2018, on [Figure 2.9](#). This data is streamed to a personal computer by USB, where the thrust and pressure traces can be saved for analysis. Two pressure sensors were used. A PCB Model 113B28 was used for dynamic (transient) pressure measurements, while an Omega PX119A-1KG5V was used for quasi-static measurements. Refer to [Appendix C](#) for the Omega pressure sensor calibration.

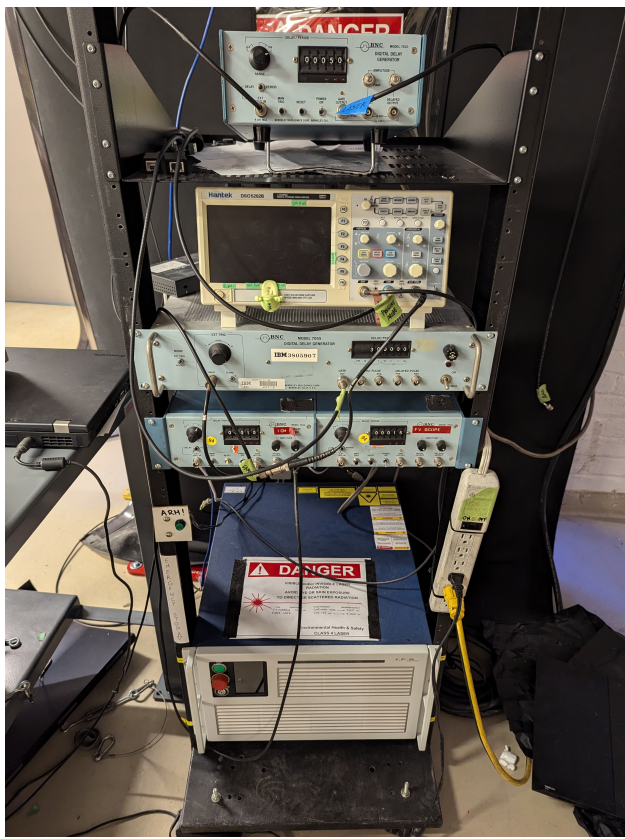


Figure 2.7: Electronics rack with laser at the base

2.2.7 Cameras

A Photron SA5 high-speed camera was used during certain LSP shots to determine if LSP initiation had happened and how long the plasma had lasted. Due to no side windows being present on V2, the Photron camera looked at an angle from the side into the front window, seeing the reflection of the plasma core (as in [Figure 2.4](#)). During LSP shots, the camera's lenses and its sensor were protected by an Aurora PowerXND-II Variable Neutral Density Filter and a Hoya 58 mm UV and IR cut filter.

A generic USB webcam was also connected to the data acquisition laptop, giving a live wide-angle view of the entire experiment. As these cameras are sensitive to IR, it gave an additional confirmation that the laser emission was turned off before opening the laser safety curtain.

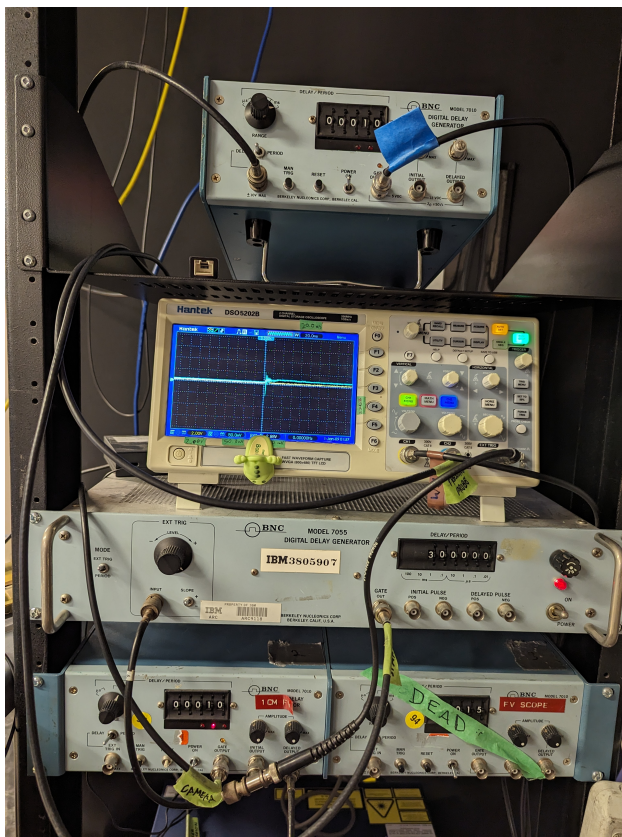


Figure 2.8: Delay generators and oscilloscope

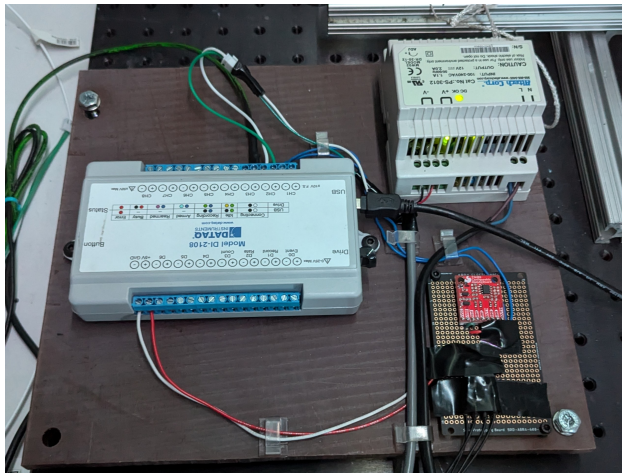


Figure 2.9: Data acquisition (DAQ) system

2.2.8 Spark initiation system

The spark was generated by an AEM 30-2853 High Output Smart Coil, supplied by a 10 A power supply. This automotive-type coil can generate a 40 kV, 103 mJ spark. The trigger signal wire from the delay generator comes in from the left of [Figure 2.10](#). It passes through

the power supply electrical box in a quad shielded coaxial cable. The smart coil is placed in a separate electrical box to reduce electromagnetic interference. The spark energy exits through the cable on the right of [Figure 2.10](#).

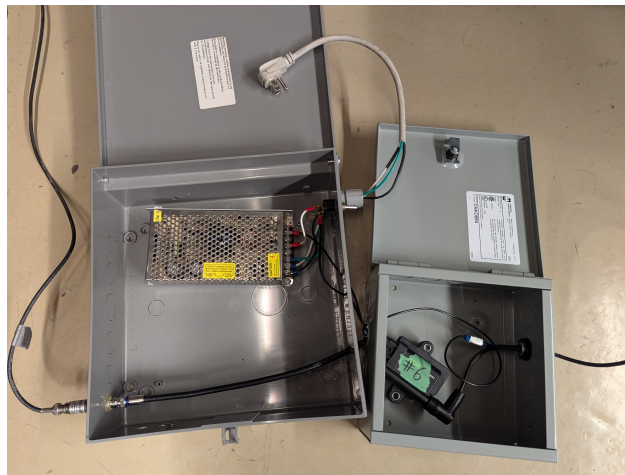


Figure 2.10: Spark initiation system. On the left is a power supply, while spark coil number 6 is on the right.

[Figure 2.11](#) shows the assembled electrodes, the sharper one being connected to the smart coil's output. The other electrode is grounded.



Figure 2.11: Assembled electrodes with Ultra-Torr cap and electrical connectors

2.2.9 Needle valve

To be able to run the thruster in the double choked configuration, an adjustable orifice upstream of the thruster is required. The WL14H-320P needle valve ([Figure 2.12](#)) was chosen for this.



Figure 2.12: WL14H-320P Needle valve

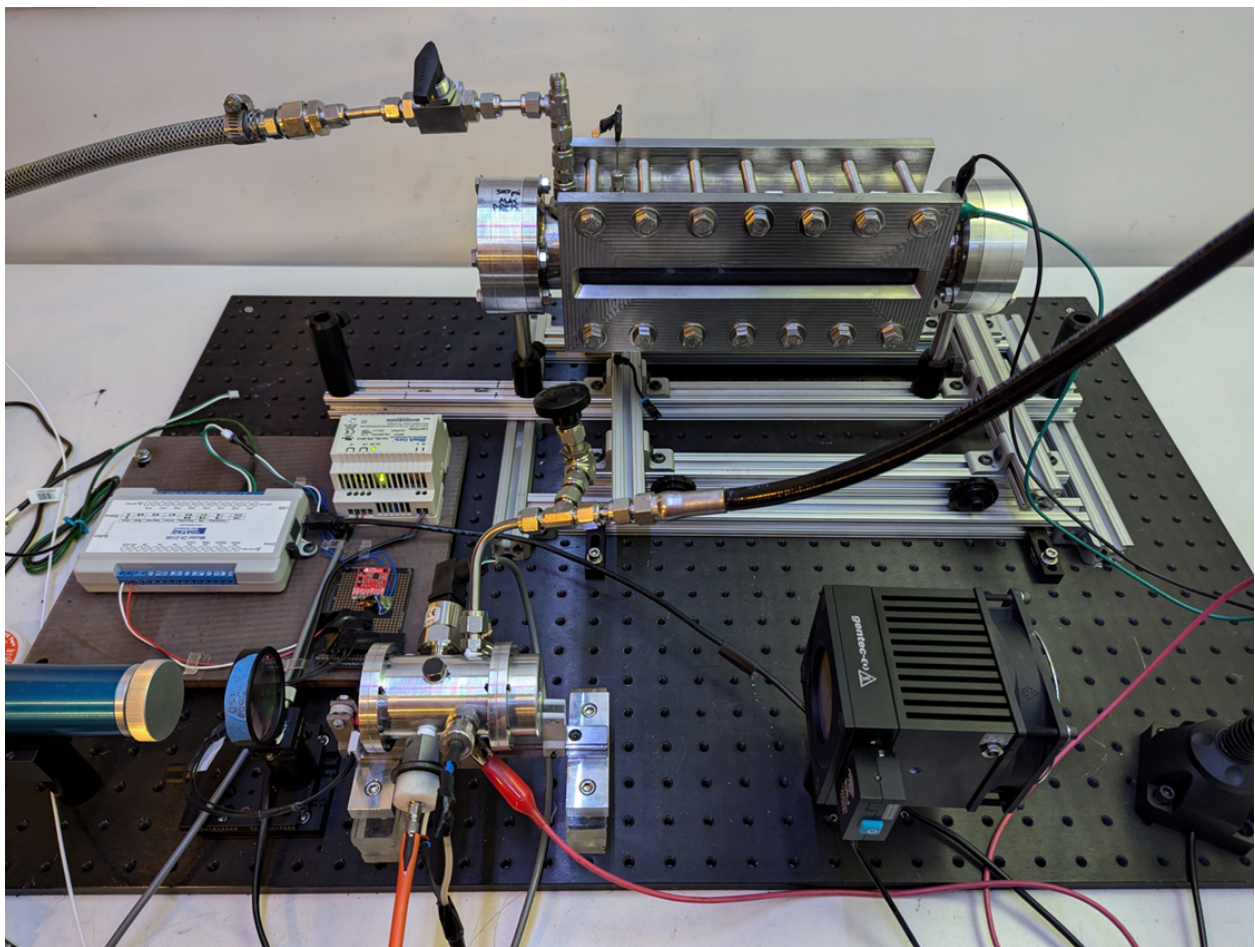


Figure 2.13: Size comparison between V1 (top, on extrusion rails) and V2 (bottom, mounted in front of laser collimator). V2 is in static configuration, without the extension cylinder.

In summary, the V1 and V2 test sections were presented, with an emphasis on V2's design. The various systems enabling LSP generation, control, and measurement with the V2 test section were also explained. The next chapter will present the results of the experiments conducted with these facilities.

Chapter 3

Experiments

The following chapter will explain the methodology and the results of the various experiments undertaken to develop, validate, and characterize the V2 thruster. Argon gas was used as the main propellant due to its low cost, safety, and ease of ionization.

3.1 Static laser-sustained plasma validation

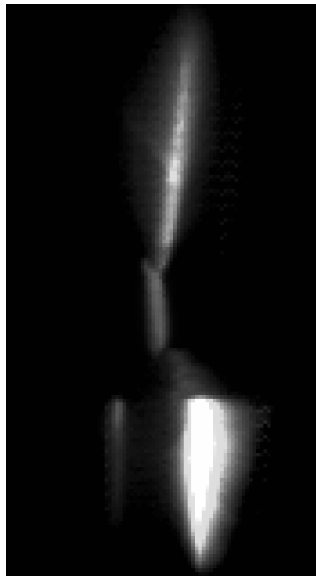
3.1.1 Spark initiation of plasma in version 1

For spark initiation to work reliably, the laser focus and the spark must both be aligned in space and in time. To resolve the spark spatially, the Photron SA5 camera was placed in front of the V1 test section instead of the laser, looking axially into the test section. This would be the point of view of the laser collimator during a Laser-Sustained Plasma (LSP) shot. [Figure 3.1a](#) shows a composite photo of the added opacities of five spark discharges (without laser). Each frame of the video has an opacity of $1/N$, with N being the total number of frames to add. This gave an average position of the spark, which is slightly to the left of the electrodes' centerline.

Using the thickness of the electrode (1.55 mm) as a reference, the spark gap's length is 0.8 mm and the average spark is 0.2 mm wide. Timing data was also recorded for the spark by the high-speed camera. To align the laser focus to the spark in time, the laser was reinstalled, and the camera was placed back to its normal position looking into the side of the test section (as in [Figure 3.1b](#)). The beam was then focused on one of the electrodes at low power. This caused the electrode to glow white-hot when the laser was on. The timings

3. EXPERIMENTS

3.1. STATIC LASER-SUSTAINED PLASMA VALIDATION



(a) Composite photo showing spark between two electrodes. The spark gap is approximately 0.8 mm.



(b) Front of V1 test section showing electrode position. This view is rotated 90° from [Figure 3.1a](#)

Figure 3.1: V1 spark alignment

presented in [Figure 3.2](#) were determined by this investigation.

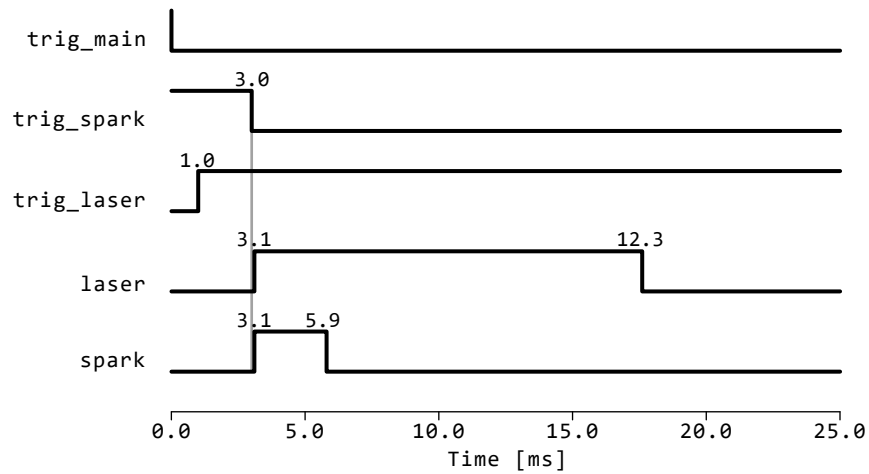


Figure 3.2: Signal timing diagram. The *trig* prefix denotes triggering signals. The component is active when the line is high. Timings in ms are also indicated on the figure.

With the position of the laser aligned to the spark and the timings synchronized, QCW LSP spark initiation in V1 was achieved with a 200 mm focal length lens at 100% power (3079 W) and a pressure of 20 bar, as seen in [Figure 3.3](#).

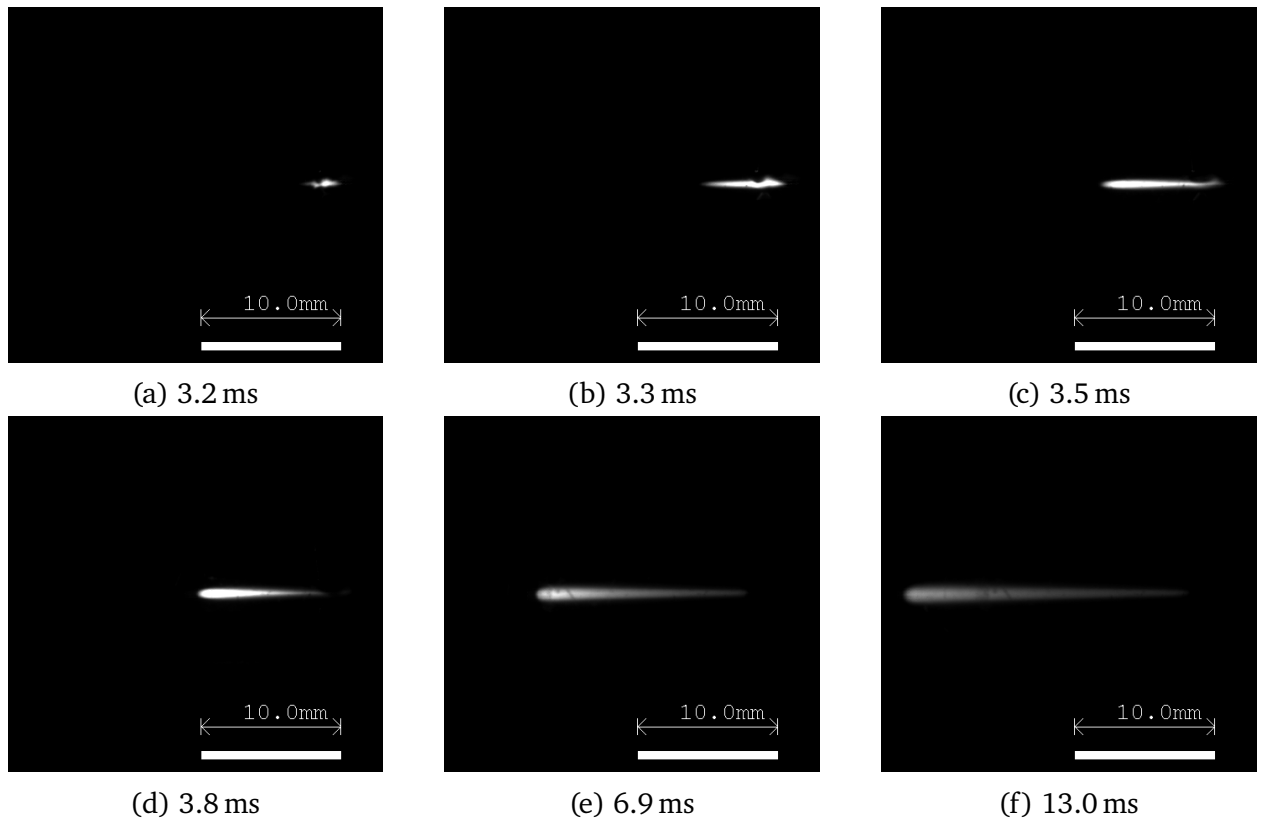


Figure 3.3: QCW LSP spark initiation in V1: 3079 W, 20 bar. LSP142_SPRK15.

The LSP is initiated at 3.2 ms, as soon as the spark is discharged. The front of the LSP moves towards the left (upstream, towards the laser), until the end of the QCW laser pulse at 13 ms. Once the laser ends its emission, the LSP dies down within two frames (0.2 ms).

3.1.2 Seeding argon with NO₂

As the plasma emits in the ultraviolet (UV) range, it is necessary to seed with a gas that absorbs UV but not the infrared (IR) laser. Khan *et al.* [17] shows that NO₂ and SO₂ are two candidates. NO₂ was first used as it was easy to produce in-house in significant quantities. The V1 system was set up with a vacuum pump connected to an outside air exhaust to safely vent the NO₂ gas. The pump was also used to bring the pressure in the test section down to a rough vacuum before introducing the gasses.

Three control QCW LSP shots were done in pure argon and their dynamic pressure trace from the PCB transducer was recorded. Next, 0.55 bar of NO₂, or 200 mL at Standard Temperature and Pressure (STP), was introduced into the chamber. V1 was then pressurized with argon to 20 bar. With the spark active, three LSPs were generated in the seeded atmo-

sphere. The dynamic pressure rise of the seeded argon was approximately double the one seen in pure argon. The next two LSP shots were conducted with 0.24 bar (85 ml at STP) of NO_2 and filled to 20.2 bar with argon. Again, higher pressure increases were observed, but slightly less than the 0.55 bar shots. The chamber was finally half evacuated to 10.17 bar and then filled back to 20.15 bar with argon. This would have brought the partial pressure of NO_2 to 0.12 bar. Two LSPs were initiated, with a higher pressure increase than pure argon, but less than the higher concentration NO_2 shots. Figure 3.4 presents the averages of these recorded pressure traces.

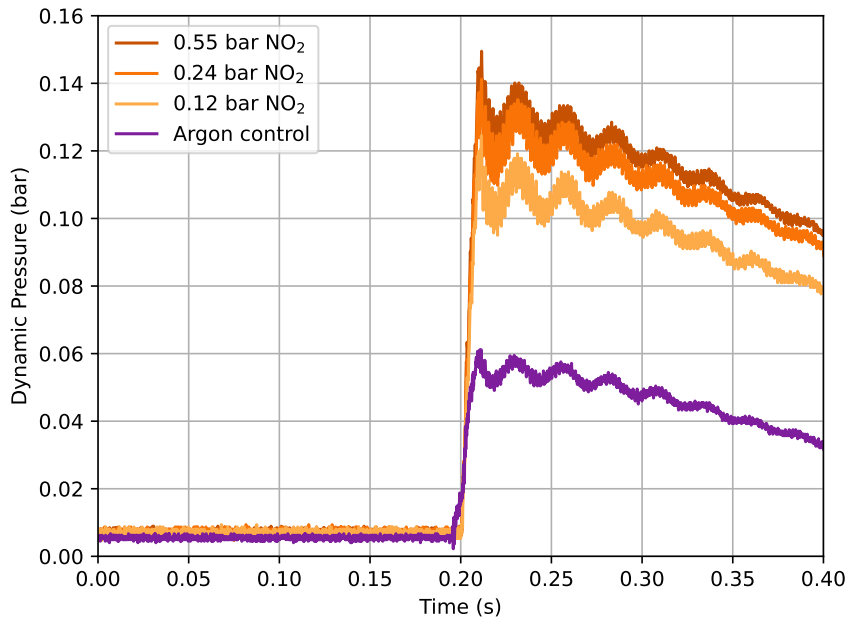


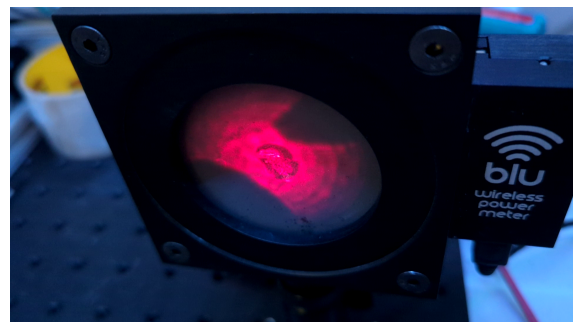
Figure 3.4: Average dynamic pressure rise of QCW LSP shots in a mixture of NO_2 and argon compared to that of pure argon QCW LSP. Initial pressure was 20.15 bar. Values given in the legend are the partial pressure of NO_2 seeding in the gas.

3.1.3 Spark initiation of plasma in version 2 and quasi-continuous wave laser-sustained plasma

For V2, the timings of the spark and laser pulse were kept the same as Figure 3.2. To align the laser focus spatially, the power meter was used as a screen to project the visible (red) alignment laser. By moving the V2 test section back and forth on the thrust stand rail, the Field Of View (FOV) of the shadows projected on the power meter can be modified, as seen in Figure 3.5. The laser focus can then be moved with the translation stages, so the brightest spot matches the center of the electrodes' shadow.



(a) V2 alignment, zoomed out



(b) V2 alignment, zoomed in

Figure 3.5: 2 FOVs of alignment laser light on power meter. The aberration at the center of the red light is due to laser damage to the window.

Once the laser focus was aligned, QCW LSP initiation was confirmed in V2 by the Photron SA5 looking into the front of the thruster at an angle, and the PCB transducer recording the pressure rise. [Figure 3.6](#), taken by the webcam, shows the brightness of a full power QCW LSP. Note the bright plasma emission to the left of the image on the laser safety curtain.

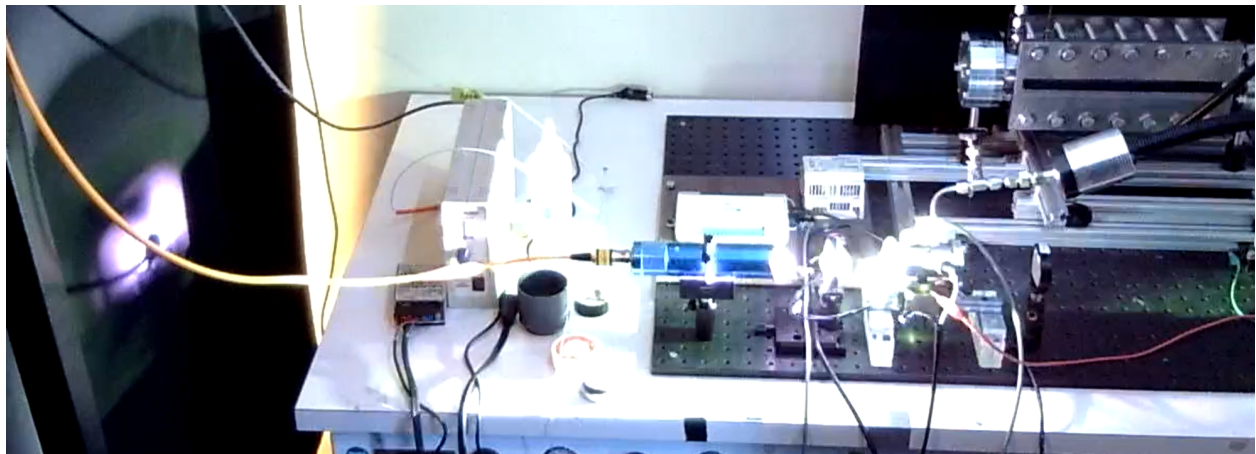


Figure 3.6: 100% power (3079 W) QCW LSP shot

3.1.4 Optical experiments: going from quasi-continuous wave to continuous wave laser-sustained plasma

Due to the low continuous laser power in this experiment compared to others in the literature, increasing the laser flux with a small focus is critical. The real amount of power in the pulsed shots was measured to get a conversion between the laser power setting (in %) to power (W), which does not scale directly at lower powers. 10 shots each at 10 % and 12 % were measured with the power meter, with statistics compiled by the power meter software

(Table 3.1). The average power was calculated by dividing the average pulse energy (J) by the pulse duration (50 ms).

Table 3.1: Statistics from the power meter after 10 times 50 ms laser shots at 10% and 12% power

Value [Unit]	10 × 50 ms shots at 10% power	10 × 50 ms shots at 12% power
Average energy value [J]	9.985	12.89
Maximum energy value [J]	10.2	13.3
Minimum energy value [J]	9.63	12.0
RMS Stability [%]	1.690	2.811
PTP Stability [%]	5.599	10.31
Std deviation [J]	0.169	0.362
Average power [W]	200	258

Extrapolating from these results, 300 W is achieved at 13.5 %.

Pulsed shots at lower power levels with a 200 mm focal length lens (Thorlabs LA1979-C) revealed a difficulty to initiate QCW LSP below 30% power, around 1 kW. This presented a problem, as the maximum continuous wave (CW) power of the laser is significantly lower at 342 W (see [Appendix A](#)). A test campaign was initiated to determine if LSP initiation in the V1 thruster was possible under this maximum CW power level. [Equation 3.1](#) [18] can be used to estimate the beam diameter at the focus:

$$\text{Spot diameter (mm)} = \frac{4 \times \text{Focal length (mm)} \times \text{Wavelength (mm)} \times M^2}{\pi \times \text{Beam diameter at lens (mm)}} \quad (3.1)$$

The beam propagation factor M^2 is a scale to measure beam quality. A diffraction-limited Gaussian beam has the minimum M^2 of 1 (Hecht [19]). The YLR-300/3000 laser has a Beam Parameter Product (BPP) of 2 mm mrad, as found in [Appendix A](#). An M^2 of 5.87 is calculated using [Equation 3.2](#) [20].

$$M^2 = \frac{\pi}{\lambda} \text{BPP} \quad (3.2)$$

From [Equation 3.1](#), lowering the focal length of the lens lowers the spot diameter, increasing laser flux. The *Thorlabs Lens Tutorial* [21] also mentions that a dual-lens system can lower the beam diameter at the focus.

A single plano-convex lens with a 125 mm focal length (Thorlabs LA1384-C) was then used,

as it was the lowest focal length lens that could focus at V1's initiation plug position. A 100 mm focal length lens was available, but the position of the focus was before the electrodes, even when pressing the lens against V1's front window. [Figure 3.7](#) shows a record of LSP initiation attempts at various power settings and lens axial positions with the 125 mm focal length lens. An argon pressure of 20 bar was used for these shots. At power lev-

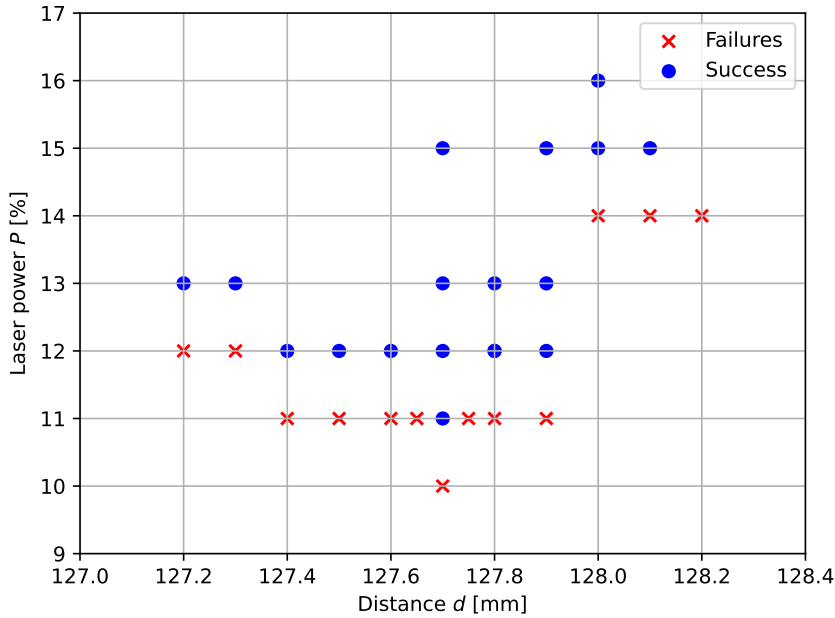


Figure 3.7: LSP threshold graph for V1 with 125 mm focal length lens

els lower than 15%, initiation was unreliable and could take up to 20 attempts to get one initiation. For example, initiation at 11 % was successful once, but it was not possible to repeat this. An even smaller diameter focus was necessary to increase initiation reliability by increasing laser flux at the focus, and a dual-lens system was designed.

For a dual-lens system, the spot diameter must be calculated numerically. Ray tracing software, such as WinLens3D Basic, calculate the geometry of paraxial ¹ rays and show the path of these rays at the focus. WinLens3D was chosen to simulate the spot size of both the single- and dual-lens systems, as it is free and powerful enough for this application. The modelled lenses are seen in [Figure 3.8](#).

With a dual-lens system, the longest focal length lens should be placed first, contrary to what is shown. This would lead to a tighter focus, as the diameter of the beam entering the second lens is maximized. In this case, the 500 mm focal length lens was placed after the

¹Rays having small angles and distances to the optical axis

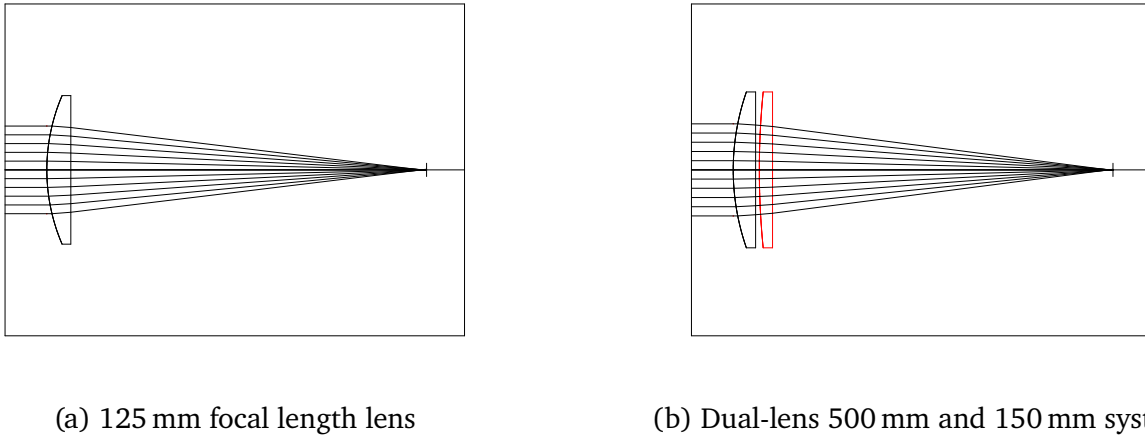


Figure 3.8: Model of the lenses showing paraxial rays and focus

150 mm lens as it was impossible to mount before with the available mounting hardware. WinLens3D showed that the difference in spot size was minimal. A practical consideration for the experiments is that the LSP will be formed upstream of the laser focus when there is no gas flow because the plasma's radiation pre-heats the gas. Therefore, the focus needs to be slightly after the initiation system.

[Figure 3.9](#) presents the spot diagrams that were then produced with WinLens3D. Note the difference in scales and spacing used throughout. From these three spot diagrams, the average laser flux at 342 W was calculated (see [Table 3.2](#)). It is assumed that the laser energy is evenly distributed in a circle as wide as the farthest ray from the center, which gives a lower bound for the laser flux. The LSP experiments were continued with this

Table 3.2: Simulated focal length and spot diameter of various lens assemblies in WinLens3D. The average laser flux is calculated for 342 W of incident power

Lens	Nominal focal length (mm)	Focal length at 1070 nm (mm)	Beam diameter at focus (mm)	Average laser flux at 342 W (MW/cm ²)
Single	125	122	0.20	1.09
Single	100	93	0.15	1.94
Dual	500, 150	110	0.08	6.80

dual-lens system (500 mm and 150 mm focal lengths), as it offers a 6.25 times increase of the laser flux compared to the single 125 mm focal length lens. To increase the laser flux even more, an aspheric lens of comparable focal length could be used, though it costs 10 times as much as a single plano-convex lens. [Figure 3.10](#) presents a record of LSP initiation

3. EXPERIMENTS

3.1. STATIC LASER-SUSTAINED PLASMA VALIDATION

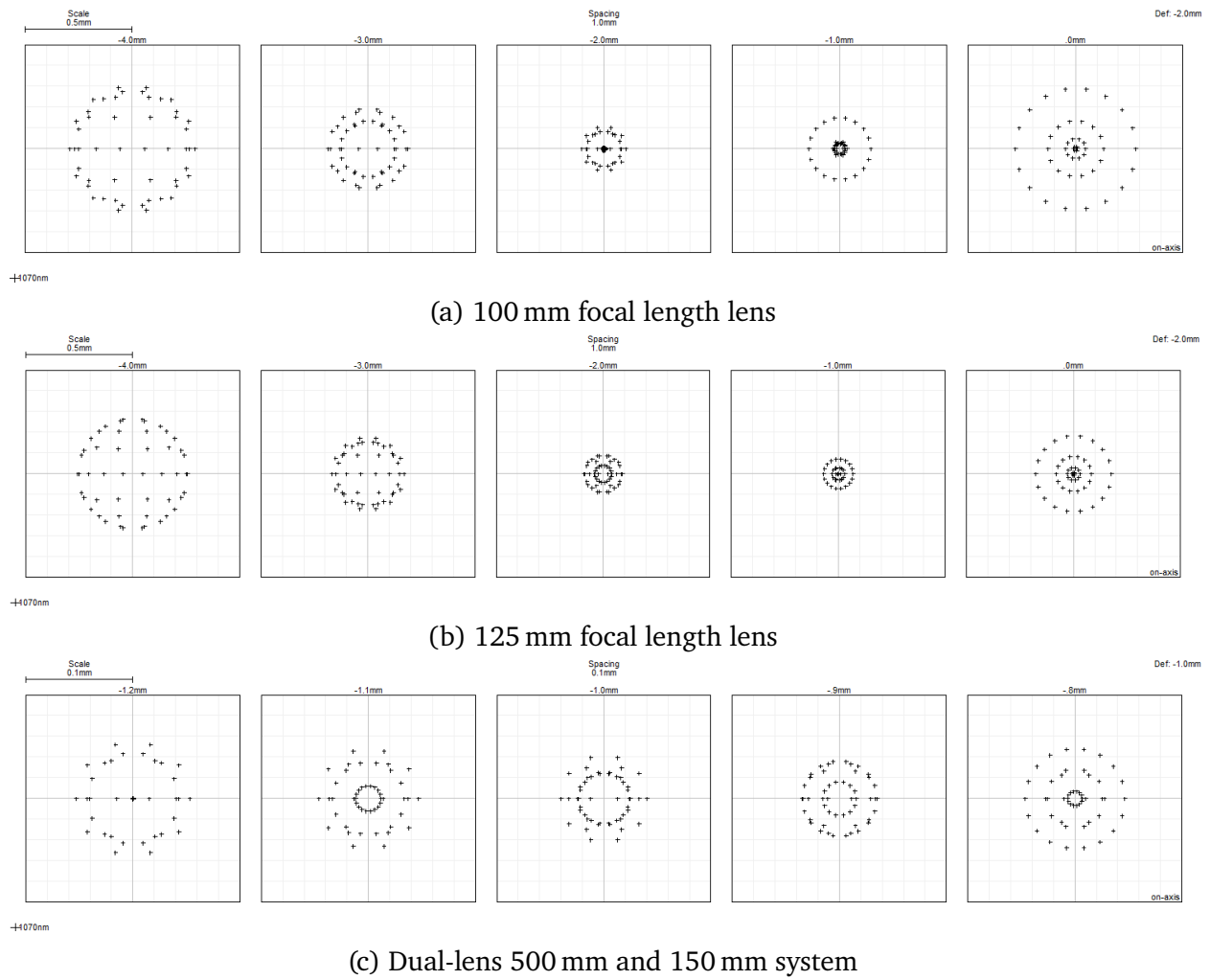


Figure 3.9: Spot diagrams of the three lens systems studied

attempts at various power settings and lens axial positions with this dual-lens system in V1. The completion of these tests validated the dual-lens design, showing that LSPs in the CW power regime of the laser could be generated. The first LSPs in V2 were therefore done using the dual-lens system. A similar graph to [Figure 3.10](#) was then created with V2 to find the lens position where the minimum laser power could reliably initiate QCW LSP. [Figure 3.11](#) presents these initiation attempts.

3.1.5 Version 2 continuous wave laser-sustained plasma

A 100 % power (342 W) CW shot was then attempted with static argon at 20.00 bar.

The webcam footage ([Figure 3.12](#)) will be examined first. The laser was first turned on. A flash marked the spark initiation and lifetime of the LSP. This flash lasted only a few frames.

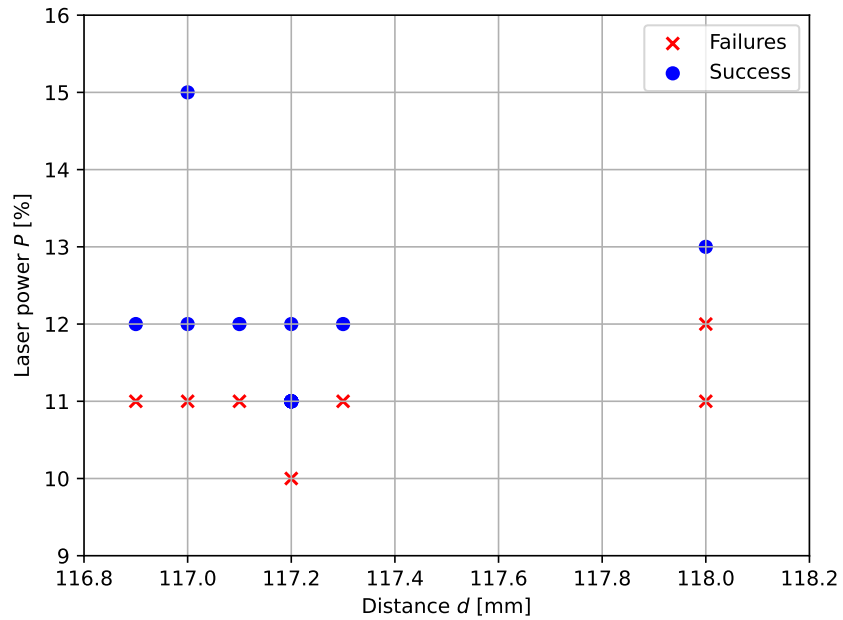


Figure 3.10: LSP threshold graph for V1 with dual-lens system

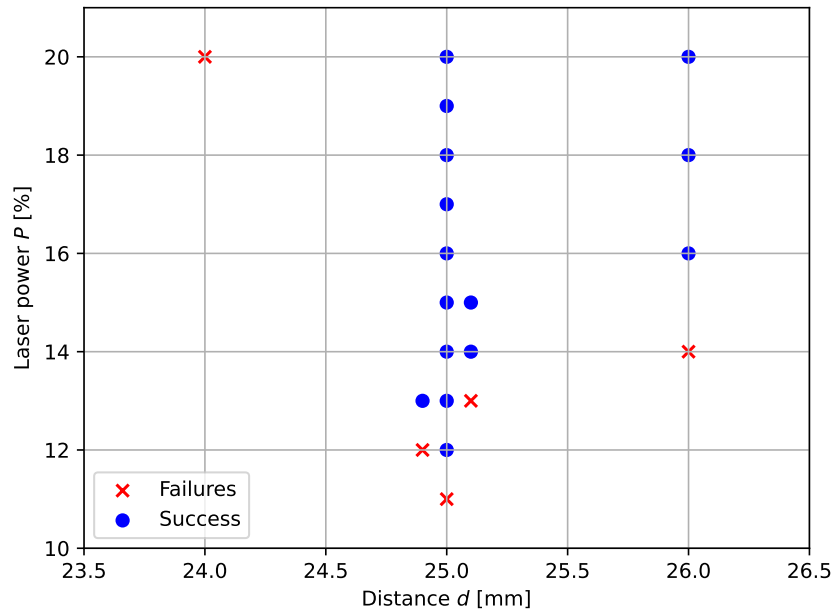


Figure 3.11: LSP threshold graph for V2 with dual-lens system

Notice the higher brightness in [Figure 3.12c](#), reflected off various surfaces like the white box (PCB signal conditioner) on the left of the collimator. The laser was kept running for

3. EXPERIMENTS

3.1. STATIC LASER-SUSTAINED PLASMA VALIDATION

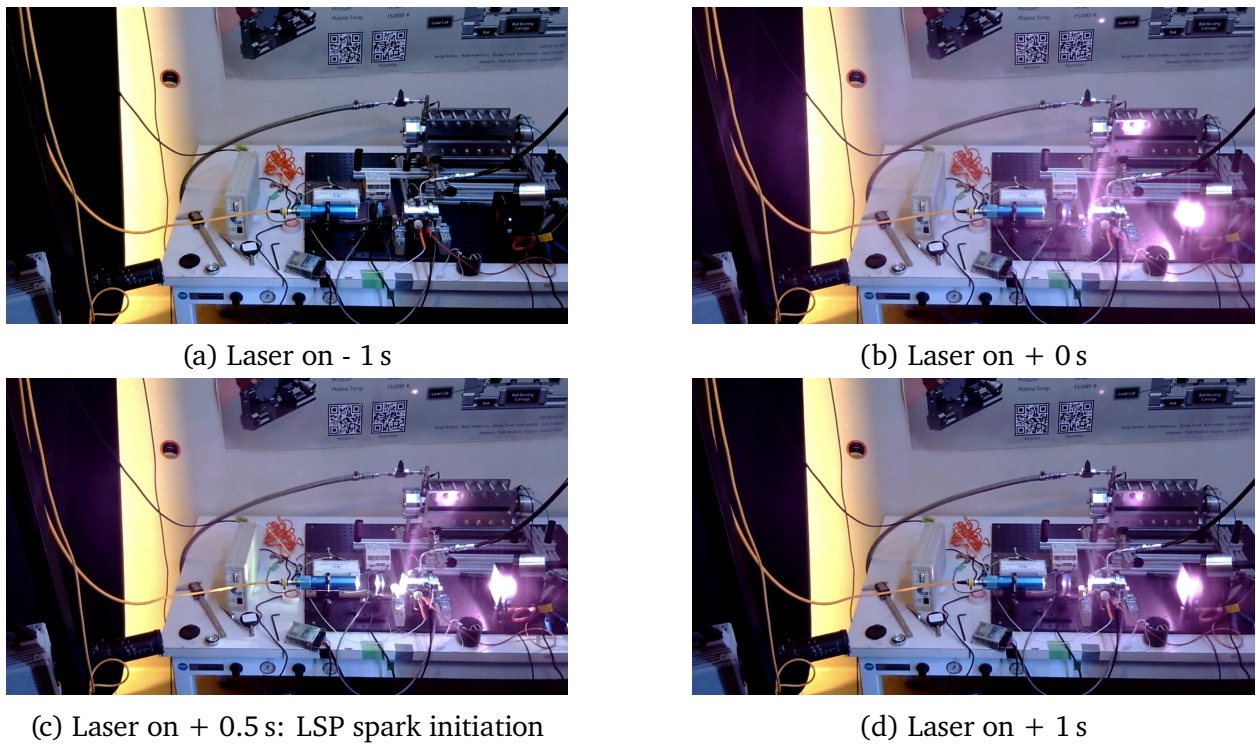


Figure 3.12: First CW LSP captured by the webcam: 342 W, 20.00 bar. LSP385_V2_CW1.

about a second before it was turned off.

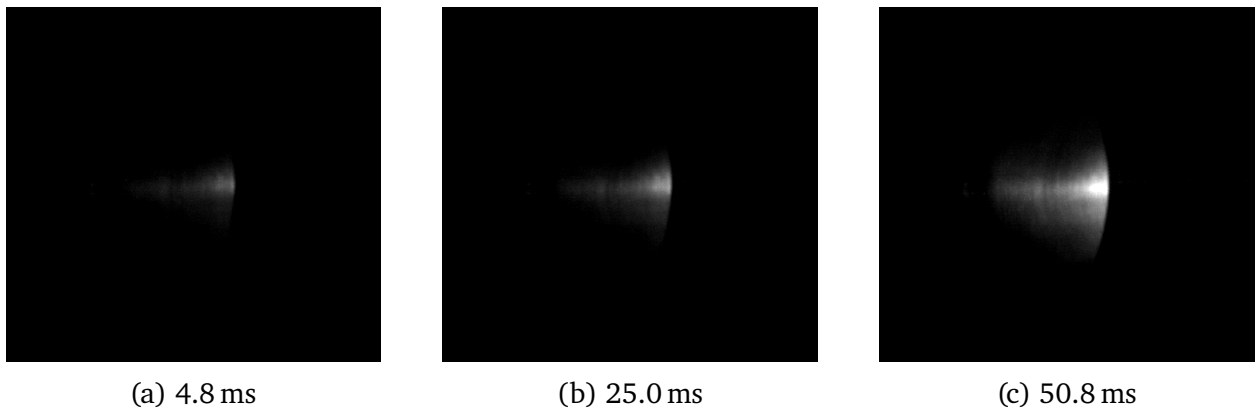


Figure 3.13: First CW LSP captured by the Photron high-speed camera: 342 W, 20.00 bar. LSP385_V2_CW1.

Observation of the high-speed camera footage (Figure 3.13), recorded at 10,000 frames per second, showed the CW LSP starting at frame 32 (3.2 ms) and ending at frame 883 (88.3 ms), lasting 85.1 ms. This represents a 1.7 times longer lifetime than the maximum QCW pulse length of 50.0 ms at this power. The brightness of the plasma increased regularly after initiation, to reach its maximum intensity around 50 ms. The maximum brightness

was constant for 10 ms. A flickering of the LSP was seen at 70.0 ms, before it died down and was completely extinguished after 88.3 ms. This was the first CW LSP generated in the lab.

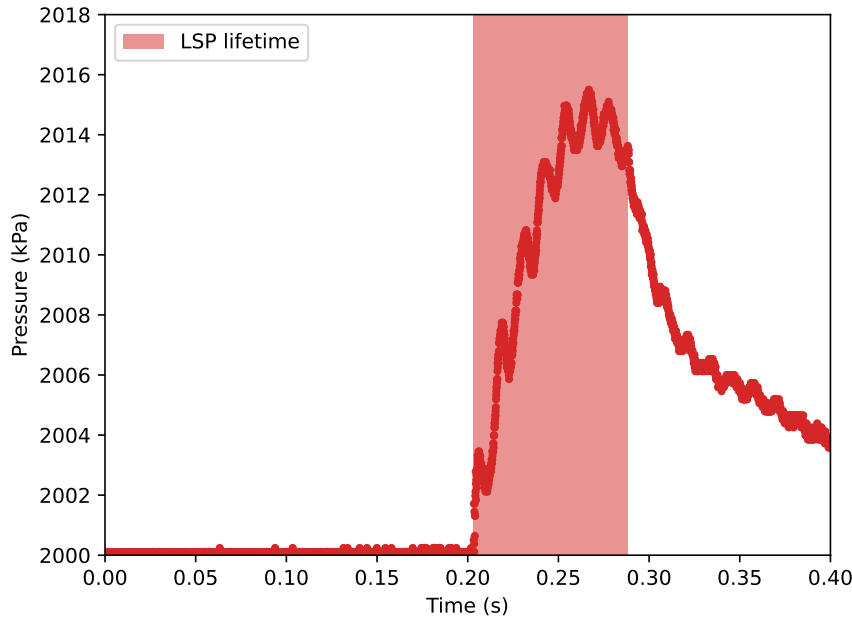


Figure 3.14: Dynamic pressure rise from CW LSP measured with PCB transducer

[Figure 3.14](#) shows the pressure rise recorded by the PCB transducer connected to the oscilloscope. Minimal damage to the window was noticed after this test.

3.2 Version 2 cold flow thruster characterization

3.2.1 Cold flow thrust tests

Cold flow tests (laser off) were completed with V2 to give a baseline measurement of thrust before eventual hot fire tests (laser on), and to validate the functioning of all data acquisition systems.

For thrust tests, pressure and thrust were recorded. [Figure 3.15](#) shows a typical thrust and pressure curve for a chamber pressure of 20 bar. Note that the thrust measurement does not return to the same value it was at initially.

Next, cold flow thrust tests were completed at chamber pressures from 5 bar to 35 bar. A linear curve fit of the experimental results is presented in [Figure 3.16](#).

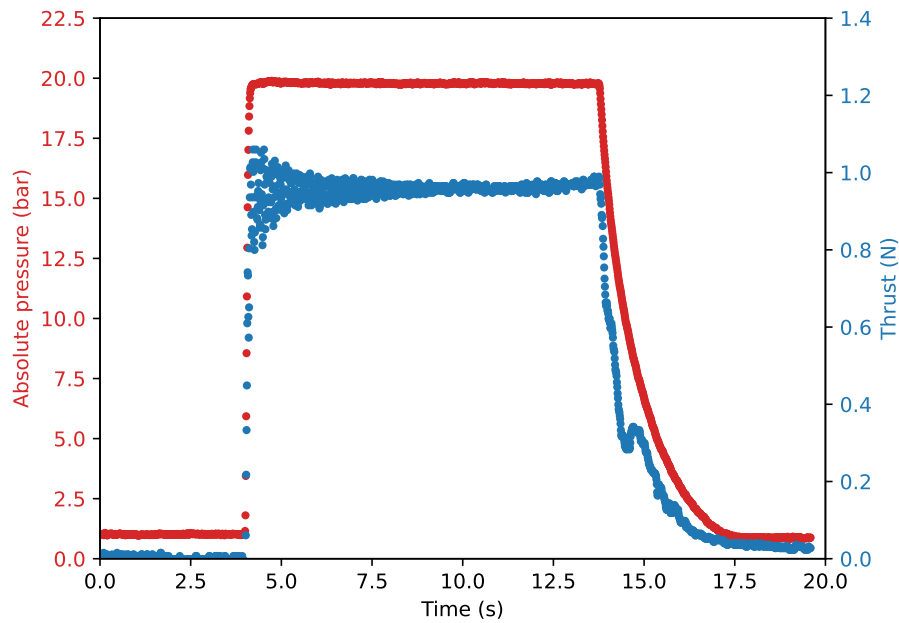


Figure 3.15: Typical cold flow pressure and thrust curves for 20 bar chamber pressure

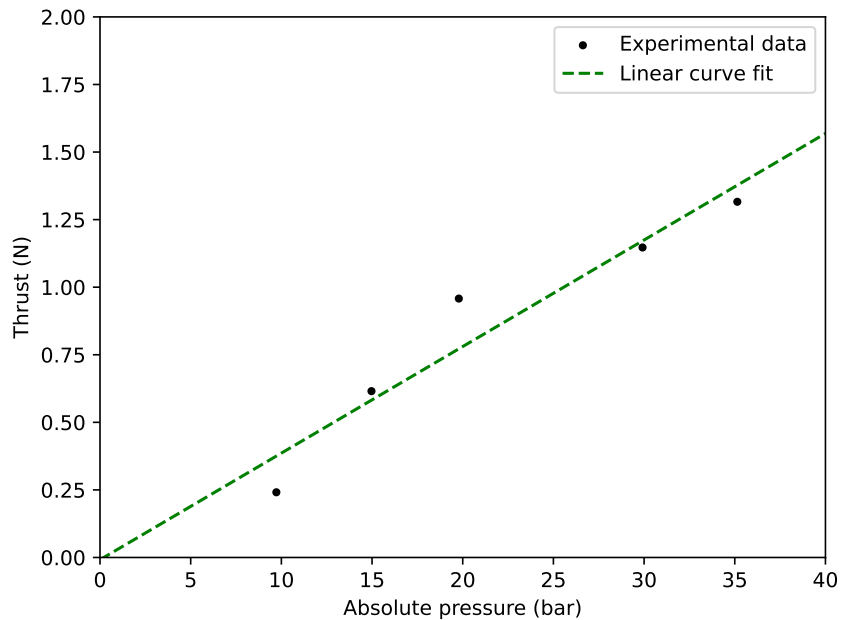


Figure 3.16: Absolute pressure versus thrust and curve fit of pressure-thrust relation

The empirical relation of pressure versus thrust is given by:

$$\text{Thrust (N)} = 0.0394 * \text{Pressure (bar)} + 0.0318 \quad (3.3)$$

Repeatability of the thrust measurements was then examined with the Honeywell FSG005WNPB 0 N to 5 N load cell and a 200 g preload, with an argon inlet pressure of 20 bar. The raw voltage of the load cell was recorded, as the hysteresis was the point of interest and not the thrust. Significant hysteresis of the thrust stand is seen in [Figure 3.17](#). The final thrust was

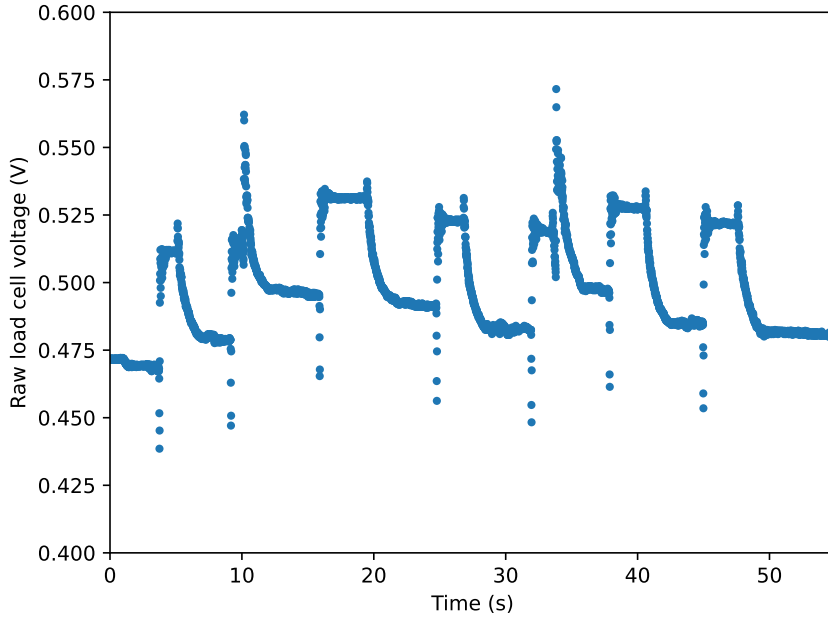


Figure 3.17: Multiple cold flow thrust tests in succession

sometimes higher than the initial thrust, sometimes lower. The discontinuities at 10 s and 35 s were due to the accidental shutoff of the gas supply.

3.2.2 Thruster nozzle effective sonic area A^*

To determine the argon mass flow rate \dot{m} of the thruster, sonic isentropic flow at the nozzle throat was assumed. The following equation can then be used:

$$\dot{m} = \frac{A^* p_0}{\sqrt{T}} \sqrt{\frac{\gamma}{R}} \left(\frac{\gamma + 1}{2} \right)^{\frac{-(\gamma+1)}{2(\gamma-1)}} \quad (3.4)$$

Where A^* , the nozzle effective sonic area, is an unknown, p_0 is the stagnation pressure, T is temperature, γ is the specific heat ratio, and R is the specific gas constant.

To characterize the effective sonic area, A^* , of the thruster nozzle, a choked orifice blow-down test was done based upon the solution found in Saad [22]. V2 in flowing configuration

was pressurized to 20 bar of argon. The argon flow was then closed. The pressure curve was recorded by the Omega transducer.

The internal volume of the V2 thruster in flowing configuration was determined by weighing it before and after it was filled with isopropyl alcohol. Using a density of 785 kg/m^3 , the volume was found to be $9.68 \times 10^{-6} \text{ m}^3$, or 9.68 ml.

The following expression for the pressure-time history of a blow down choked orifice flow [22] was then implemented in Python. As the timescale is short (less than 10 seconds), the process is considered adiabatic, and the isentropic case is used:

$$t = \frac{-2V \left[\left(\frac{p(t)}{p_i} \right)^{(1-\gamma)/2\gamma} - 1 \right]}{(1-\gamma)R\sqrt{T}A \sqrt{\frac{\gamma}{R} \left(\frac{2}{\gamma+1} \right)^{(\gamma+1)/(\gamma-1)}}} \quad (3.5)$$

Where t is time, $p(t)$ is the absolute pressure in the system at time t , p_i is the initial absolute pressure in the system, V is the volume of the V2 thruster and tubing after the valve, T is temperature, and A is the area of the nozzle's throat. With this equation, the absolute pressure in bar was plotted versus time in seconds for different values of A , with a specific heat ratio γ of 1.67, a temperature of 300 K, and an R value of 208.13 J/(kg K) (see Figure 3.18). An experimental pressure curve was also overlaid, similar to Figure 3.15, but cut to only show the decrease in pressure right after the gas feed valve is closed. The time at which this valve is closed is defined as $t = 0$.

The best match was found to be an area of $3.46 \times 10^{-8} \text{ m}^2$, giving a nozzle diameter of 0.21 mm.

3.2.3 Needle valve effective sonic area A^*

The WL14H-320P needle valve (see Figure 2.12) was calibrated to relate its rotation increments to its flow rate. This was undertaken by connecting the valve's input to a gas supply, while the valve's output was connected to a bubble flow meter constructed for this experiment (Figure 3.19). The tube used for the bubble flow meter had an internal diameter of 5.80 cm and a length of 63.78 cm, resulting in an internal volume of 1.68 L. The bubble flow meter and experiment methodology were presented in Barigou and Davidson [23].

A uniform bubble created at the base of the tube rises upwards towards the top of the tube as it is displaced by the pressurizing gas. This end of the tube was open to the atmosphere.

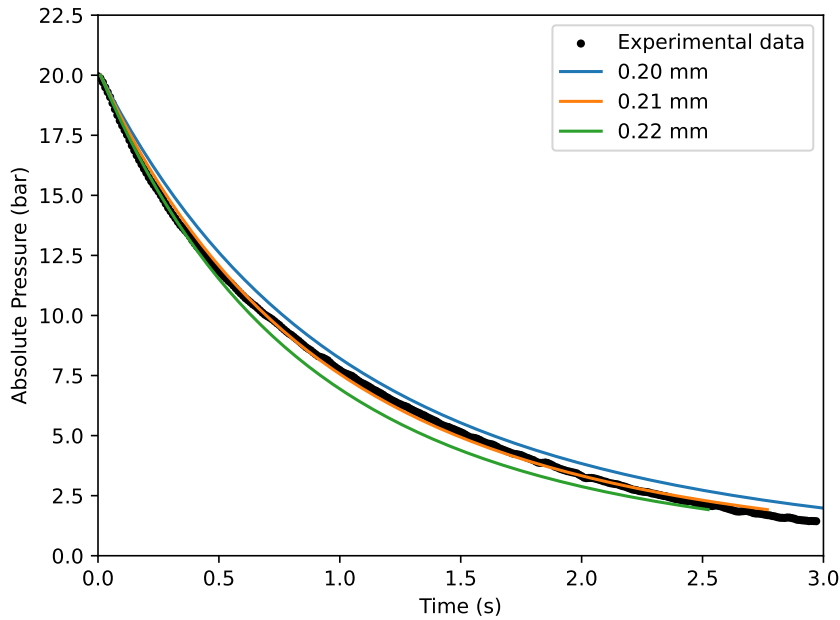


Figure 3.18: Saad blowdown model and experimental data

A stopwatch was started when the bubble passed the base of the green tape line and stopped once the bubble passed the base of the red tape line. These stopwatch measurements were repeated three times and averaged. This enabled precise measurement of the volumetric flow rate.

First, the valve was calibrated with air at 3.45 bar and 6.89 bar. The valve was then calibrated with 20 bar and 50 bar of argon. The volumetric flow rate was measured in both cases for increments of 0.5 rotations to 2.0 rotations. [Equation 3.4](#) can again be used to calculate the critical area A^* of the valve, which is presented in [Table 3.3](#).

Table 3.3: Calculated opening area and calculated diameter for needle valve at different rotation increments (upstream pressure = 5000 kPa and outlet pressure = 100 kPa)

Increment	Volume Flow (L/s)	Mass Flow (g/s)	A^* (mm ²)	Diameter from A^* (mm)
0.5	0.25	0.410	0.028	0.188
1.0	0.37	0.607	0.041	0.229
1.1	0.51	0.836	0.057	0.269
1.2	0.67	1.099	0.075	0.308
1.3	0.97	1.591	0.108	0.371
1.4	1.24	2.033	0.138	0.419

For a mass flow rate of 0.641 g/s, a temperature of 293 K, a P_0 of 5000 kPa, a γ of 1.67, and

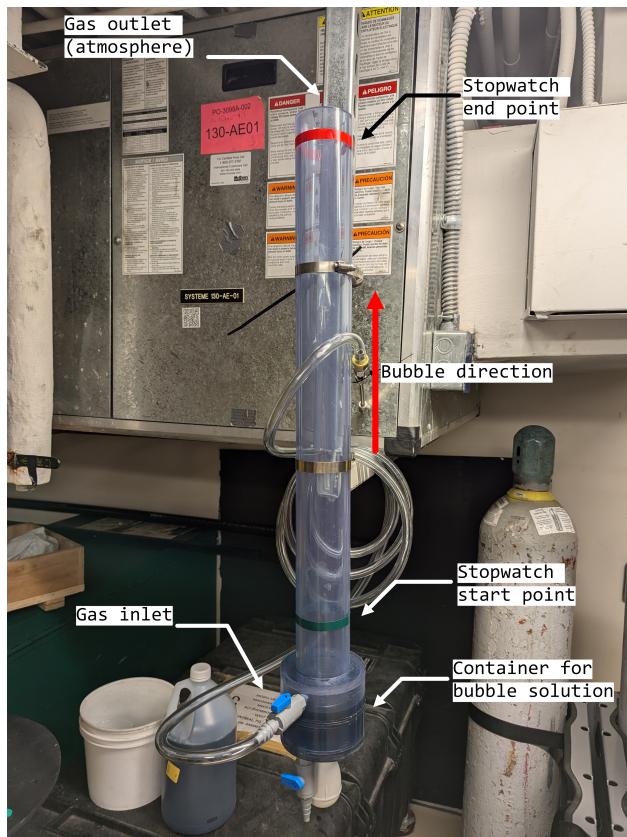


Figure 3.19: Bubble flow meter setup

an R of $208.13 \text{ J}/(\text{kg K})$, an A^* of 0.0436 mm^2 and an opening diameter of 0.236 mm are found. This means the needle valve must be open between an increment of 1 and 1.1.

3.2.4 Summary of results

Table 3.4 presents a summary of the results determined from cold flow thruster characterization.

Table 3.4: Summary of the studied V2 thruster characteristics

Characteristic	Value and unit
Needle valve A^* with predicted experiment conditions	$4.36 \times 10^{-8} \text{ m}^2$
Nozzle A^*	$3.46 \times 10^{-8} \text{ m}^2$
Internal volume of thruster in flowing configuration	$9.68 \times 10^{-6} \text{ m}^3$
Average cold flow thrust at 20 bar	0.96 N

3.3 Initial quasi-continuous wave laser-sustained plasma thrust tests (hot fire)

With V2 CW LSP achieved, and the cold flow thrust tests completed, initial QCW LSP thrust tests were attempted. The needle valve was not installed as it was not yet procured.

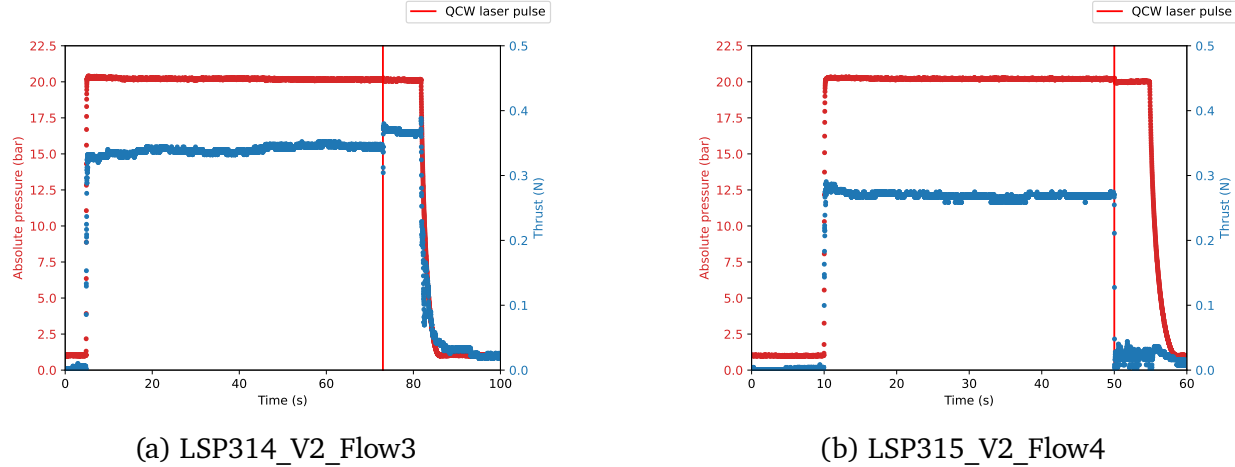


Figure 3.20: Two QCW thrust tests

The thrust stand was unfortunately not calibrated before these tests. Thrust values should be closer to 1 N, according to previous cold flow data. Nonetheless, the QCW pulse changes the thrust in both cases, but in opposing directions. No definitive increase in thrust could be determined with the current V2 setup when the laser was on.

The following webcam frame ([Figure 3.21](#)) was taken from the LSP315_V2_Flow4 3079 W QCW shot, with the electrodes unplugged so no LSP could be initiated. A plasma plume still left the nozzle and the noise of the flow changed once the laser was fired, indicating possible nozzle ablation.

Further flowing tests confirmed that LSP could be initiated by a spark in flowing argon. The following frame ([Figure 3.22](#)) from the Photron SA5 shows LSP light emission in 20.0 bar of flowing argon.

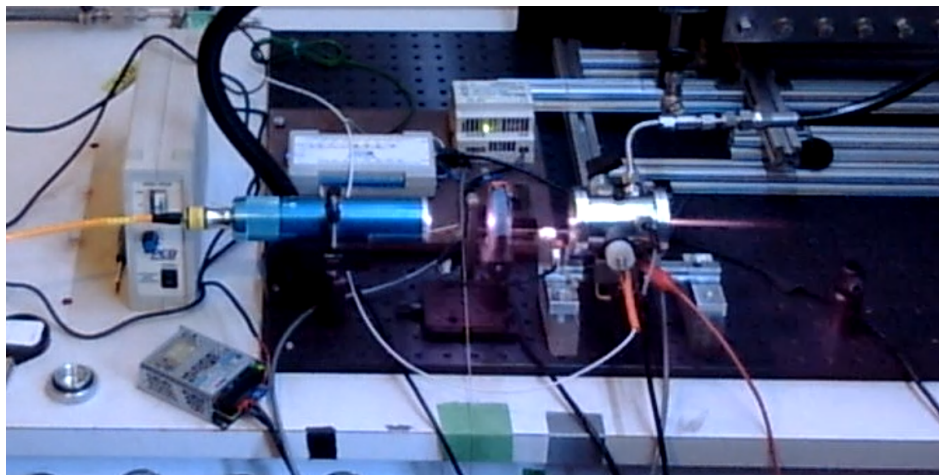


Figure 3.21: Nozzle ablation during flowing test. LSP315_V2_Flow4.

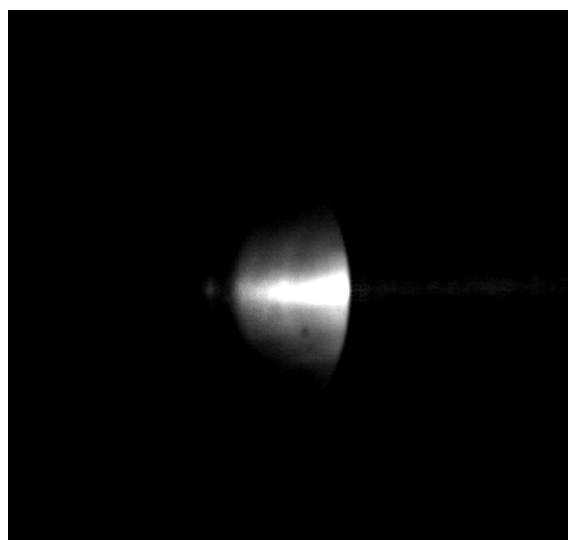


Figure 3.22: V2 Flowing QCW LSP. LSP321_V2_Flow10.

Chapter 4

Zero-dimensional laser-sustained plasma model

To predict experimental data, namely the pressure increase of the gas that should be expected when laser energy is input, the heat capacity of argon and hydrogen was modelled. A zero-dimensional (0D) heat transfer model was then written in Python to compare to experimental data. Argon and hydrogen were used to validate initial equilibrium calculations, while the 0D model was solely implemented using argon. Argon was the main gas used in experiments, as it was economical and easy to ionize. Hydrogen is projected to be used in a full-scale LTP engine for its increased I_{sp} due to its lower molecular weight.

4.1 Equilibrium calculations

The following seventh order polynomials and their coefficients (a_1 to a_7 , b_1 , and b_2), from McBride *et al.* [24], were implemented in Python. Species of interest were H, H₂, Ar, Ar⁺, and electrons e⁻. Plasma temperatures studied allowed us to treat the argon as singly ionized, and the hydrogen as dissociated. The heat capacity at constant pressure, as well as the temperature (T) dependent part of enthalpy and entropy of each species are given by c_p^0 , h^0 , and s^0 , respectively. \bar{R} is the universal gas constant.

$$c_p^0(T)/\bar{R} = a_1 T^{-2} + a_2 T^{-1} + a_3 + a_4 T + a_5 T^2 + a_6 T^3 + a_7 T^4 \quad (4.1)$$

$$h^0(T)/\bar{R}T = -a_1 T^{-2} + a_2 \ln(T)/T + a_3 + a_4 T/2 + a_5 T^2/3 + a_6 T^3/4 + a_7 T^4/5 + b_1/T \quad (4.2)$$

$$s^0(T)/\bar{R} = -a_1 T^{-2}/2 - a_2 T^{-1} + a_3 \ln(T) + a_4 T + a_5 T^2/2 + a_6 T^3/3 + a_7 T^4/4 + b_2 \quad (4.3)$$

Next, the functions for entropy \bar{s}_i of each species i and Gibbs energy \bar{g}_i , both per kmol, were implemented. These values depend on temperature T and partial pressure p_i . y_i is the molar fraction of the species, p_{ref} is the reference pressure, equal to 1 bar, and p is the total pressure of the gas.

$$\bar{s}_i(T, p_i) = \bar{s}_i^0(T) - \bar{R} \ln \frac{y_i p}{p_{\text{ref}}} \quad (4.4)$$

$$\bar{g}_i = \bar{h}_i - T \bar{s}_i \quad (4.5)$$

Considering the number of moles n_i , expressions of the Gibbs energy of the two mixtures G_{mixture} were found:

Starting with 1 kmol argon,

$$G_{\text{mixture, Ar}}(T, p) = n_{\text{Ar}} \bar{g}_{\text{Ar}}(T, p_{\text{Ar}}) + n_{\text{Ar+}} \bar{g}_{\text{Ar+}}(T, p_{\text{Ar+}}) + n_{\text{e}} \bar{g}_{\text{e}}(T, p_{\text{e}}) \quad (4.6)$$

Starting with 1 kmol hydrogen,

$$G_{\text{mixture, H}_2}(T, p) = n_{\text{H}} \bar{g}_{\text{H}}(T, p_{\text{H}}) + n_{\text{H}_2} \bar{g}_{\text{H}_2}(T, p_{\text{H}_2}) \quad (4.7)$$

[Figure 4.1](#) plots the Gibbs energy of the hydrogen mixture as a function of its degree of dissociation x , for different total pressures p .

A similar dissociation graph can be found with argon, but with three species. The Gibbs energy was then minimized to determine the molar fractions y_i at which the mixture reaches equilibrium. From this, the enthalpy H of the mixture was found. The c_p of the mixture was then calculated from the enthalpy with:

$$c_p = \left. \frac{\partial h}{\partial T} \right|_{p=\text{const.}} \quad (4.8)$$

For argon, these calculated c_p values were validated against values from CEA [25] in [Fig-](#)

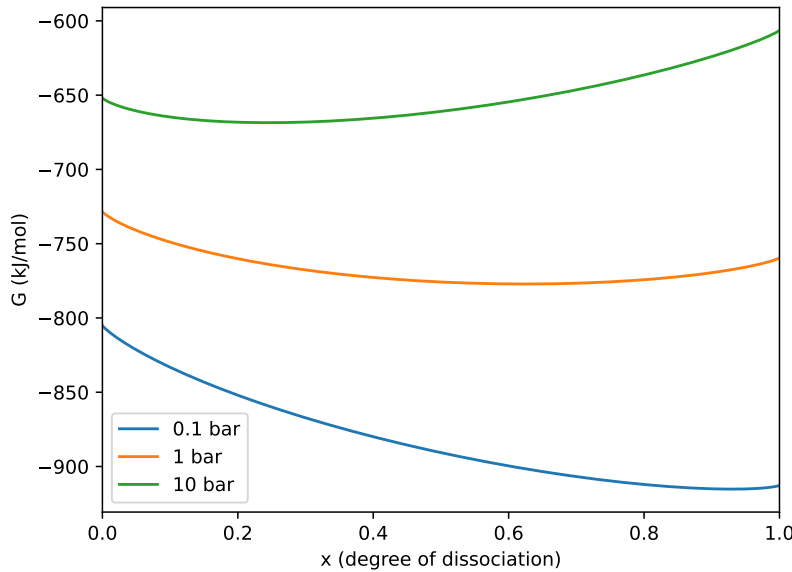


Figure 4.1: Gibbs free energy (G) plotted against the degree of dissociation (x) of hydrogen under three different pressures

ure 4.2.

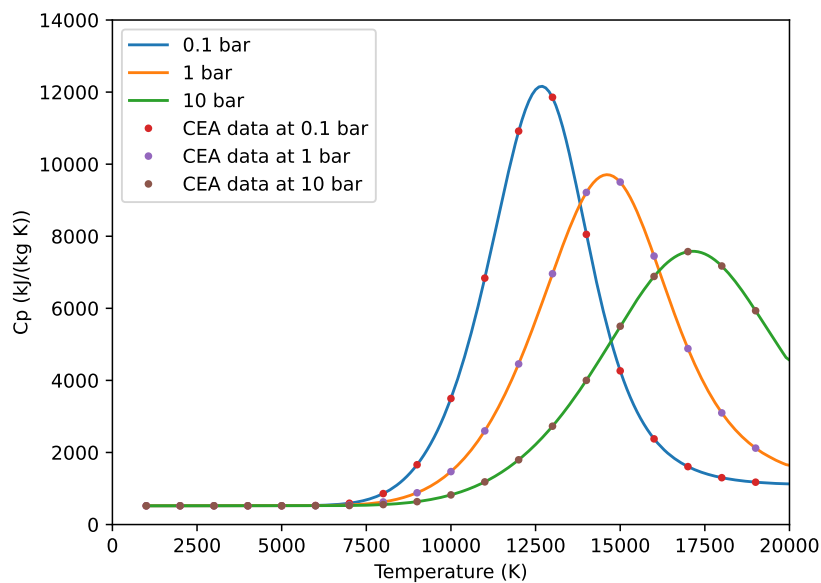


Figure 4.2: Comparing calculated c_p values of argon to those from CEA

The properties of the argon plasma will be used as the basis of the 0D LSP model.

4.2 Bremsstrahlung energy loss

The main source of radiation found in LSP is Bremsstrahlung, or braking radiation. When an electron passes close to a heavier ion, it is deflected by the ion's electric field. This collision releases a photon [26]. The total radiated power density P_{br}/V of the collisions can be estimated with the formulas presented in [Table 4.1](#).

[Table 4.1](#): Comparison of Bremsstrahlung power density loss

Reference	Formula	SI Conversion
Glasstone and Lovberg [26]	$P_{\text{br}}/V = 1.57 \times 10^{-27} n_e n_i Z^2 T^{1/2}$ ergs/(cm ³ · s), with T in K.	$P_{\text{br}}/V = 1.57 \times 10^{-28} n_e n_i Z^2 T^{1/2}$ W/m ³
Rybicki and Lightman [27]	$P_{\text{br}}/V = 1.4 \times 10^{-27} n_e n_i Z^2 T^{1/2} \bar{g}_B$ ergs/(cm ³ · s), with T in K.	$P_{\text{br}}/V = 1.68 \times 10^{-28} n_e n_i Z^2 T^{1/2}$ W/m ³ , using $\bar{g}_B(T) = 1.2$

The first relation, from Glasstone and Lovberg [26] converted to SI, was used for the remainder of the calculations.

There was also a question regarding whether this plasma was a surface emitter or a volume emitter. This was determined by calculating the plasma frequency at a typical electron density and comparing it to the wavelength of the light emitted by Bremsstrahlung. If the plasma frequency was higher than the wavelength of emitted Bremsstrahlung light, then it was cut off by the plasma; no light could escape directly from the inside of the LSP cone, and it was a surface emitter. If it was lower, then the emitted photons were not blocked by the LSP and the cone was a volumetric emitter.

The plasma frequency ω_p was found with:

$$\omega_p = \sqrt{\frac{n_e e^2}{\epsilon_0 m_e}} \quad (4.9)$$

With n_e the plasma electron density, e the elementary charge, ϵ_0 the vacuum permittivity, and m_e the electron mass.

In the worst case scenario (highest temperature and pressure) of 20 000 K and 20 bar, an electron density of 3.05×10^{21} was found. This resulted in $\omega_p = 3.11 \times 10^{12}$ Hz. Considering visible light and above ($> 1 \times 10^{14}$ Hz) as the wavelengths of interest, the LSP was indeed a volume emitter.

4.3 Model setup

Finally, a 0D model was written in Python to attempt to explain the pressure rise seen in the LTP experiments. [Figure 4.3](#) illustrates this model. Laser energy is focused into a volume of argon, creating an LSP cone. Energy is transferred from the LSP cone to the larger argon volume by Bremsstrahlung. A part of the laser energy is also transmitted through the cone to the outside of the argon volume and lost, but this was not modelled. The LSP was treated as an ideal gas.

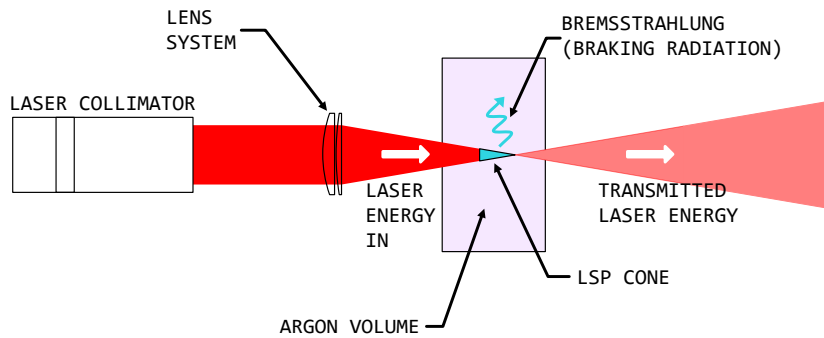


Figure 4.3: Model of an LSP inside a volume of pressurized argon

The calculation procedure implemented in the 0D model was as follows:

1. The volume V_{plasma} and the mass m_{plasma} of a cone of pure argon were found at the initial temperature ($T_{\text{ini}} = 300 \text{ K}$) and pressure ($p_{\text{ini}} \approx 20 \text{ bar}$, set to the experimental measurement done before each shot). This was the mass of argon plasma and will remain fixed for the rest of the problem. This fixed mass could be a source of error, as the plasma propagates as described in [Figure 5.9](#). The length (l_{plasma}) and radius (r_{plasma}) of the plasma cone were taken from previous observations in Duplay [4] when the cone reached equilibrium near the end of a laser pulse. The argon volume contained in the V1 test section was 0.4 L.

$$l_{\text{plasma}} = 0.02 \text{ m}, r_{\text{plasma}} = 0.001 \text{ m} \quad (4.10)$$

$$V_{\text{plasma}} = \frac{\pi r_{\text{plasma}}^2}{3} \quad (4.11)$$

$$m_{\text{plasma}} = V_{\text{plasma}} \rho(T_{\text{ini}}, p_{\text{ini}}) \quad (4.12)$$

2. The energy in the plasma E_{plasma} was calculated, starting at 0 J. Energy from the laser pulse was added to the cone while the energy lost from radiation, calculated at the previous iteration, was subtracted. These were calculated from their respective powers P .

$$E_{\text{plasma}} = E_{\text{plasma}} + \underbrace{P_{\text{laser}} \times \text{timestep}}_{\text{Energy from the laser pulse}} - \underbrace{P_{\text{loss}} \times \text{timestep}}_{\text{Energy lost by radiation}} \quad (4.13)$$

The new temperature (T_2) of the cone at this step was found at constant pressure,

$$E_{\text{plasma}} = m_{\text{plasma}} (h_2(T_2, p_{\text{ini}}) - h_1(T_{\text{ini}}, p_{\text{ini}})) \quad (4.14)$$

where this equation was solved for T_2 . The enthalpy of the argon was found with the relations implemented in [Section 4.1](#).

3. The number of moles n in the cone was found by minimizing the Gibbs free energy (see again [Section 4.1](#)) at the temperature and pressure of step 2 (T_2, p_2). This gave the ionization fraction x .

$$n = \frac{m_{\text{plasma}}}{M_{\text{Ar}}} (x + 1) \quad (4.15)$$

The atomic mass of argon is $M_{\text{Ar}} = 39.948$ u. The new volume of the cone (V_2) was then found with the ideal gas law.

$$V_2 = \frac{n\bar{R}T_2}{p_2} \quad (4.16)$$

With the universal gas constant \bar{R} .

4. The pressure increase p_4 of the larger argon volume in the V1 chamber (0.4 L) due to the isentropic expansion of the gas in the LSP cone was calculated.

$$p_4 = p_{\text{ini}} \left(\frac{V_{\text{chamber}} - V_{\text{plasma}}}{V_{\text{chamber}} - V_2} \right)^\gamma \quad (4.17)$$

With $\gamma = 1.67$, the heat capacity ratio of argon at 300 K. p_2 was set equal to p_4 at this point, so that the LSP cone would be at the same pressure as the surrounding gas for the next iteration.

5. The radiated power from the LSP cone to the larger argon volume was determined for the next iteration. The Bremsstrahlung power density loss equation from Glasstone

and Lovberg [26] was used, multiplied by the volume V_2 of the LSP.

$$P_{\text{br}} = 1.57 \times 10^{-28} n_e n_i Z^2 T_2^{1/2} V_2 \quad (4.18)$$

With $Z = 1$, as the argon was singly ionized.

6. Steps 2 to 5 were looped until 10 ms, when laser energy deposition ended. No more energy was added but Bremsstrahlung loss continued. The conservation of energy equation thus became:

$$E_{\text{plasma}} = E_{\text{plasma}} - P_{\text{loss}} \times \text{timestep} \quad (4.19)$$

To determine an upper bound for power loss, a switch was implemented to change Bremsstrahlung loss to blackbody radiation loss. This would be the case if the LSP was a surface emitter. The power loss was computed by first finding the area of the cone A_{plasma} . The length was found from the volume of the cone (which is known), while the radius was considered fixed at $r_{\text{plasma,fixed}} = 0.001$ m.

$$l_{\text{plasma}} = \frac{3V_{\text{plasma}}}{\pi r_{\text{plasma,fixed}}^2} \quad (4.20)$$

The area of the cone and the power loss are then found.

$$A_{\text{plasma}} = \pi r_{\text{plasma,fixed}} (r_{\text{plasma,fixed}} + \sqrt{l_{\text{plasma}}^2 + r_{\text{plasma,fixed}}^2}) \quad (4.21)$$

$$P_{\text{loss}} = \sigma T_2^4 A_{\text{plasma}} \quad (4.22)$$

With the Stefan-Boltzmann constant σ .

4.4 Model results

From these iterations, pressure rise curves with Bremsstrahlung loss and blackbody radiation loss were determined. These curves were overlaid on experimental data from LSP178_SPRK49, a 10 ms QCW LSP experiment at 3079 W and 19.91 bar of argon to give Figure 4.4.

Using Bremsstrahlung loss, the model appropriately approximated the first peak seen in the experimental data. Once the gas cooled down enough and stopped being ionized, Brems-

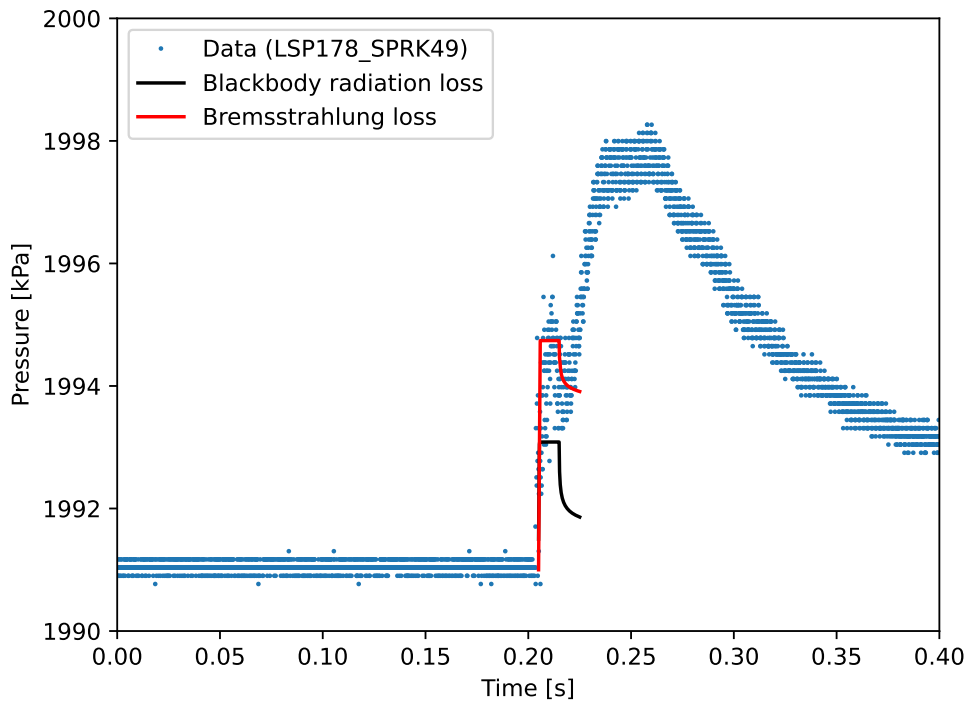


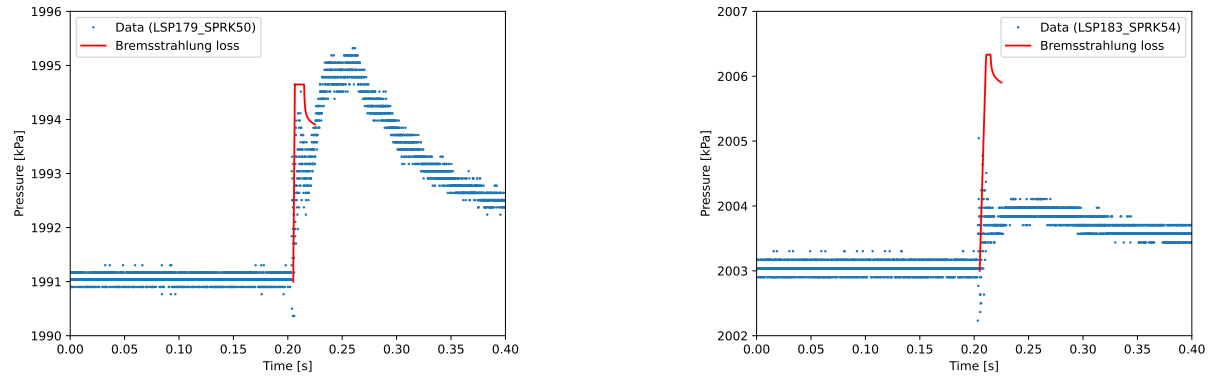
Figure 4.4: Experimental data compared to the 0D model, with both Bremsstrahlung and blackbody losses

trahlung loss also stopped. The LSP cone in the model was then stable at approximately a temperature of 5200 K and a pressure of 2.003 MPa. As expected, the pressure rise was lower with blackbody radiation, as the loss was greater.

Further investigation has shown that the model was not as sensitive as the experiments to a decrease in laser power, as can be seen in [Figure 4.5](#).

Finally, [Figure 4.6](#) shows how the pressure rise increased as the laser power was increased.

For reference, [Table 4.2](#) contains the initial values of each model run used for [Figure 4.6](#). Each run took around 15 minutes to compute on a laptop.



(a) LSP179_SPRK50, 1540 W (50% power)
and initial pressure of 19.91 bar

(b) LSP183_SPRK54, 345 W (15% power)
and initial pressure of 20.03 bar

Figure 4.5: Pressure change over time during two further LSPs, with Bremsstrahlung loss

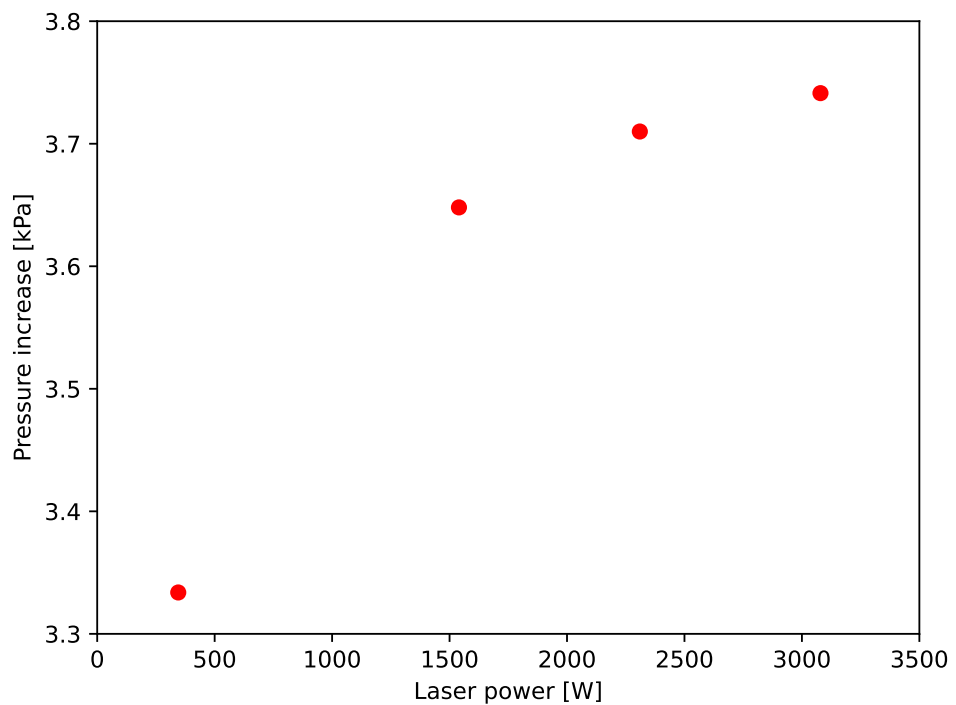


Figure 4.6: Pressure increase from 0D model as a function of laser power, with initial pressure of 20 bar

Table 4.2: Initial values for 0D model

Shot ID	P_{laser} (W)	P_{laser} (%)	p_{ini} (bar)	Time step (s)	Source of P_{laser} (W)
LSP176_SPRK47	2310	75	19.91	50×10^{-6}	Maximum power multiplied by %
LSP178_SPRK49	3079	100	19.91	10×10^{-6}	Maximum power
LSP179_SPRK50	1540	50	19.91	10×10^{-6}	Maximum power multiplied by %
LSP183_SPRK54	345	15	20.03	10×10^{-6}	Extrapolated from Table 3.1

Chapter 5

Discussion

A comprehensive discussion on the findings will now be presented, first on the experiment and then on the model.

5.1 Experiment

This project was started on the heels of Duplay [4], with the V1 test section using wire initiation. In this experiment, spark initiation was preferred to wire initiation for a few reasons. First, there would be no solid object blocking the beam path. This would allow the power meter to measure the energy that was not absorbed by the plasma. Second, replacing the target wire was a time-consuming process that was conducted every 1–3 shots, requiring the test section to be re-pressurized. Indeed, spark initiation enabled a much higher shot rate. Third, when conducting flowing experiments, the wire could be moved out of the focus by the flowing argon. Finally, the wire prevented the downstream propagation of the plasma by being physically in the way.

With V1, spark initiation was first attempted with two side by side electrodes that could fit into a single port, seen in [Figure 5.1](#). However, the spark was created at a different height every time between the parallel electrodes.

Using opposing electrodes would ensure that their tips were always the closest point to each other, greatly increasing spatial repeatability of the spark and enabling the electrode gap length to be easily adjusted. Opposing ports ([Figure 5.2](#)) were drilled into the bottom of the V1 apparatus to fit an electrode through the top and one through the bottom, as seen in [Figure 3.1b](#).

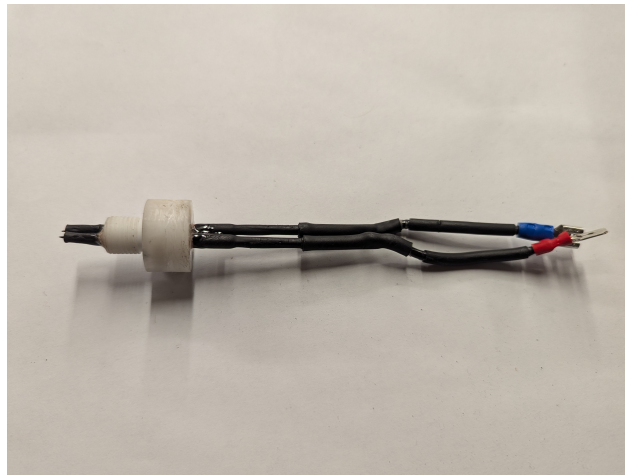


Figure 5.1: V1 single plug electrodes



Figure 5.2: V1 with newly machined opposing bottom ports

Another critical issue was burnout of the automotive-type coils used in the spark initiation system. Five such coils were damaged to the point that they could no longer create a strong enough spark across the spark gap. A contributing factor could have been the poor electrode retention of the Ultra-Torr fittings, as 20 bar of gas could visibly push the electrodes away 1 mm to 2 mm. An increase in the spark gap increases its resistance, putting a higher load on

the coil. Another concern was electromagnetic interference between the coil and its power supply. Originally in the same box, the 10 A current-limited power supply and the smart coil were placed in separate electrical boxes (see [Figure 2.10](#)). Quad shielded coaxial cable was used between the coil and its controlling delay generator as an additional precaution.

Spatial alignment and timing synchronization of the laser focus to the spark was completed, and reliable spark initiation of LSP was achieved in V1. NO₂ seeding tests were then undertaken to determine if more laser energy could be captured by the propellant. With as low as 0.6% of NO₂ partial pressure mixed with argon, double the pressure rise was observed. This indicated that the propellant was absorbing twice the energy from the plasma. As the NO₂ fraction was increased, there were diminishing returns to the pressure rise. This was encouraging, as not much NO₂ was needed to have a great impact on the energy absorption.

The V1 started showing downsides when it was being set up for thrust tests. Due to the weight of its steel construction, it created too much friction on its rails during cold flow thrust tests. This was mitigated in part by a rope system mentioned in Duplay [4] but was not found to be repeatable. Having the LSP heat a smaller internal volume than the 0.4 L of V1 was also desirable, as a greater effect on internal pressure and thrust would be seen. Critically, rubber seals were exposed to the laser path during continuous (CW) lasing with a lower focal length lens, severely melting them in the only V1 CW test conducted. A shorter test section designed for a 100 mm focal length lens would allow the beam to pass through without hitting the sides of the test section. A smaller purpose-built test section, named V2, was therefore designed.

The achievement of consistent spark initiation with V1 coincided with the arrival of the V2 test section parts. Proof pressure testing of V2 up to 75 bar for 25 minutes was completed successfully. Unfortunately, the off-the-shelf 44 kV wire originally intended to be used as the electrodes burst during pressure tests. An electrode redesign was therefore necessary. Molded dielectric epoxy (Loctite® Stycast ES 1001 from McMasterCarr) around an industrial sewing needle core was chosen, as it was economical and the outer diameter of the electrodes could be precisely controlled by sanding the surface of the set epoxy. Molds were 3D printed and Mann Ease Release™ 300 was applied to all their inside surfaces.

The electrodes were then sanded down to fit tightly into Ultra-Torr vacuum connectors. Although these connectors were not designed for high pressure, previous experience has shown that they are appropriate up to about 20 bar if tightened enough. The result is presented in [Figure 5.3c](#). Once installed in the V2 thruster, the electrodes were pushed into contact with each other and the Ultra-Torr connectors tightened. Statically pressurizing V2

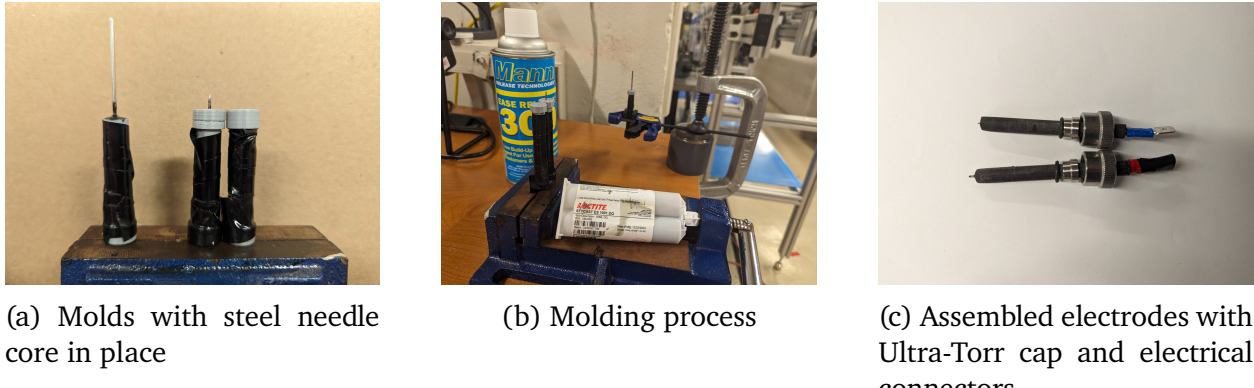


Figure 5.3: Electrode manufacturing process

to 20 bar was enough to separate the electrodes from one another by about 1 mm.

With a dual-lens system, static LSP via spark initiation in V2 was achieved on the first QCW shot at 100% power (3079 W). This was initially done with a flat aluminum plate at the end of the test section (see [Figure 5.4](#) and [Appendix D](#)).

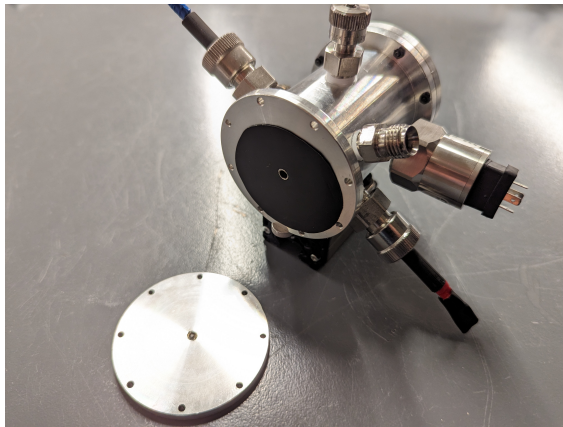


Figure 5.4: Ablation damage to the flat rear plate of the thruster after two 3 kW laser shots

The black sheet in [Figure 5.4](#) is Thorlabs laser-absorbing aluminum foil, used in a failed attempt to protect the rear plate from damage. In addition to this ablation problem, the laser could only be aligned between the electrodes when the rear plate was taken off. This required re-pressurization after every attempt at alignment. Given that the electrodes would also move under the 20 bar pressure, this was very tedious.

To solve this, a second window holder was machined ([Appendix E](#)) to replace the flat plate. The laser could then be aligned when the test section was pressurized, and the alignment could be changed without opening the thruster. The window allowed the laser energy that was not absorbed by the plasma to pass freely through the apparatus, also enabling power

meter measurements. With the new window mount installed, the goal was then to bring the QCW initiation power down to the maximum CW power of the laser, 342 W, in order to attempt a CW LSP.

A dual-lens system was designed to increase laser flux at the focus by decreasing the area of the focus while keeping the power constant. The lenses were validated with V1 and used in all of V2's LSP shots. Once LSPs lower than 342 W were initiated reliably, our first 100% power (342 W) CW LSP was generated for 85.1 ms, a 1.7 times longer lifetime than the maximum QCW pulse length of 50.0 ms. While these results were encouraging, more experiments with CW laser operation must be completed to determine if lifetimes can be extended to an order of magnitude more, i.e. around one second. This would help with measuring a difference in thrust when the laser is on, as the energy transmitted to the gas would also be increased by the same amount.

After the first CW LSP, more CW and pulsed shots were attempted. These continued to damage the rear window, as seen in the center of [Figure 5.5](#). Eventually, a 3 s CW shot melted it severely enough that visual laser alignment between the electrodes of V2 was no longer possible. A window extension tube (seen in [Figure 5.6](#), drawings in [Appendix F](#))

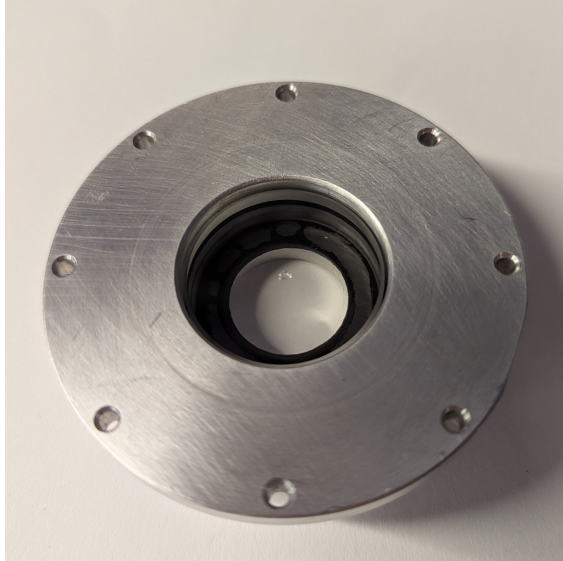


Figure 5.5: Rear window damage on V2

was manufactured to solve this, moving the rear window downstream to where the laser flux was comparable to the front window, where no damage was seen. This extension tube has yet to be tested.

In parallel to the static LSP validation, characterization of the thruster with argon cold flow was advanced. High hysteresis of the thrust measurements was found, with the thrust stand

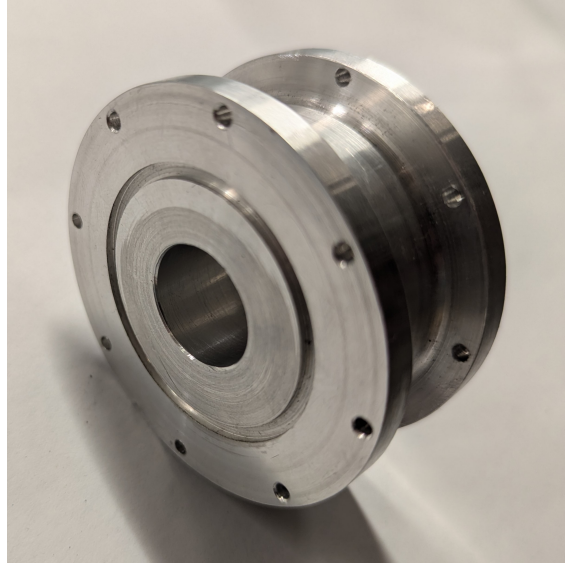


Figure 5.6: Window extension tube

often not returning to its original zero after a cold flow test. To attempt to correct these problems, a more sensitive load cell was installed with a 0 N to 5 N force sensing range (Honeywell FSG005WNPB). Lubricant was also added to the cart's bearings. However, the hysteresis issue remained (see [Figure 3.17](#)) due to high friction between the rail and the ball bearing carriage preventing the thruster from resetting at the same place every time. The present thrust stand is therefore inadequate for future thrust tests and a new one should be built to measure thrust repeatably and reliably.

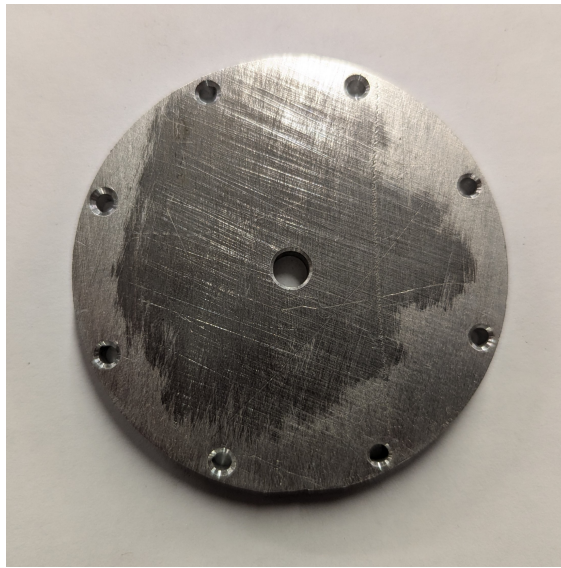
Initial QCW LSP (pulsed hot fire) thrust tests aimed to determine if QCW LSP initiated by a spark in flowing argon was possible with V2, and if usable thrust data could be collected. It was shown that LSP could be initiated, and a change of thrust was measured, but this was due to nozzle ablation in all cases. [Figure 3.21](#) shows nozzle ablation during a QCW flowing test without LSP, with [Figure 5.7](#) showing the damage to the nozzle afterward. No LSP was initiated in this test, however a plasma plume can be seen exiting the nozzle. This plasma was again generated by nozzle ablation, proving that this experiment can operate as a laser ablation thruster. This result was not what the thruster was designed for and lead to a redesign of the V2 nozzle.

To solve the ablation of the aluminum nozzle under pulsed laser shots, a new backplate ([Figure 5.8a](#) and [Appendix F](#)) was manufactured to accept nozzle inserts. Toyoda *et al.* [13] used a refractory metal, tungsten, as the nozzle material. Other possibilities are machinable ceramics, stainless steel, or graphite. Graphite was chosen as it was already used by Shoji [6] and was economical. These inexpensive, changeable inserts ([Figure 5.8b](#) and [Ap-](#)

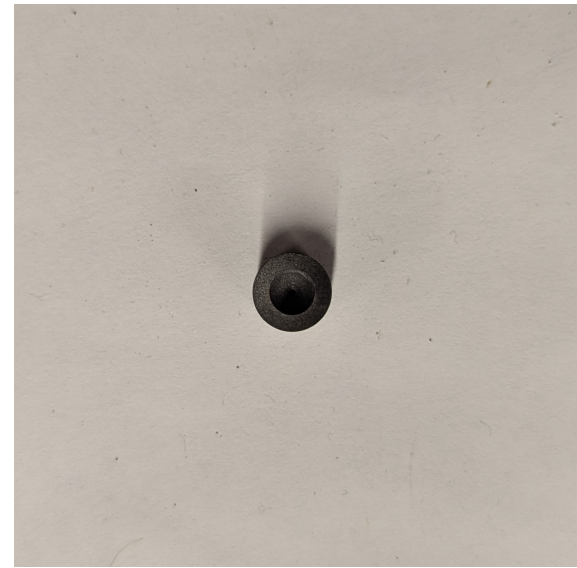


Figure 5.7: Nozzle laser damage

pendix F) were made from superfine iso-molded graphite rods sourced from Graphitestore (0.500" diameter x 12"L, SKU GT001685). V2's inner cylinder was also re-machined ([Appendix F](#)) to guarantee a seal with the new nozzle. Due to machining delays, these final parts are still to be tested.



(a) Nozzle retention plate



(b) Graphite nozzle insert

Figure 5.8: New nozzle parts

Longer term, to ultimately test LTP as a viable means of space propulsion, more improvements to the V2 setup can be envisioned. A simple but costly one is to use a more powerful

laser, instead of the 300 W CW one used here. This would increase thrust and laser absorption by the plasma, making an eventual thrust increase easier to detect. Using hydrogen as a propellant instead of argon would increase the thruster's specific impulse. However, it would be harder to ionize, possibly requiring higher laser power or better focusing optics. A hydrogen LTP thruster would also need to be run inside a vacuum chamber, as hydrogen is extremely flammable.

5.2 Model discussion

Using a model for Bremsstrahlung loss, the zero-dimensional (0D) heat transfer model successfully approximated the order of magnitude and the timescale of the first of two pressure increases seen in experiments ([Figure 4.4](#)). The second, higher, peak could be explained by the fact that after the laser pulse, the energy in the cone was then communicated to the bulk argon volume. This equalization of temperatures and pressures could be due to natural convection. To test this hypothesis in future studies, the timescales of radiation and convection should be determined with the geometry of the problem.

In [Figure 4.5](#), the model increasingly overshot the experimental pressure data as the laser power was decreased. A potential cause for this was that laser energy transmission was not taken into account in the model, and a measurement of this transmission was not taken experimentally. As the laser power was lowered, the fraction of laser energy that was absorbed by the plasma (laser absorption efficiency) also decreased.

The LSP growth mechanism ([Figure 5.9](#)) was also not modelled, but it is useful to understand the physics at play.

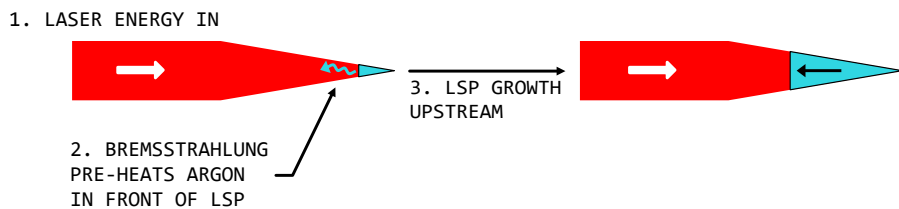


Figure 5.9: Mechanism of LSP growth

The laser creates at first a small LSP volume near the focus, where the laser flux is highest. As the plasma radiates via Bremsstrahlung, the argon around the plasma is heated. Being

exposed to the laser beam, the argon in front of the LSP ionizes. This causes the plasma to propagate towards the laser collimator until equilibrium is reached between radiation and heat dissipation. This reduces the absorption efficiency of the plasma, as the thicker part of the cone is no longer at the laser's focus, where the highest laser flux, and therefore temperature, can be reached. Gas flow up to a certain velocity can be used to push the plasma back into the focus, as was explained in Chen and Mazumder [11]. Too high a gas flow speed, and the plasma is blown out. Future experimental investigation of the V2 thruster could determine what the ideal flow speed is.

Chapter 6

Conclusion

6.1 Summary

Using a $1.07\text{ }\mu\text{m}$ fiber laser, a Version 1 (V1) lab-scale Laser Thermal Propulsion (LTP) thruster was tested, while an improved Version 2 (V2) thruster was designed and tested. This thesis lays the groundwork for future LTP thrust tests with longer plasma lifetimes and better thrust measurement, which would show the thrust added by the laser. A 0D heat transfer model was also written to interpret the experimental data.

Static LSP tests showed successful spark initiation of QCW LSP in V1 and V2, and an 85.1 ms CW LSP. A new window mount for V2 was designed and used in static tests. NO_2 seeding was also investigated in V1 as a way to increase energy retention by the gas and resulted in a twofold increase in argon dynamic pressure.

Cold flow thruster characterization measured thrust of about 1 N at 20 bar. To get repeatable thrust measurements without significant hysteresis, the need for a new thrust stand design with less friction was made clear. Flowing QCW LSP tests led to a new nozzle design to prevent significant ablation due to laser energy that was not absorbed by the LSP.

Measurements of the mass flow rate \dot{m} of V2 with the bubble flow meter are still to be completed. Once the new parts for V2 are installed and pressure tested, CW LSP tests can restart to explore longer plasma lifetimes.

6.2 Future work

The following recommendations for future work are further discussed in [Chapter 5](#).

On the experiment:

- Implement a new type of thrust stand that would reduce friction to obtain reliable thrust measurements: high friction between the rail and the ball bearing carriage created significant hysteresis in the thrust data. The load cell value corresponding to zero thrust was different before and after cold gas flow.
- Validate that the new parts fabricated for V2 solve the problems they were designed to solve: the new nozzle insert and retention plate were designed to minimize throat ablation from the laser. An extension cylinder was designed to move the rear window to where the laser flux would be low enough to not damage it. These parts must also hold pressure.
- Determine the ideal propellant flow speed to obtain the highest thermal efficiency (power retained by the gas divided by incident laser power): the LSP grows towards the laser source. An optimum flow speed would be where the core of the LSP is pushed by the gas flow back to the laser focus, but not beyond.
- Use a more powerful laser: higher laser power generates higher thermal efficiency. This is also necessary to scale the technology towards operation in space.
- Investigate using hydrogen as a propellant instead of argon: as the lightest element, hydrogen would have the greatest I_{sp} of all propellants. Due to this, hydrogen is the propellant that is projected to be used in a full-scale LTP engine.
- Start thrust tests in a vacuum chamber: necessary if hydrogen is used due to its flammability. This will validate the technology in an environment similar to space.

On the model:

- Determine the timescales of radiation and convection with the geometry of the LSP to explain the second pressure peak: as the 0D model shows, the first peak seen in pressure measurements is explained by Bremsstrahlung (braking radiation) loss of the LSP. Given that radiation is faster to communicate energy than convection, the second peak could be due to convective losses of the LSP.
- Account for the fraction of laser energy that was absorbed by the plasma, as the present model uses 100 % absorption: from previous measurements, it was found

that a significant amount of laser energy passes through the plasma without being absorbed. Modeling this efficiency could be a simple way to improve the model's accuracy.

- Develop a 1D model to explain the lengthwise growth of the LSP through time: as time progresses, the LSP grows towards the laser source. This reduces absorption efficiency in a static gas, as the plasma core moves away from the laser focus.

References

- [1] P. Lubin, “A Roadmap to Interstellar Flight,”
Journal of the British Interplanetary Society, vol. 69, no. 2, pp. 40–72, 2 Feb. 2016.
DOI: [10.48550/arXiv.1604.01356](https://doi.org/10.48550/arXiv.1604.01356).
- [2] A. Kantrowitz, “Propulsion to Orbit by Ground-Based Laser,”
Astronaut. Aeronaut., no. 10, pp. 34–35, 1971.
- [3] E. Duplay, Z. F. Bao, S. Rodriguez Rosero, A. Sinha, and A. Higgins, “Design of a rapid transit to Mars mission using laser-thermal propulsion,”
Acta Astronautica, vol. 192, pp. 143–156, Mar. 1, 2022, ISSN: 0094-5765.
DOI: [10.1016/j.actaastro.2021.11.032](https://doi.org/10.1016/j.actaastro.2021.11.032).
- [4] E. Duplay, “Argon Laser-Plasma Thruster: Design and Test of a Laboratory Model,”
M.S. thesis, Technical University Delft, Delft, 2024, 149 pp. [Online]. Available:
<https://repository.tudelft.nl/islandora/object/uuid%3A3a853f2e-2d8c-496b-a016-9e9855e8069c> (visited on 2024-02-02).
- [5] N. A. Generalov, V. P. Zimakov, G. I. Kozlov, V. A. Masyukov, and Yu. P. Raizer, “Continuous optical discharge,” *Soviet Journal of Experimental and Theoretical Physics Letters*, vol. 11, pp. 302–304, 1970.
- [6] J. M. Shoji, “Laser-heated rocket thruster,” NASA-CR-135128, Apr. 12, 1977.
[Online]. Available: <https://ntrs.nasa.gov/citations/19770017244>.
- [7] J. Shoji and V. Larson, “Performance and heat transfer characteristics of the laser-heated rocket - A future space transportation system,”
in *12th International Electric Propulsion Conference*,
American Institute of Aeronautics and Astronautics, Nov. 14, 1976.
DOI: [10.2514/6.1976-1044](https://doi.org/10.2514/6.1976-1044).
- [8] D. Keefer, R. Welle, and C. Peters, “Power absorption in laser-sustained argon plasmas,” *AIAA Journal*, vol. 24, no. 10, pp. 1663–1669, Oct. 1986,
ISSN: 0001-1452. doi: [10.2514/3.9498](https://doi.org/10.2514/3.9498).

REFERENCES

- [9] H. Krier, J. Mazumder, T. Rockstroh, T. Bender, and R. Glumb, “Continuous wave laser gas heating by sustained plasmas in flowing argon,” *AIAA Journal*, vol. 24, no. 10, pp. 1656–1662, Oct. 1986, ISSN: 0001-1452. doi: [10.2514/3.9497](https://doi.org/10.2514/3.9497).
- [10] D. K. Zerkle, S. Schwartz, A. Mertogul, X. Chen, H. Krier, and J. Mazumder, “Laser-sustained argon plasmas for thermal rocket propulsion,” *Journal of Propulsion and Power*, vol. 6, no. 1, pp. 38–45, 1990, ISSN: 0748-4658. doi: [10.2514/3.23220](https://doi.org/10.2514/3.23220).
- [11] X. Chen and J. Mazumder, “Emission spectroscopy of cw CO₂ laser-sustained argon plasma: Effects of gas-flow speed,” *Journal of Applied Physics*, vol. 66, no. 12, pp. 5756–5762, Dec. 15, 1989, ISSN: 0021-8979. doi: [10.1063/1.343644](https://doi.org/10.1063/1.343644).
- [12] J. Black, H. Krier, and R. J. Glumb, “Laser Propulsion 10-kW Thruster Test Program results,” *Journal of Propulsion and Power*, vol. 11, no. 6, pp. 1307–1316, 6 Nov. 1995, ISSN: 0748-4658, 1533-3876. doi: [10.2514/3.23973](https://doi.org/10.2514/3.23973).
- [13] K. Toyoda, K. Komurasaki, and Y. Arakawa, “Thrust performance of a CW laser thruster in vacuum,” *Vacuum*, 3rd International Symposium on Applied Plasma Science (ISAPS 01), vol. 65, no. 3, pp. 383–388, 3 May 27, 2002, ISSN: 0042-207X. doi: [10.1016/S0042-207X\(01\)00446-8](https://doi.org/10.1016/S0042-207X(01)00446-8).
- [14] Q. Lu *et al.*, “Characteristic Diagnostics of a Laser-Stabilized High-Pressure Argon Plasma by Optical Emission Spectroscopy,” *IEEE Transactions on Plasma Science*, vol. 50, no. 9, pp. 2578–2587, Sep. 2022, ISSN: 1939-9375. doi: [10.1109/TPS.2022.3172977](https://doi.org/10.1109/TPS.2022.3172977).
- [15] T. Kamei, M. Matsui, and T. Ono, “Methane and Methane–Xenon Laser Sustained Plasma using High Power Diode Laser for Space Propulsion,” *Transactions of the Japan Society for Aeronautical and Space Sciences, Aerospace Technology Japan*, vol. 18, no. 5, pp. 271–275, 2020, ISSN: 1884-0485. doi: [10.2322/tastj.18.271](https://doi.org/10.2322/tastj.18.271).
- [16] S. Takano, Y. Homme, Y. Arakaki, and M. Matsui, “Demonstration of Diode Laser-sustained Argon Plasma Thruster using various F-number,” in *AIAA SCITECH 2024 Forum*, American Institute of Aeronautics and Astronautics, Jan. 4, 2024. doi: [10.2514/6.2024-2704](https://doi.org/10.2514/6.2024-2704).
- [17] S. Khan, D. Newport, and S. Le Calvé, “Gas Detection Using Portable Deep-UV Absorption Spectrophotometry: A Review,”

REFERENCES

- Sensors*, vol. 19, no. 23, p. 5210, 23 Jan. 2019, ISSN: 1424-8220.
DOI: [10.3390/s19235210](https://doi.org/10.3390/s19235210).
- [18] “Laser spot size and beam waist calculator and formulas,” Gentec-EO. (2024), [Online]. Available: <https://www.gentec-eo.com/laser-calculators/beam-waist-spot-size> (visited on 2024-07-25).
- [19] J. Hecht, *Understanding Lasers: An Entry Level Guide*, 4th ed. Hoboken: John Wiley & Sons, Inc., 2019, ISBN: 978-1-119-31064-8.
- [20] R. Paschotta. “Beam parameter product.” (2024), [Online]. Available: https://www.rp-photonics.com/beam_parameter_product.html (visited on 2024-03-26).
- [21] “Lens Tutorial,” Thorlabs. (2024), [Online]. Available: <https://www.thorlabs.com> (visited on 2024-07-30).
- [22] M. A. Saad, *Compressible Fluid Flow*. Englewood Cliffs.
- [23] M. Barigou and J. F. Davidson, “The fluid mechanics of the soap film meter,” *Chemical Engineering Science*, vol. 48, no. 14, pp. 2587–2597, Jul. 1, 1993, ISSN: 0009-2509. doi: [10.1016/0009-2509\(93\)80269-V](https://doi.org/10.1016/0009-2509(93)80269-V).
- [24] B. J. McBride, M. J. Zehe, and S. Gordon, *NASA Glenn Coefficients for Calculating Thermodynamic Properties of Individual Species*, Sep. 1, 2002. [Online]. Available: <https://ntrs.nasa.gov/citations/20020085330> (visited on 2024-07-15).
- [25] “CEARUN rev4.” (2024), [Online]. Available: <https://cearun.grc.nasa.gov/> (visited on 2024-07-26).
- [26] S. Glasstone and R. H. Lovberg, *Controlled Thermonuclear Reactions : An Introduction to Theory and Experiment*. Huntington, N.Y. : R. E. Krieger Pub. Co., 1975, 554 pp., ISBN: 978-0-88275-326-3. [Online]. Available: <http://archive.org/details/controlledthermo00glas>.
- [27] G. B. Rybicki and A. P. Lightman, *Radiative Processes in Astrophysics*. Weinheim, [Germany]: Wiley-VCH Verlag GmbH & Co. KGaA, 2004, 1 p., ISBN: 978-0-471-82759-7 978-3-527-61818-7.

Appendix A

YLR-300/3000-QCW-MM-AC Calibration Report

	TEST RESULTS YTTERBIUM FIBER LASER Model YLR-300/3000-QCW-MM-AC S/N PLMP31901422	Form: Revision: Spec: Page:	P69-00051 1 G22-29650 rev.4 1 of 6
---	---	--------------------------------------	---

This product is covered by the U.S. Pat. Nos. 5,422,897 and 5,774,484 and any foreign counterparts thereof, and other patents pending.

The information and the following charts provided below is the result of tests performed in controlled environments by IPG Photonics. These provided useful, but not warranted, information about the functions and performance of the product.

N	Characteristic	Symbol	Test Conditions	Min	Typ.	Max	Test Results	Unit
Optical characteristics								
1.1	Operation Mode						Pulsed / CW	
1.2	Maximum Average Power	P_{average}	Pulsed mode	300			307.9	W
		P_{CW}	CW mode	300			342.0	W
1.3	Maximum Peak Power	P_{peak}	Pulsed mode				3079.25	W
1.4	Duty Cycle	DC	Pulsed mode				50 ¹⁾	Tested %
1.5	Pulse Duration	τ	Pulsed mode	0.2			50 ²⁾	0.2-50 ms
1.6	Maximal Pulse Energy	E_{max}	Pulsed mode	30			30.8	J
1.7	Emission Wavelength	λ			1070		1069.6	nm
1.8	Emission Linewidth	$\Delta\lambda$	Pulsed mode maximum output power		5	6	1	nm
1.9	Long-term Power Instability		T = const maximum output power CW & Pulsed mode		± 0.5	± 1	± 0.5	%
Optical output								
2.1	Output Fiber Termination						QBH-compatible connector	Tested
2.2	Beam Quality	BPP ³⁾	50µm core fiber pulsed mode	1		2	2	mm x mrad
General characteristics								
3.1	Cooling Method						Forced Air	
Electrical characteristics								
4.1	Operating Voltage, single phase						200-240 VAC, 50/60 Hz	VAC

¹⁾ Maximum duty cycle limit is inversely proportional to peak power: 10% for 3000W, 15% for 2000W, ..., 50% for 600W and lower.

²⁾ Maximum pulse duration limit is inversely proportional to peak power: 10ms for 3000W, 15ms for 2000W, ..., 50ms for 600W and lower.

3) Measurement tolerance for BPP is +/- 10%.

	TEST RESULTS YTTERBIUM FIBER LASER Model YLR-300/3000-QCW-MM-AC S/N PLMP31901422	Form: Revision: Spec: Page:	P69-00051 1 G22-29650 rev.4 2 of 6
---	---	--------------------------------------	---

N	Characteristic	Test Conditions	Test Results
Laser Interfaces			
5.1	Control	Analog	Tested
		RS-232	Tested
		Ethernet	Tested

Date: 29.10.2019

Tested by: Henry Thepsimoung

Approved by: Thomas Rogers

This document has been created automatically and is valid without a signature

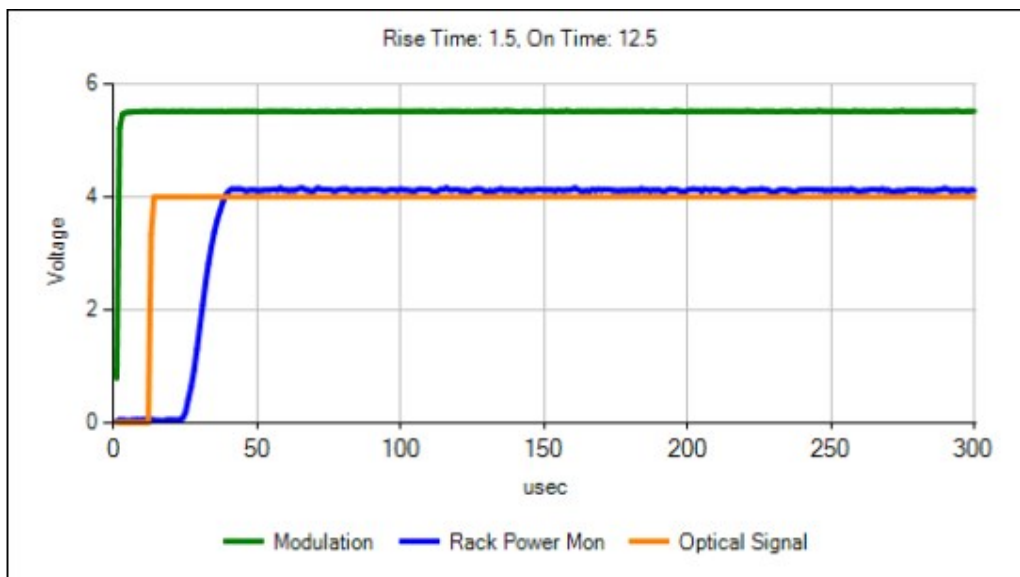


Fig. 1 Switching ON characteristic at nominal output power

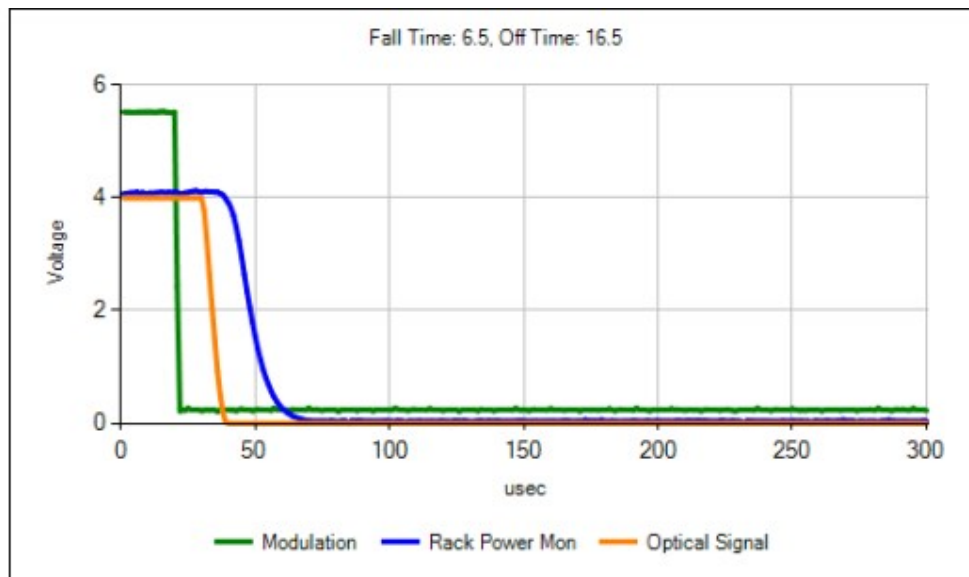


Fig. 2 Switching OFF characteristic at nominal output power

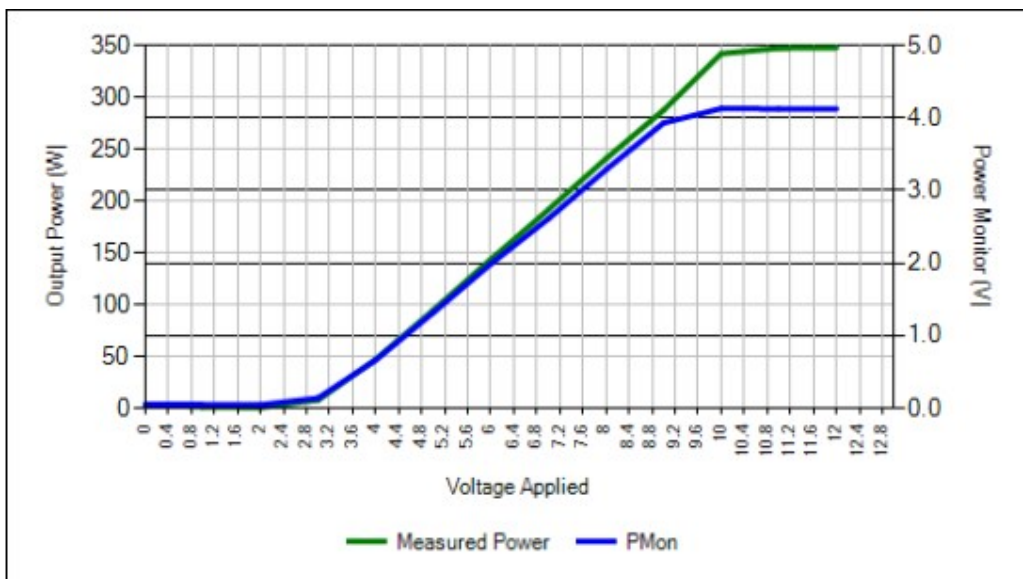


Fig. 3 CW Mode: Output Power vs. Analog Voltage

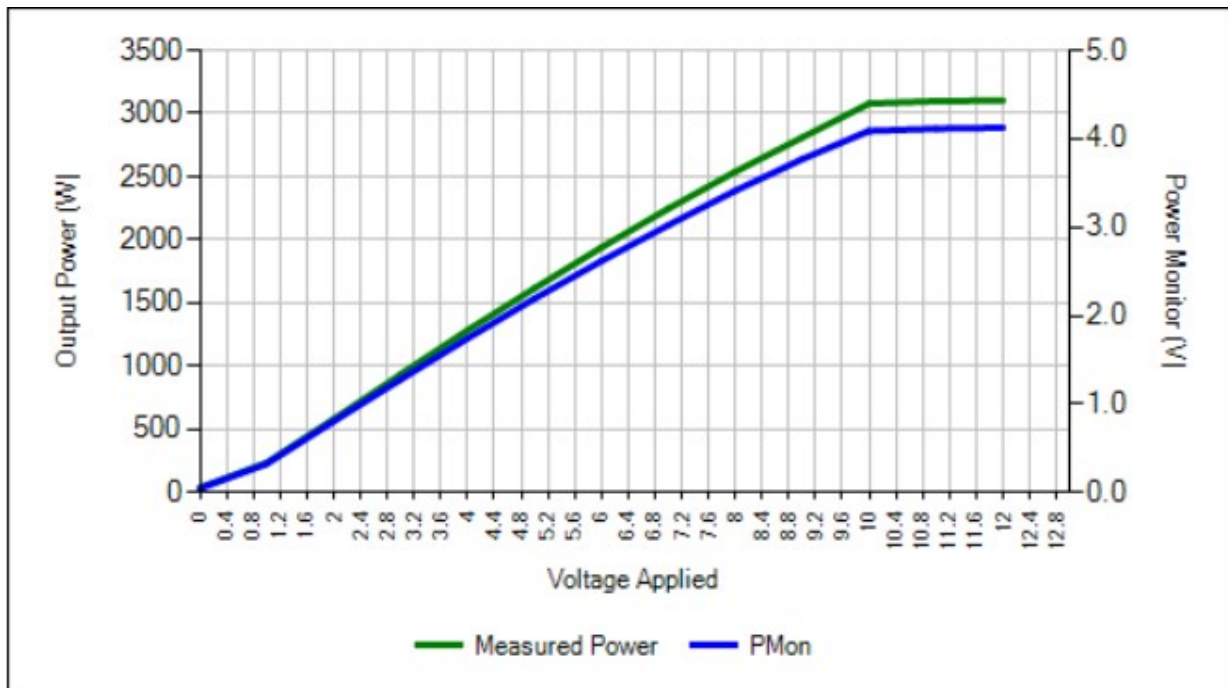


Fig. 4 Pulsed Mode: Peak Output vs. Analog Voltage at RR=10Hz, 10% Duty Cycle

IPG PHOTONICS	TEST RESULTS YTTERBIUM FIBER LASER Model YLR-300/3000-QCW-MM-AC S/N PLMP31901422	Form: Revision: Spec: Page:	P69-00051 1 G22-29650 rev.4 5 of 6
-------------------------	---	--------------------------------------	---

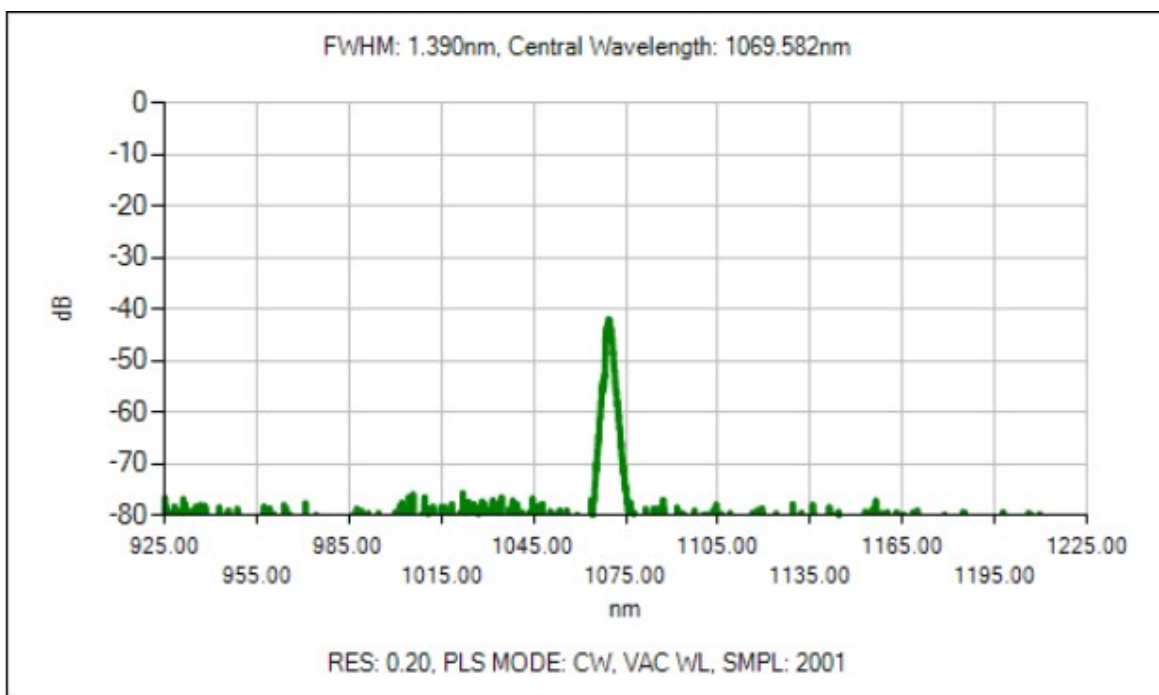


Fig. 5 Output Spectrum at Nominal Output Power

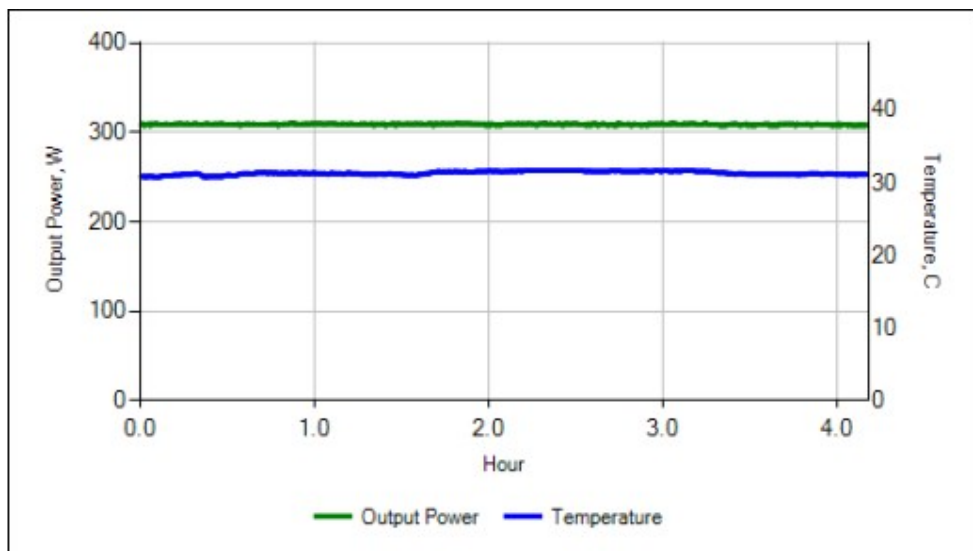


Fig. 6 Output Power Stability Chart

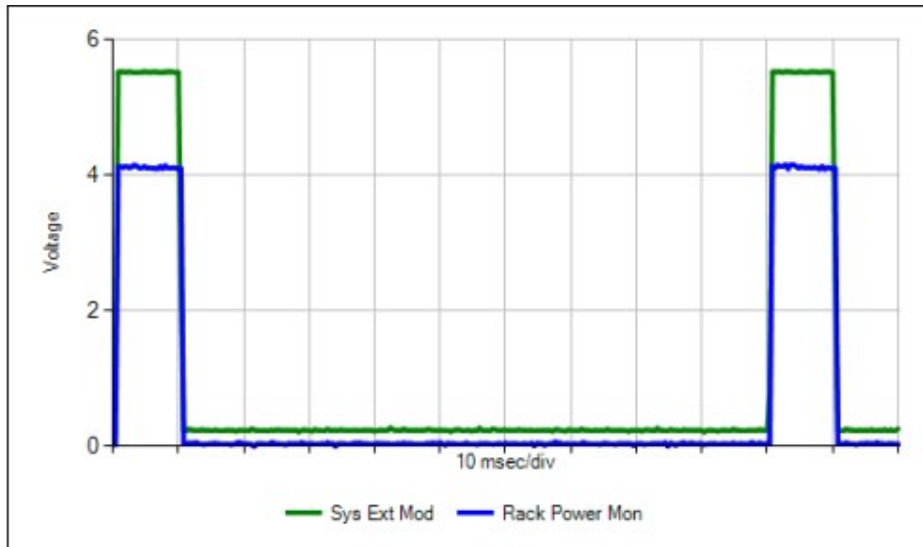


Fig. 7 Pulsed Mode: Laser Output Signal Frequency 10Hz (10% Duty Cycle)

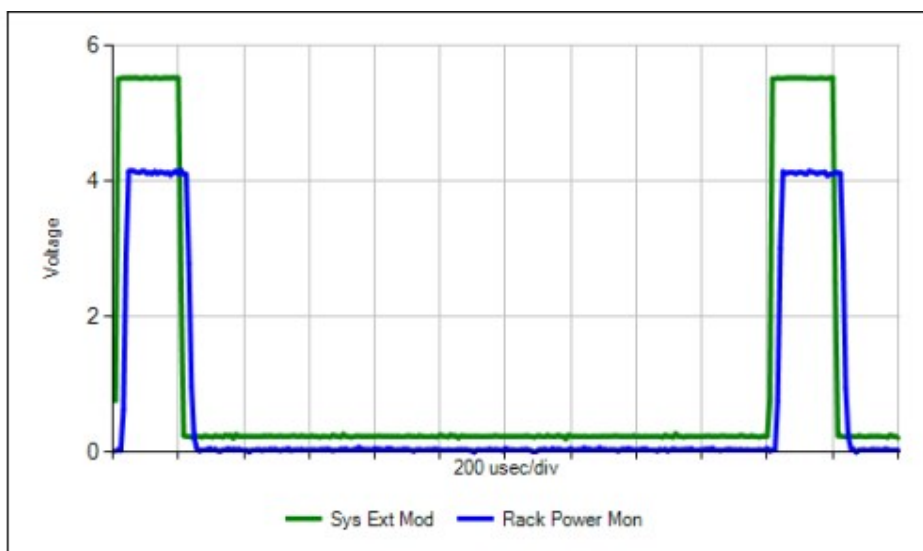


Fig. 8 Pulsed Mode: Laser Output Signal Frequency 500Hz (10% Duty Cycle)

Appendix B

P30 Collimator Calibration Report



Model: P30-001736

Serial Number: CO211706

Date: 3/29/2022 3:11:04 PM

Tested By: Ketsana Chanthavangso

Collimator Test Results Sheet

Characteristic	Conditions	Min.	Typical	Max.	Tested	Units
Z-Position	Measured at Beam Waist				-0.066	m
BPP	Algo. 2nd 100 W			2.5	1.472	mm*mrad
Safety Interlock	Circuit Continuity Tested				Pass	-
Leak Testing	80psi Air for 15min.					-

Raw-Beam:



Raw-Beam:

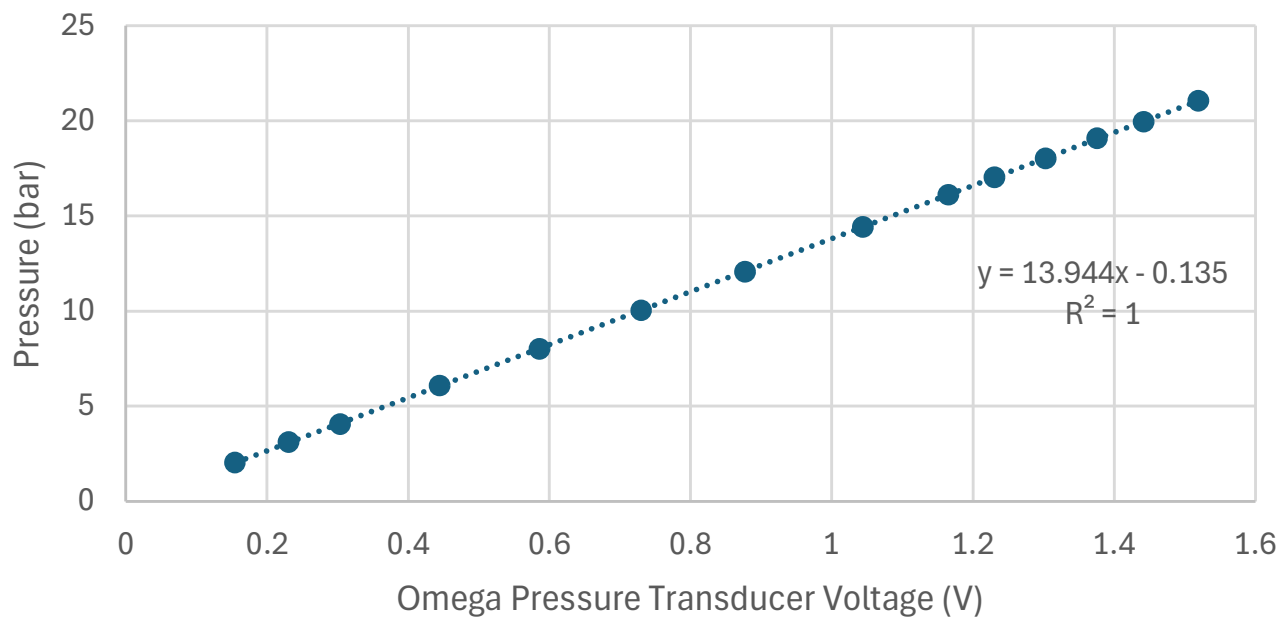
Position Z:	-66.288 [mm]
Position Z(X):	-3.131 [m]
Position Z(Y):	3.635 [m]
Raw-Beam Radius:	6.813 [mm]
Raw-Beam Radius (X):	6.814 [mm]
Raw-Beam Radius (Y):	6.917 [mm]
Rayleigh length:	31.531 [m]
Rayleigh length X:	29.099 [m]
Rayleigh length Y:	33.790 [m]
Divergence Angle:	0.432[mrad]
Divergence Angle (X):	0.455[mrad]
Divergence Angle (Y):	0.409[mrad]
Raw-Beam Dia. at Laser	13.626[mm]

Exit

Appendix C

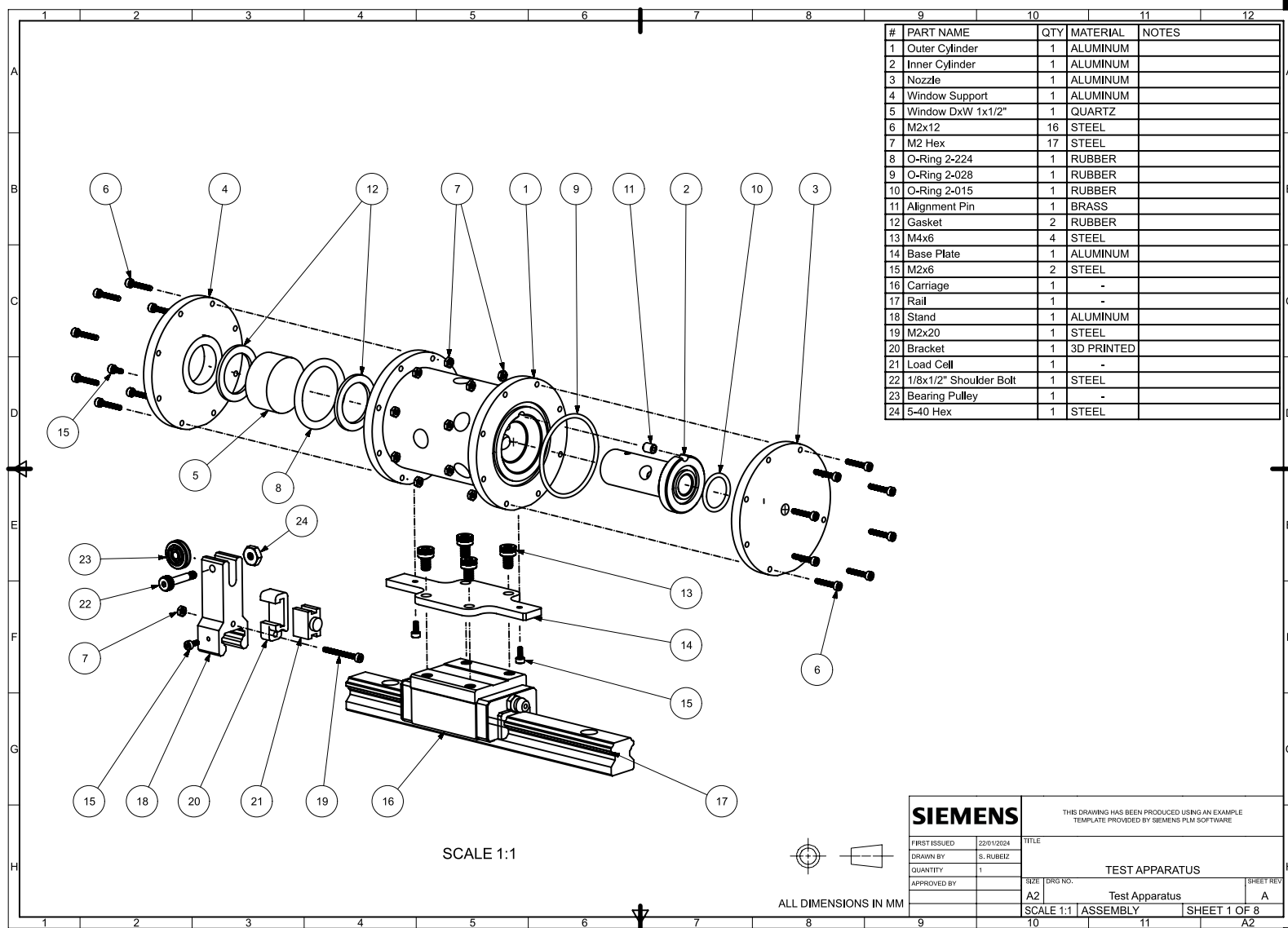
Omega PX119A-1KG5V Calibration

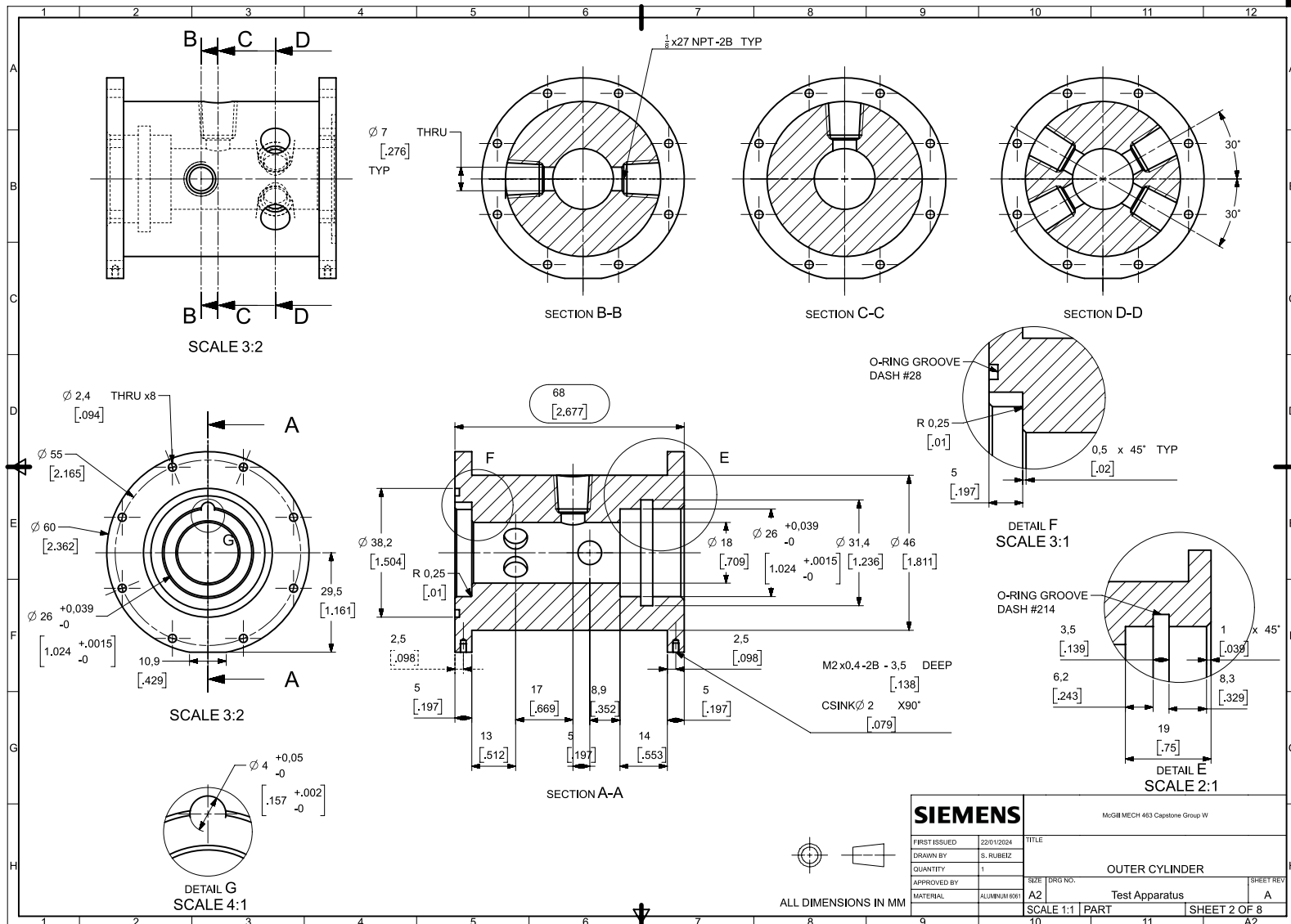
Omega PX119A-1KG5V Calibration

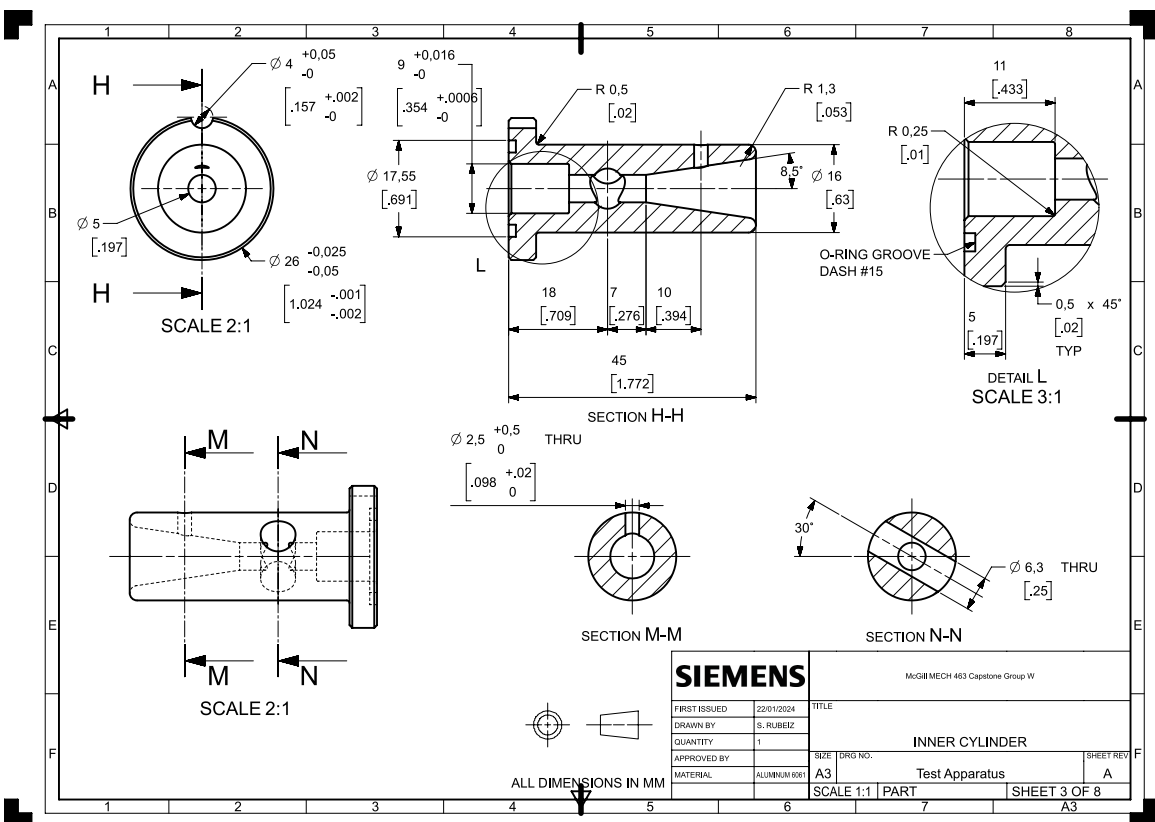


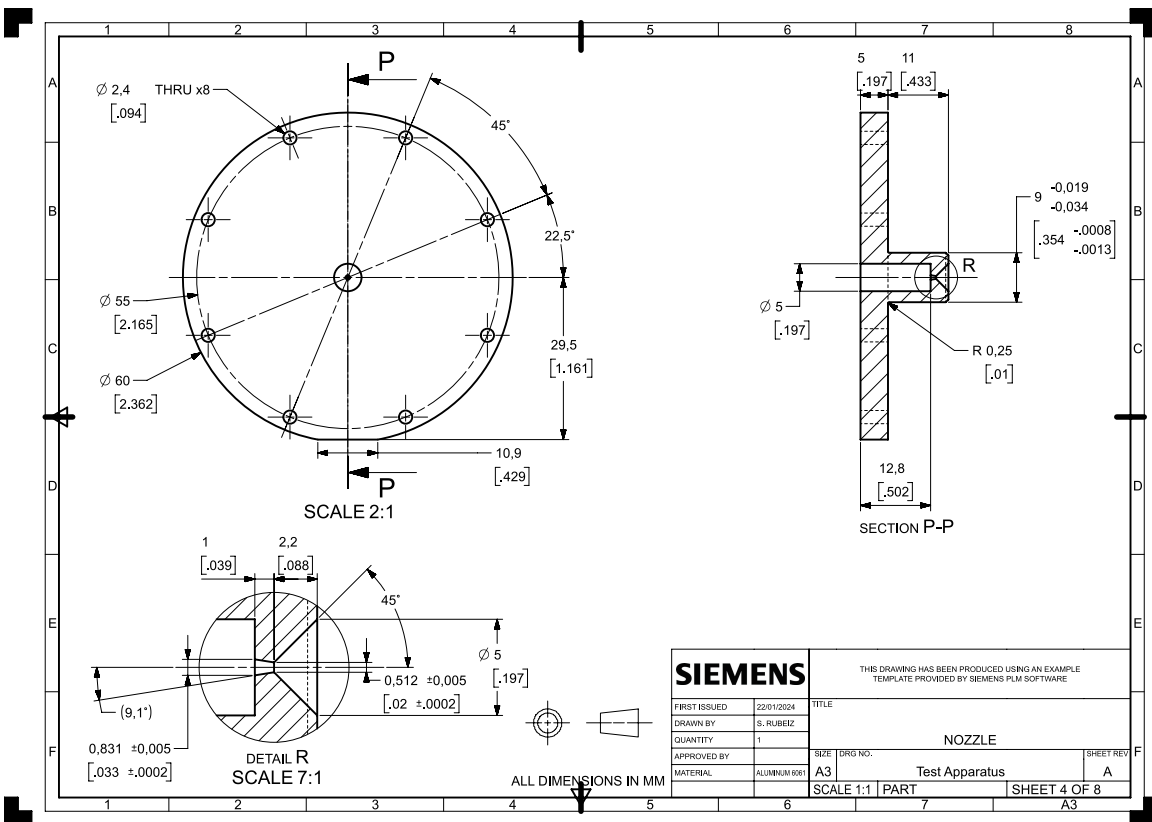
Appendix D

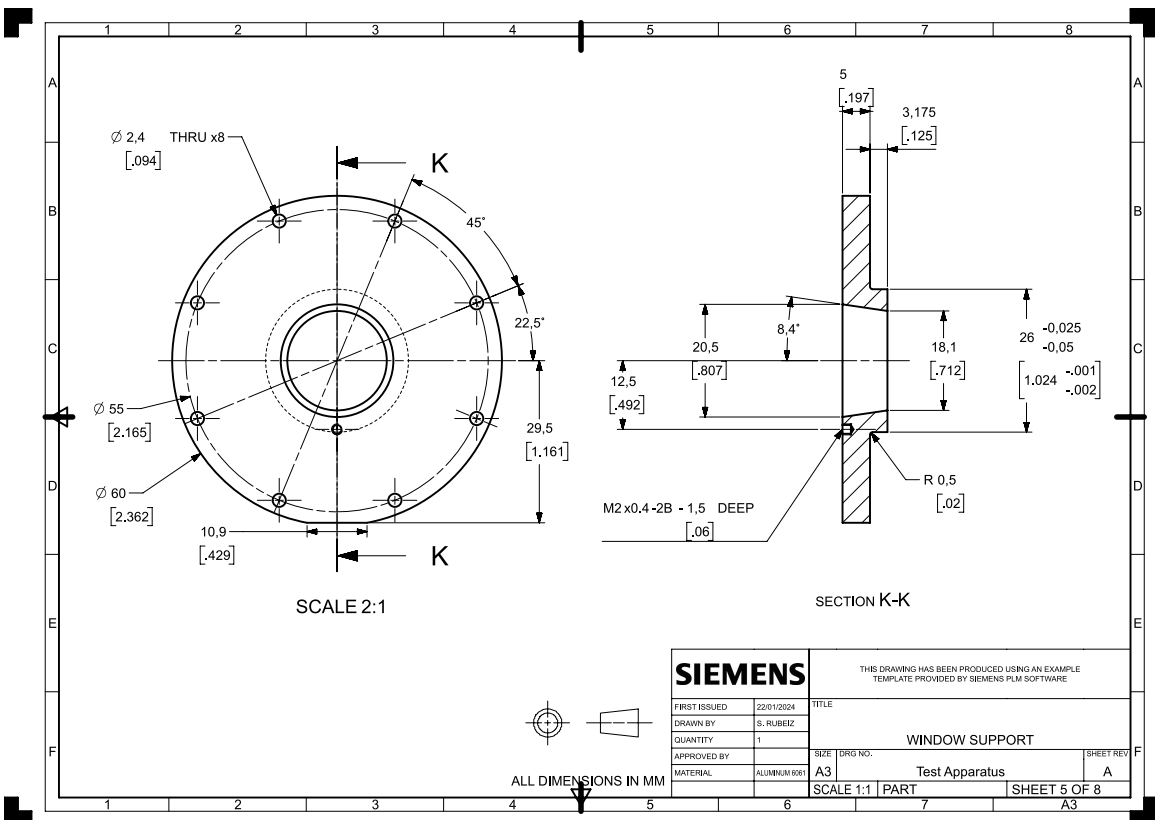
V2 Test Section Parts Drawings

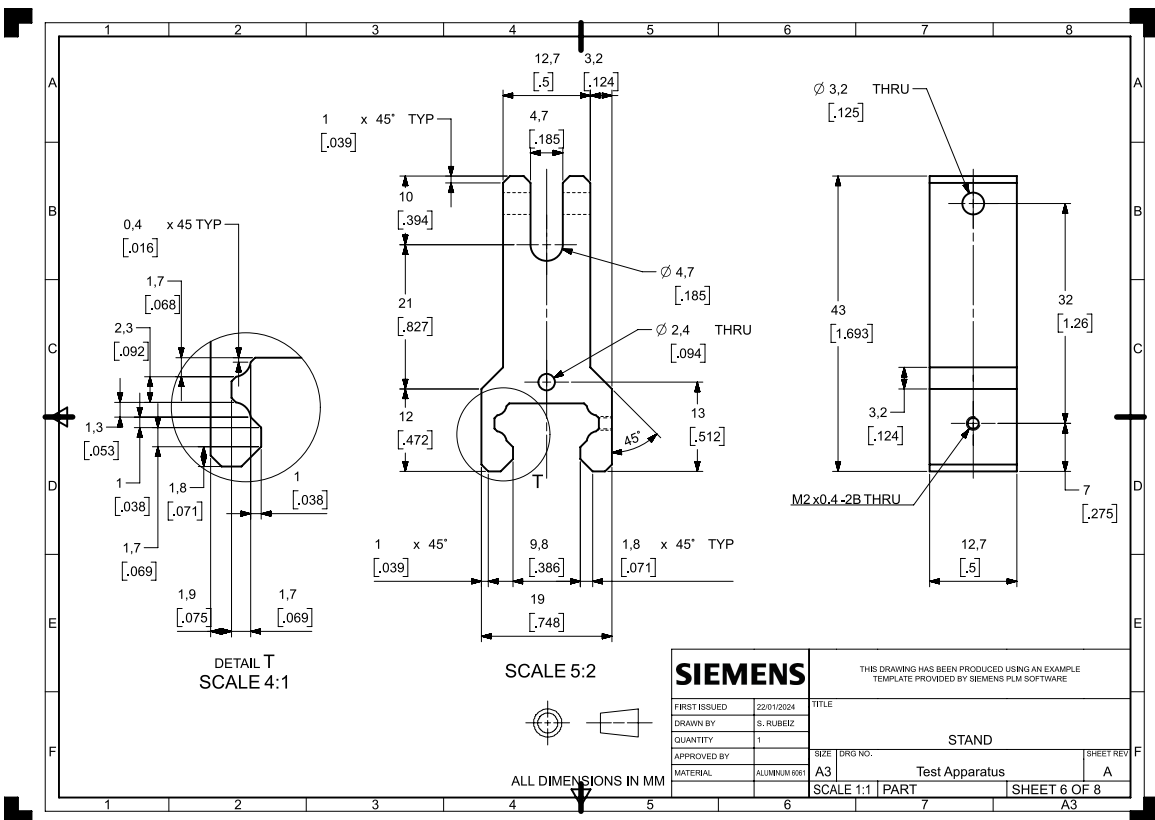


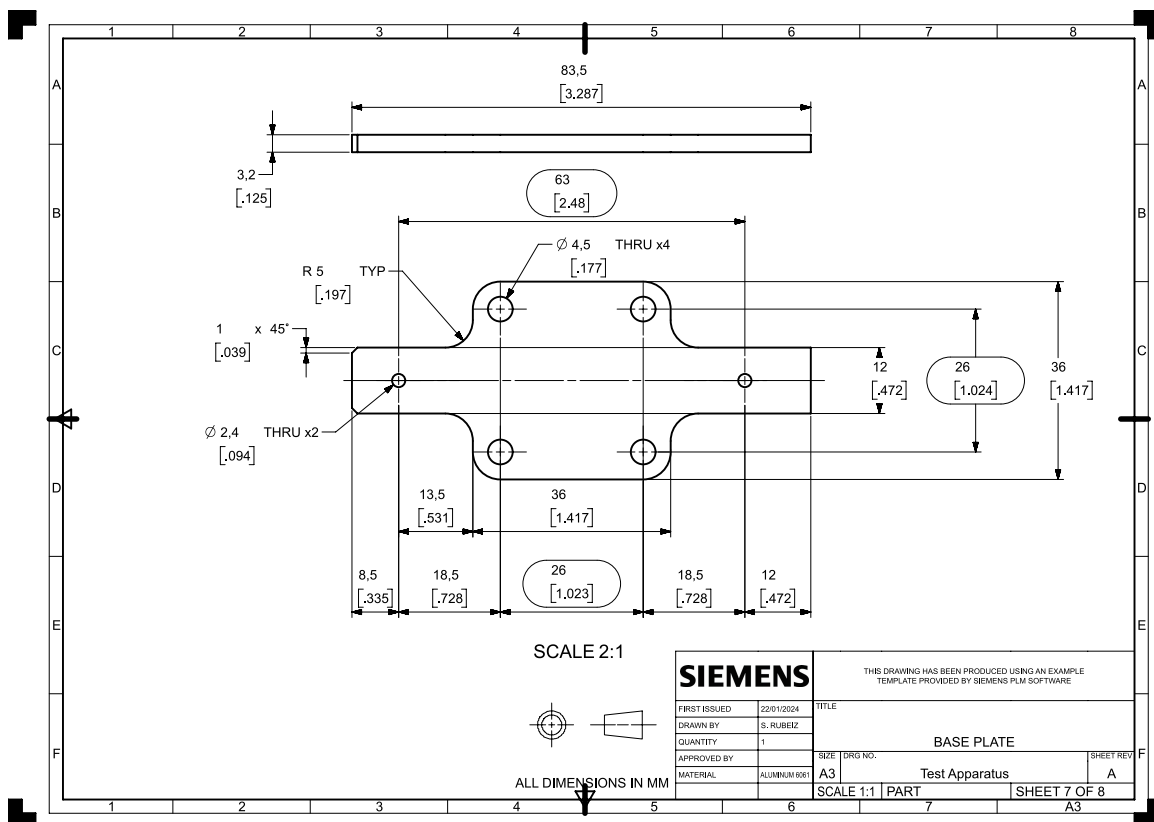


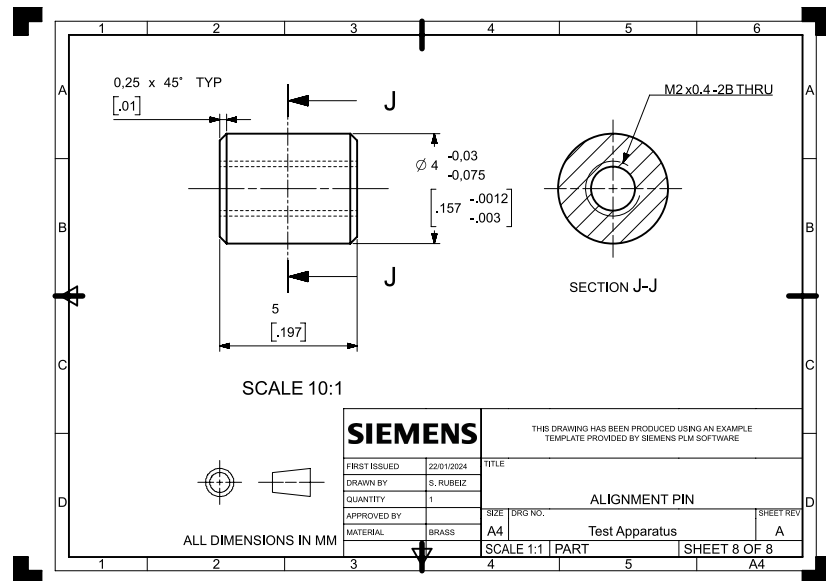






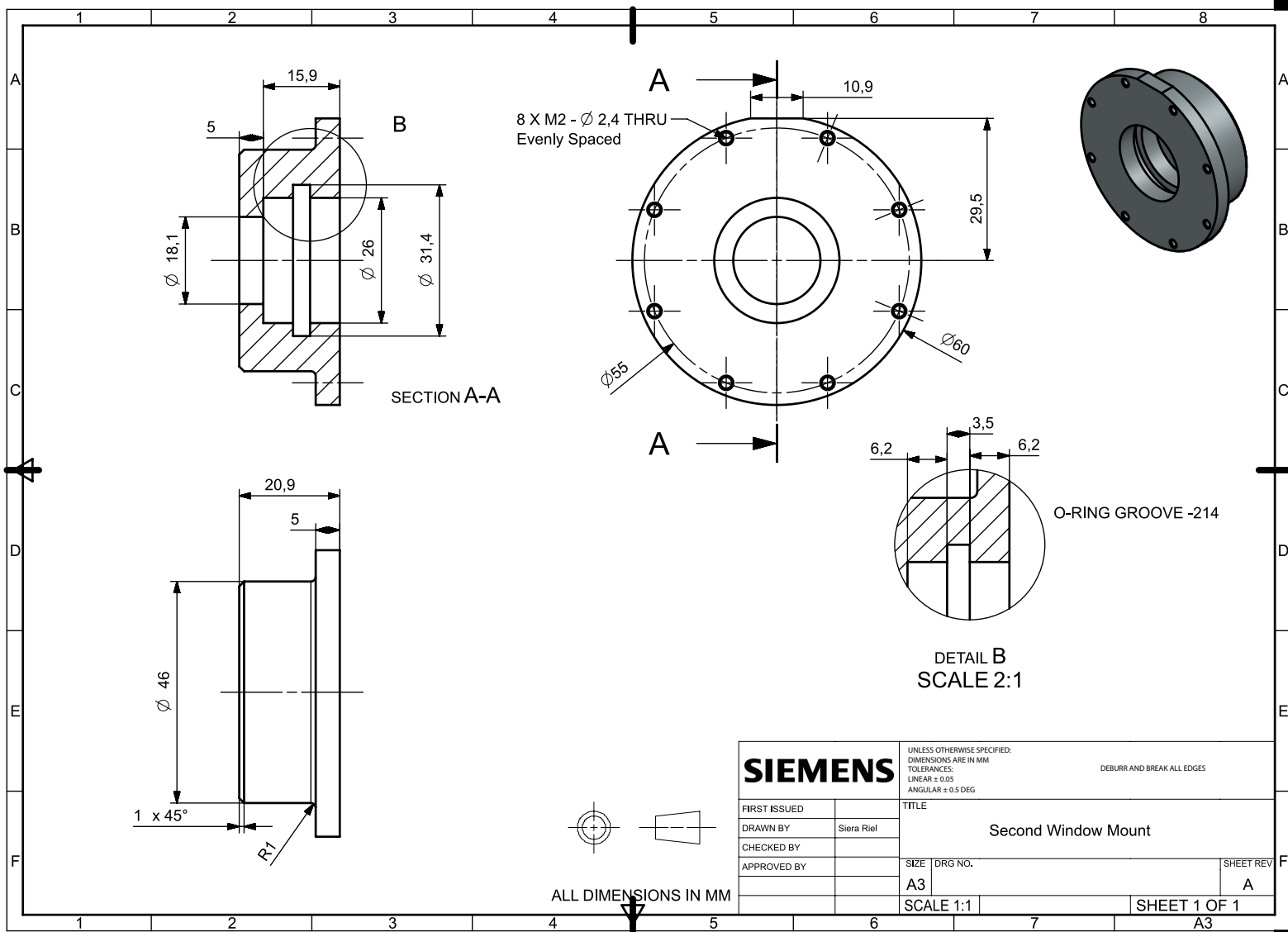






Appendix E

V2 Second (Rear) Window Mount



Appendix F

Untested V2 Parts Drawings

